REPORT DOCUMENTATION PAGE

Form Approved
OMB No. 0704-0188

1. AGENCY USE ONLY *(Leave blank)*	2. REPORT DATE	3. REPORT TYPE AND DATES COVERED
	~~7 Jan 99~~	DISSERTATION

4. TITLE AND SUBTITLE
SELF-GUIDING EFFECTS IN GALLIUM ARSENIDE SEMICONDUCTOR OPTICAL AMPLIFIERS

5. FUNDING NUMBERS

6. AUTHOR(S)
MAJ KUTSCHE CARL A

7. PERFORMING ORGANIZATION NAME(S) AND ADDRESS(ES)
UNIVERSITY OF CENTRAL FLORIDA

8. PERFORMING ORGANIZATION REPORT NUMBER

9. SPONSORING/MONITORING AGENCY NAME(S) AND ADDRESS(ES)
THE DEPARTMENT OF THE AIR FORCE
AFIT/CIA, BLDG 125
2950 P STREET
WPAFB OH 45433

10. SPONSORING/MONITORING AGENCY REPORT NUMBER
FY99-22

11. SUPPLEMENTARY NOTES

12a. DISTRIBUTION AVAILABILITY STATEMENT
Unlimited distribution
In Accordance With AFI 35-205/AFIT Sup 1

12b. DISTRIBUTION CODE

13. ABSTRACT *(Maximum 200 words)*

14. SUBJECT TERMS

15. NUMBER OF PAGES

16. PRICE CODE

17. SECURITY CLASSIFICATION OF REPORT	18. SECURITY CLASSIFICATION OF THIS PAGE	19. SECURITY CLASSIFICATION OF ABSTRACT	20. LIMITATION OF ABSTRACT

SELF-GUIDING EFFECTS IN GALLIUM ARSENIDE SEMICONDUCTOR OPTICAL AMPLIFIERS

By

CARL ALAN KUTSCHE
B.S. University of Michigan, 1980
M.S. Air Force Institute of Technology, 1991

A dissertation submitted in partial fulfillment of the requirements
for the degree of Doctor of Philosophy
in the Department of Electrical and Computer Engineering
in the College of Engineering
at the University of Central Florida
Orlando, Florida

Summer Term
1998

Major Professor: Patrick Li Kam Wa

Abstract

The realization of all-optical devices requires identification and characterization of materials possessing large nonlinearities and low loss. Although gallium arsenide – aluminum gallium arsenide (GaAs-AlGaAs) quantum well structures have very large third order resonant nonlinearities just below the bandgap, the absorption in this region makes them unusable for all-optical processing devices. Using these materials at below ½ of the bandgap reduces the losses, but also reduces the nonlinearity.

In this research, we investigate a different method of accessing the nonlinearity. By fashioning GaAs-AlGaAs double heterostructure devices into semiconductor optical amplifiers, a strong positive nonlinearity correlated to the gain of the device was identified and characterized. This nonlinearity is all the more valuable as these devices can provide gain to the signal as opposed to loss thereby boosting the effective nonlinearity of the devices. The detriment in using this type of carrier induced effect is that the nonlinearity is not instantaneous and requires over 1 ps to stabilize.

Standard interferometric techniques were used to characterize the nonlinearity in these forward biased devices. The resulting measurements when compared to Kerr nonlinearity of generic form $n_r = n_o + n_2 I$, returned an effective nonlinear coefficient of refractive index n_2 on the order of $5 \times 10^{-10} cm^2/W$.

Further characterization of these spatial solitons proved that they were capable of guiding a second, weaker non-coherent and cross-polarized signal beam within the refractive index trail created by the soliton writing beam.

Following that, a soliton beam-steerer was designed and fabricated from the same semiconductor double heterostructure material. The device employed a single mode waveguide to define the soliton launch path. The beam then passed through an electro-optic steering prism before landing within a 40-μm wide, active slab waveguide section. The solitons that were formed within this last section of the device were readily steered across a 20-μm wide region at the output facet of the slab using current injection into the steering prism. The mechanism for the beam steering was due to the carrier-induced nonlinearity and our measurements confirmed that the electrically induced nonlinearity was of the same magnitude as the optically induced nonlinearity (6.05×10^{-21} cm^3/carrier). This device may have potential applications as beam-routers in telecommunications networks.

Acknowledgments

This degree would never have succeeded without the Herculean ability of my wife to be both mother and father to my three children as well as wife and confidant to me for almost four years. Thank you. My thanks also to my children for their unwavering love and affection, even though I feared they may not recognize me from time to time.

To my advisor, Dr. Patrick Li Kam Wa who has ever amazed me with the breadth of his intellectual and practical knowledge. Technical guidance, intellectual management of our work, and advice on tough problems we expect from our advisors, but Dr Li Kam Wa provided an example in tenacious work and practical ingenuity that I will benefit from for the rest of my life. I have learned more from him than any other mentor I've had the privilege to work with.

In the same way, the members of my committee, Dr Stegeman, Dr Van Stryland, and Dr Delfyett have been instrumental in the formation and completion of this work. Particularly Dr Stegeman, who originally proposed the idea of self guiding in semiconductor optical amplifiers.

Working towards any goal can seem impossible without the proper work environment. As such, I'd like to thank Dr Soileau, director of CREOL, and the staff and faculty for creating an institution without barriers between student and professor. I've benefited from the association with many of the prominent researchers in their fields

through casual contact as well as grabbing someone in the halls and following them into their offices. Maintaining such an environment in an art.

Finally, I need to thank my two closest friends at CREOL, Brian Mathason and Steve Dunn. Many lunches and evenings have we studied together, bounced crazy ideas around, consoled each other, downed a few beers, and delivered a kick on the posterior when necessary. Thanks for keeping me sane, guys.

Table of Contents

List of Figures

CHAPTER 1: INTRODUCTION

Until the development of the laser by Maiman in 1960,[1] the field of optics was limited to linear systems. At this time, copper cables held a monopoly on long haul communications, and the cladded core fiber optic cable had just been introduced[2] mainly for the purpose of image transmission through a bundle of glass fibers.[3]

The laser provided the first stable source of intense, coherent light, and the advent of the laser launched a new revolution in optics. Soon after the laser's development, Franken demonstrated second harmonic generation for the first time using crystalline quartz.[4] Over the next two years optical rectification,[5] sum frequency generation,[6] optical parametric amplification,[7] stimulated Raman scattering[8] and third order intensity dependent refractive index changes[9] were all reported.

The first semiconductor laser was reported in 1962, however, it wasn't until the later years of the 1970's that improved material growth combined with sophisticated micro-fabrication techniques paved the way for the mass production of reliable cw GaAlAs laser diodes.[10] Techniques such as gain switching,[11,12] proton implanted quantum well passive mode locking,[13] active mode-locking,[14] and hybrid mode locking[15] have been utilized to shorten output pulses and raise peak powers of semiconductor diode lasers.

Pulses as short as 200fs with over 160W of peak power have been demonstrated using external cavity, semiconductor laser systems with intra-cavity elements.[16]

At the same time, improved purity and fabrication processes reduced transmission losses in optical fibers from an initially high value of >1000 dB/km to 20dB/km by 1970,[17] and to 0.2 dB/km by 1979.[18] Nonlinearities in fibers such as stimulated Raman and Brillouin scattering,[19] optically induced birefringence,[20] four-wave mixing,[21] self-phase modulation and temporal solitons[22] were demonstrated in fibers throughout the 1970's. These techniques have been used for a variety of systems such as the erbium-doped fiber amplifier developed in 1990 and made commercially available in 1992,[23] and in fiber pulse compression techniques allowing the production of a 6 fs pulse.[24] Most recently, low loss plastic fibers are under development for use in short haul, high traffic applications. These links permit the use of 650 nm laser diodes and have been demonstrated to operate in excess of 2.5GBps.[25]

1.1 DEVICES FOR INFORMATION TECHNOLOGY

It should be no surprise that research pushes the envelope of optical processing speed. With the explosion of data traffic passing through land, ocean, and satellite links, a real need exists for systems that pass as much data through every communications link as fast as possible. Fiber optic lines with a theoretical effective bandwidth of 25THz[26] can replace thousands of coaxial links, 100MHz bandwidth, and even more twisted pair lines, 1MHz bandwidth.[10] Unfortunately, the ability of electrical components to load 25THz of

information onto a fiber optic link has not caught up with the link's capability, and most likely never will. Optical systems, on the other hand, have the potential of routing information onto, through, and off of these high-speed links. Recently, researchers at the NEC Corporation demonstrated a 2.6 Terabit/sec (20-Gbit/sec x 132 channels) communication link.[27] Devices such as an all-optical clock recovery system[28] and a 20-channel optical transmitter fabricated from a single laser diode assist in loading and unloading information from these links.[29] High speed demultiplexers such as the Terahertz Optical Asymmetric Demultiplexer (TOAD),[30] nonlinear optical loop mirror (NOLM),[31] and soliton switch[32] can optically route data up to several hundred gigabits per second. A prototype Y-junction device has also been demonstrated to provide a switching response capable of demultiplexing data at a rate of 588 GHz.[33] Many other switching devices using the nonlinear effects listed above have been fabricated and demonstrated.[34]

1.2 MATERIAL NONLINEARITIES

The performance of optical switches depends strongly on the materials they are fabricated from. Several figures of merit (FOM) exist as ratings of a material's suitability for use as a nonlinear optical device. For example, the FOM for a linear loss system is[35]

$$W = \frac{n_2 I(0)}{\alpha_0 \lambda} > 1 \qquad (1.1)$$

where the FOM, W, is to be maximized, n_2 is the nonlinear coefficient, $I(0)$ is the launch intensity, α_0 is the absorption, and λ is the wavelength. As all nonlinear optical devices require at least a 2π nonlinear phase shift,[35] this FOM must exceed 1.0. The form of the FOM varies based upon the mechanism responsible for the nonlinearity, however, all maximized nonlinear FOM's have two things in common: a high nonlinear coefficient and low absorption.

Vast improvements have been made in creating materials with large nonlinearities and low loss, as well as harnessing the nonlinearities to their fullest extent possible. Franken used crystalline quartz ($d_{11} = 4*10^{-13}\ m/V$)[36] for his second-harmonic generation experiment. Today, lithium niobate ($LiNbO_3$), barium titanate ($BaTiO_3$), and lithium iodate ($LiIO_3$) possess second order nonlinear coefficients one to two orders of magnitude larger than quartz. The nonlinear coefficient of $CdGeAs_2$ is three orders of magnitude larger than that of quartz. Nonlinear materials have also been developed with outstanding third order nonlinearities. The high-speed conjugated polymer PTS has a third order nonlinearity of $2.2x10^{-12}\ cm^2/W$ and an unusually high fifth-order nonlinearity of $-0.8x10^{-15}\ cm^4/W^2$. This combination permitted researchers to demonstrate stable 2-dimensional first and second order solitary waves, typically very unstable, within this material[37]. In comparison, silica glass fibers have a third order nonlinearity of only $2x10^{-16}\ cm^2/W$. The extremely low losses in these fibers, however,

allows very efficient length scaling and help maintain SiO_2 fibers as a viable nonlinear material[35] for all-optical devices.

Device geometries also play an important role in developing nonlinear devices and techniques. Second harmonic fields, for instance, will back convert to the primary wavelength then back to the second harmonic in a periodic manner. Quasi-Phase matching eliminates this back conversion by stopping or reversing the down conversion during that part of the propagation.[38] Cascading nonlinearities provides another avenue to advance the state of the art. Cascading makes use of the second harmonic down conversion to create an effective third order nonlinearity. This process takes advantage of the large second order coefficient to generate large third order nonlinearities.[39] Using this approach, researchers have created spatial solitons in KTP crystals.[40,41] This method provides stable beam self-focusing and second harmonic generation together in one automatically aligned path. Using this technique, the index tuning range, usually small for typical second harmonic crystals, was enhanced by a factor of ten.[42]

1.3 NONLINEARITY IN SEMICONDUCTOR OPTICAL AMPLIFIERS

One of the drawbacks of third order nonlinear coefficients is that they are typically small, usually $1x10^{-16}$ to $1x10^{-13} cm^2 / W$. Creating an index change large enough to form spatial solitons in these materials requires intense optical intensities, typically generated by mode-locked or Q-switched short pulse lasers. Materials with larger nonlinearities have been found, however, they typically have large absorption.[35] This

absorption degrades device performance making the nonlinearity an interesting, but useless, phenomenon.

Semiconductors also possess large nonlinearities near their bandgap.[43,44] Third order coefficients as large as $-2x10^{-4}\ cm^2/W$ for exciton saturation have been reported.[45] Like many other materials, semiconductors also possess a large absorption near the bandgap, when they are inactive. One potential is to use a passive AlGaAs waveguide at below ½ of the bandgap to access the Kerr like nonlinearity while avoiding two-photon absorption. At this wavelength, the positive third order nonlinearity was measured to be $1.5x10^{-13}\ cm^2/W$ and $1.43x10^{-13}\ cm^2/W$ for the TE and TM polarization states relative to the slab waveguide.[46] As the ratio of cross-phase modulation to self-phase modulation is almost one, several varieties of spatial solitons such as primary, vector and Manakov have been observed.[47] Unfortunately, the small magnitude of this nonlinearity requires large optical powers to access enough self-phase modulation to observe self-focusing.

There exists, however, a strong resonant nonlinearity at the band edge. The nonlinearity lies well within the absorption edge of the material, but by fashioning the material into a semiconductor optical amplifier the nonlinearity can be used in the gain region of the material.[48]

There are many mechanisms involved in this gain nonlinear process. Figure 1.1 shows the time evolution probe response of the nonlinearity to a 440 femto-second pump pulse for GaAs-AlGaAs amplifier in the gain (a), transparency (b), and absorption (c) regions. In each of these regions, a strong instantaneous negative nonlinearity, lasting on

the order of 150 fs, was attributed to rapid electronic or virtual processes.[49] A positive going nonlinear spike caused by free carrier heating[50,51] and by spectral hole burning within the homogeneously broadened amplifier[52,53] quickly replaced this nonlinearity. The long-term behavior of the probe phase shift depends upon the slowly recovering carrier density change caused by the pump beam.[50] Both the Burstein-Moss shift and Free Carrier Plasma models describe this shift. The sign of this long-term nonlinearity depends on whether the device is in the absorption, transparency, or gain region.

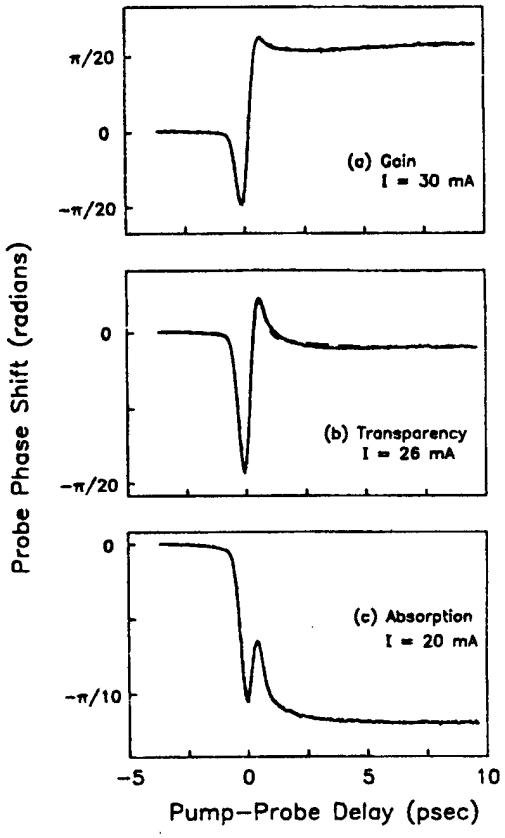

Figure 1.1 Time Resolved Probe Phase Change in AlGaAs Optical Amplifiers for the (a) gain, (b) transparency, and (c) absorption regimes. Pump duration was 440 fs[50].

These measurements indicate that the short pulse bright soliton is doomed to fail, as the nonlinearity is always negative for short pulses. Delfyett, however, performed the same measurements using longer pulses and found that the negative going initial spike was not detectable for pulses of one picosecond in duration.[16] A long, one-microsecond pulse therefore, was selected to create the spatial solitons characterized in this dissertation. The two mechanisms leading to a positive nonlinearity are the Burstein-Moss Shift, and the index shift caused by the change in the free carrier plasma. Both provide a positive nonlinearity in the spectral gain region.

1.3.1 DYNAMIC BURSTEIN-MOSS SHIFT

Absorption and gain in a semiconductor is the process of either raising an electron from the valence band to the conduction band or vice versa through interaction with a photon. In optical absorption, the energy in a photon is transferred to an electron in the valence band thus raising the energy level of the electron. As there are no levels to be occupied between the bands, photons with energies below the bandgap are not absorbed and pass through the material. Photons with energies exceeding the bandgap are readily absorbed. Upon entering the conduction band, the electron will rapidly thermalize in times much less than the carrier lifetime to fill states near the band extrema. As only one carrier can occupy a state at any time, the next absorption event must raise an electron from a slightly lower level in the valence band to a slightly higher level in the conduction band. Although the effect is negligible for a single carrier, a significant amount of

absorption will cause the band edge to shift towards the higher energy side (blue shift). This is the Burstein-Moss shift.[54,55] The reverse shift is also true in the emission region. When a distribution of excited carriers in the conduction band is significantly depleted by stimulated gain, the band edge shifts towards lower energies or a red shift.

A periodic crystal lattice, such as a semiconductor, has distinct properties that effect the number, distribution, and energy of the electrons and lack of electrons (holes) in the ground state (valence band) of the material. Characteristic of semiconductors is the band diagram. The diagram depicts a series of closely spaced states at and below the valence band for holes, and at and above the conduction band for electrons. Separating these bands is the forbidden bandgap where there are no states. The number of carriers, n for electrons in the conduction band and p for holes in the valence band, is characterized by the expression[56]

$$\begin{aligned} n_0 &= \int_{\varepsilon_c}^{\infty} N(\xi) f(\xi) d\varepsilon \\ p_0 &= \int_{-\infty}^{\varepsilon_v} N(\xi)[1 - f(\xi)] d\varepsilon \end{aligned} \tag{1.2}$$

$N(\xi)$ is the density of states function that defines the number of states available for potential occupation, and $f(\xi)$ is the Fermi function which defines the probability that a given state will be occupied. Under normal equilibrium conditions, the Fermi function is dependent on the Fermi energy ξ_f and temperature T and is identical for both n and p concentrations.

$$f(\xi) = \frac{1}{1 + exp\left(\frac{\xi - \xi_f}{k_B T}\right)} \tag{1.3}$$

Under electrical pumping conditions, however, the concentrations of electrons and holes in their respective bands can exceed these equilibrium levels. In these cases, the probability of occupation is split into two functions that use quasi-Fermi levels, ξ_{fn} and ξ_{fp} to describe the probability of occupation in each of the levels.

$$\begin{aligned} f_n(\xi) &= \frac{1}{1 + exp\left(\frac{\xi - \xi_{fn}}{k_B T}\right)} \\ 1 - f_p(\xi) &= \frac{1}{1 + exp\left(\frac{\xi - \xi_{fp}}{k_B T}\right)} \end{aligned} \tag{1.4}$$

Knowledge of the number of carriers in excess of the equilibrium level, Δn and Δp, existing in an area is necessary to determine the quasi-Fermi level.

$$\begin{aligned} \xi_{fn} &= \xi_c + k_B T \, ln\left(\frac{n_0 + \Delta n}{N_c}\right) \\ \xi_{fp} &= \xi_v - k_B T \, ln\left(\frac{p_0 + \Delta p}{N_v}\right) \end{aligned} \tag{1.5}$$

N_c and N_v are the effective density of states constants for the semiconductor. For GaAs $N_c = 4.4x10^{17} cm^{-3}$ and $N_v = 8.2x10^{18} cm^{-3}$. The rate at which absorption or gain can occur is dependent upon the probability that states exist and are filled that satisfy conservation of momentum. These rates are defined by the expressions

$$r_{abs}(\xi) = P_{abs} N_J(\xi)[1 - f_n(\xi_2)] f_p(\xi_1) N_p(\xi)$$
$$r_{st}(\xi) = P_{st} N_J(\xi) f_n(\xi_2)[1 - f_p(\xi_1)] N_p(\xi) \tag{1.6}$$

In these expressions, P is the transition probability and N_p is the density of photons of energy ξ, and N_J is the joint density of states function. Weighted energies ξ_1 and ξ_2 are selected to maintain conservation of energy, $\xi_2 - \xi_1 = \hbar\omega$, and conservation of momentum, $k_{electron} = k_{hole} + k_{photon}$. The photon momentum is negligible compared to the mass of the electron and hole, and we approximate this conservation as $k_{electron} \approx k_{hole}$. Assuming the energy bands are parabolic with characteristic masses m_e^* and m_h^*.

$$\xi_2 = \xi_c + \frac{m_r^*}{m_e^*}(\xi - \xi_g)$$
$$\xi_1 = \xi_v - \frac{m_r^*}{m_e^*}(\xi - \xi_g) \tag{1.7}$$

m_r^* is the system reduced effective mass given by $\frac{1}{m_r^*} = \frac{1}{m_e^*} + \frac{1}{m_h^*}$.

The net stimulated emission rate per energy is the difference between the absorption rate and the emission rate. Dividing this difference by the net number of photons crossing a given area of speed $\frac{c}{n_r}$ and assuming P_{em} and P_{st} are identical, the spectral form of the gain $g(\xi)$ becomes

$$g(\xi) = \frac{\sqrt{2}(m_r^*)^{3/2} q^2 p^2{}_{CV}}{3\pi n_r \in_0 m_0^2 \hbar^2 c\xi} \sqrt{\xi - \xi_g}\left[f_n(\xi_2) - f_p(\xi_1)\right] \tag{1.8}$$

In an active semiconductor, the carrier distribution is created through electrical injection of carriers into the gain region. Knowing the number of carriers injected into the active gain region, and the average lifetime the carriers exist prior to recombination, we can calculate the quasi Fermi levels and finally the gain spectrum. If stimulated emission occurs, the average carrier density will decrease locally causing a change in the gain spectrum.

This change can be directly related to the change in the index of refraction through the Kramers-Kronig relationship, appendix B. Figure 1.2 shows the effect that a change in the gain spectrum has on the refractive index of the material, assuming an incident optical excitation at the peak of the gain curve. It is important to note that the change in index is not the same for all wavelengths, but that the change in refractive index is positive for all energies below the peak of the gain. Furthermore, the change in the index of refraction calculated by this method is a change in index per depleted carrier ($\Delta n/\Delta N$). Thus, the actual change in the index of refraction is proportional to the change in carrier population within the amplifier.

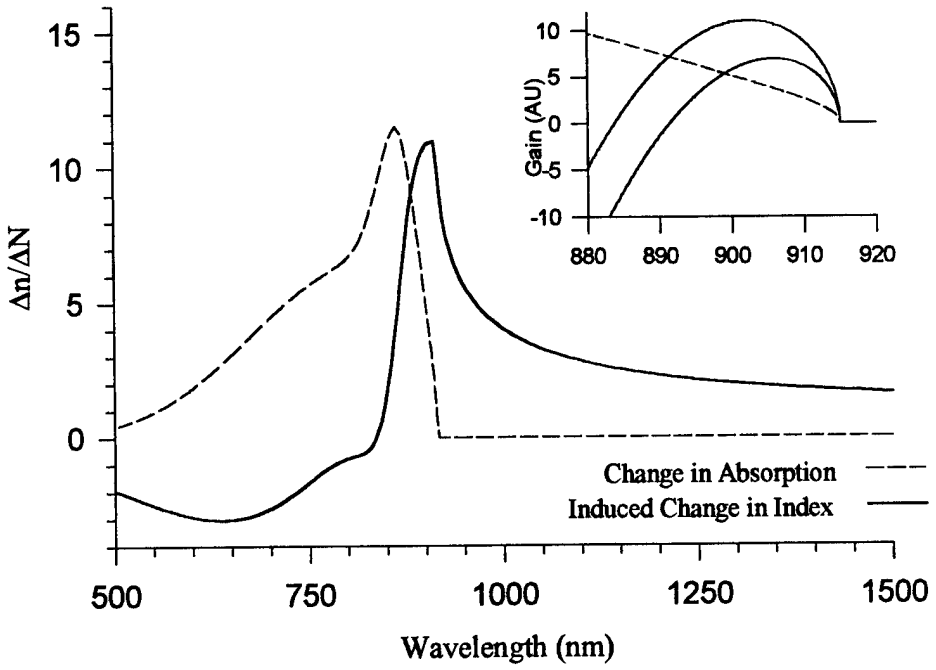

Figure 1.2 Index Change Due to Absorption Change, Kramers-Kronig Relationship. Inset shows gain change and delta gain in the region about the peak of the gain.

1.3.2 FREE CARRIER PLASMA

The effect of free carriers on a semiconductor's susceptibility results from the characteristic absorption of free carriers in the infrared. The peak of the absorption increases in energy with carrier density, thus increasing the carrier density will decrease the susceptibility, and the index of refraction, below the peak of the absorption. The susceptibility's dependence on carrier concentration is given as[57,58]

$$\chi = -\frac{Ne^2}{\epsilon_0 \omega^2 m_e^*} \tag{1.9}$$

where N is the carrier concentration, e is the electron charge, $\in_0$ is the free space permittivity, ω is the angular frequency of the radiation, and m_e^* is the effective carrier mass. The effective mass of the electrons is much smaller than that of the holes, thus only the change in the susceptibility caused by the electrons need be taken into account. The susceptibility is related to the index of refraction by the approximate equation, see appendix A,

$$n^2 = 1 + \chi \tag{1.10}$$

Using a change in the carrier concentration to produce a change in the index of refraction yields the perturbation equations

$$\begin{aligned} \Delta n &= \frac{1}{2n_0}\frac{d\chi}{dN}\Delta N \\ \Delta n &= -\frac{\Delta N e^2 \lambda_0^2}{8\pi^2 \in_0 n_0 m_e^* c^2} \end{aligned} \tag{1.11}$$

ΔN in an optical excitation case would be the change in carriers caused by the optical beam.

1.3.3 CARRIER CONCENTRATION CHANGE IN A GAIN DEVICE

The changes in the index of refraction derived above depend upon a change in the carrier concentration. This change, however, is not constant in an amplifier and must be taken into account. To account for this change, we examine the change in carrier concentration in a differential increment along the optic axis. The power along the axis is

given by $P(z) = P_{in}\, exp(gz)$ where g is the gain coefficient, z is the distance along the optic axis with z=0 at the input, and P_{in} is the optical power at the input. The change in the carrier concentration in an incremental segment is proportional to the increase in optical power found by differentiating the power equation.

$$\frac{dP}{dz} = gP \tag{1.12}$$

The change in carrier concentration is measured within the volume Adz, where A is the effective cross sectional area of the beam. Power relates to individual electronic transitions by the optical quanta $\hbar\omega$, thus the rate of carrier depletion per unit volume is

$$\frac{dN}{dt} = \frac{gP}{A\hbar\omega} \tag{1.13}$$

Noting that the power per unit area is intensity, and the change in carrier density relaxes with a time constant τ, the change in the carrier concentration becomes

$$\Delta N = \frac{gI\tau}{\hbar\omega} \tag{1.14}$$

In the semiconductor slab waveguides used in this research, the cladding material's bandgap exceeds the energy of the gain region, and is transparent. Thus any of the gain, or absorption will be restricted to the region of the gain. Thus, a smaller effective gain needs to be used as opposed to the calculated gain. This effective gain is the calculated gain times the confinement factor, Γ, which is the ratio of the amount of guided energy in the active region over the total amount of guided energy. Applying equation to the basic forms of the change in the index of refraction, equations and yields the standard form

$\Delta n = BgI$, where B is the effective change in the index of refraction in the zero-gain transparency region. Using the standard Kerr model of the nonlinearity $n = n_0 + n_2 I$, the nonlinear coefficient, n_2, is effectively amplified by the gain provided by the device. As the gain of a semiconductor amplifier can reach values of 10,000 m^{-1}, the possibility exists to access nonlinearities four orders of magnitude larger than those typically seen in passive media.

Although this method indicates an instantaneous n_2, an alternate method to examine the gain uses the total phase shift to calculate the nonlinear coefficient. This total phase shift is found by the integration of the incremental phase shifts along the path of propagation. This becomes

$$\begin{aligned} \Delta\phi &= \int_0^z k n_2 I_{in} e^{gz} dz \\ &= k n_2 I_{in} \frac{e^{gz} - 1}{g} \end{aligned} \tag{1.15}$$

This equation has the same form as the non-gain equation if the top and bottom of the right hand side are multiplied by the distance z and a new nonlinear coefficient of

$$n_2' = \frac{e^{gz} - 1}{gz} n_2 \tag{1.16}$$

is used. For values of the gz multiple less than 2, this function exhibits linear behavior with a slope of approximately ½. Thus with the length of the device fixed, the gain effects the nonlinearity by approximately $n_2(1+½\, gz)$.

1.3.4 GAIN SATURATION

When the optical beam traversing the amplifier becomes so large that the rate of removal of excited carriers exceeds the electrical pumping rate, the gain will saturate. The gain spectrum arising from the radiative recombination of excited electrons of the semiconductor optical amplifier is homogeneously broadened. Thus, gain saturation in these devices I_s, is given by the following,[59]

$$g = \frac{g_0}{1 + \frac{I}{I_s}} \tag{1.17}$$

Here g_0 is the small signal gain. As the third order optical nonlinearity depends on the magnitude of the gain, the nonlinearity itself eventually saturates with a characteristic saturation intensity I_s.

1.3.5 EXCITON EFFECTS

Exciton saturation creates large nonlinearities as well.[45] Excitons are a lower energy state created when electrons and holes on either side of the bandgap are in close spatial proximity and retain a coulombic attraction to each other. Excitons are not typically measured at room temperature in bulk devices; however, high quality, quantum well structures provide enough spatial confinement to form excitons. The exciton can be seen as one or two absorption peaks just below the main absorption band edge.

Promoting carriers into the conduction band easily saturates excitons. The saturation alters the absorption spectrum, and creates an intensity-based change in the refractive index through the Kramers-Kronig relationship. As quantum structures were not available at the time of this research, exciton saturation was not investigated.

1.4 SOLITON

To describe a spatial soliton, we start with the polarization of the material the soliton exists in. The expression for the polarization of a linear material is $P = \epsilon_0 \chi E$ where χ is the linear response of the material to a field E. In nonlinear materials, however, the polarization varies in time, depends on frequency, and contains multiple cross terms linking the polarizability between frequency components. To allow mathematical manipulation of the polarization term, it is common to assume that the polarization is instantaneous and to approximate the polarization response by a Taylor expansion of the polarization.

$$P(\omega) = \epsilon_0 \begin{pmatrix} \chi^{(1)}(\omega)E + \chi^{(2)}(\omega;\omega_1,\omega_2)E(\omega_1)E(\omega_2) + \\ \chi^{(3)}(\omega;\omega_1,\omega_2,\omega_3)E(\omega_1)E(\omega_2)E(\omega_3) + \ldots \end{pmatrix} \tag{1.18}$$

In this notation, $\chi^{(2)}(\omega;\omega_1,\omega_2)$ is the second order susceptibility at frequency ω arising from stimulation at frequencies ω_1 and ω_2. Of particular interest are situations where there is only one input stimulus, and we are interested only in the response of the material at that frequency. This situation is called the self-action nonlinearity and equation above reduces to

$$P(\omega)=\epsilon_0\left(\chi^{(1)}E+\chi^{(2)}E^2+\chi^{(3)}E^3+...\right) \tag{1.19}$$

this term can be inserted into the nonlinear Schroedinger Wave equation (NSWE), described in appendix A, to derive the closed form solution for a bright spatial soliton, assuming the $\chi^{(2)}$ term is negligible.

$$I(x)=A_0\,sech^2\left(\frac{x}{a_0}\right) \tag{1.20}$$

Here A_0 measures the amplitude of the soliton, and a_0 is the waist of the soliton in the dimension where diffraction is allowed. As stated above, the soliton is usually stable in only one dimension, the confinement in the other dimension must be provided by a slab waveguide. In this dimension, where diffraction is not allowed, w is used to describe the beam size. Inserting equation (1.2) into the NSWE, the relationship

$$P_s a_0=\frac{2w}{n_0 n_2 k_0^2} \tag{1.21}$$

is derived, where P_s is the linear power contained in the soliton and n_0 and n_2 are the linear and nonlinear indices of refraction. These form the expression for the index of refraction in a Kerr nonlinear material.

$$n(x)=n_0+n_2 I(x) \tag{1.22}$$

Noting that all of the terms to the right of the equality are constants, the ratio between soliton power and waist remains constant. Therefore, in low loss systems, the waist remains constant.

The soliton can be described logically in this manner. Propagating light diffracts. Because the index of refraction in a Kerr like material varies with the intensity of light at a given position, the index of refraction of a propagating beam will be highest at the center of the beam and the least at the edges. This forms a positive lens causing the beam to focus. For any beam, the tighter the focus generally means the larger the diffraction. For the nonlinearity, the larger the optical intensity at the peak, the tighter the focusing will be. Eventually, a stable condition can be reached in one dimension and the beam's natural diffraction is exactly balanced by the nonlinear self-focusing.

1.4.1 MATHEMATICAL VS OTHER SOLITONS

The spatial soliton described in the previous section is a closed form solution to the NSWE in a perfect Kerr nonlinear material. This type of soliton has many specific mathematical properties such as when N solitons collide, N solitons will emerge which travel in the same direction as the input solitons, but endure a lateral shift. Additionally, mathematical solitons are reciprocal meaning that a series of beams launched backwards along the path used to create a forward pattern, will recreate the launched pattern at the input. Many other soliton like beams can be created that possess the self-guided nature of a perfect mathematical soliton but may not necessarily possess all of the characteristics of a mathematical soliton. Throughout the remainder of this dissertation, the term soliton will be used to label a self-focused beam; however the beam may not conform to the strict properties of the mathematical soliton.

1.4.2 DEMONSTRATED SOLITONS

Kerr nonlinearity below the two-photon absorption bandgap was used to create fundamental bright solitons, Vector solitons, and Manakov solitons in AlGaAs slab waveguides. This was remarkable as very few materials have the self and cross phase modulation terms nearly equal as AlGaAs does.[60]

In second order nonlinear materials, the second order nonlinearity can cascade to produce the fundamental wavelength and, if the nonlinearity is strong enough, can result in soliton like self-guiding. As discussed above, this has been demonstrated in KTP.[61]

Khitrova and Gibbs demonstrated spatial solitons in InP, using the same mechanism used in this research to produce spatial solitons in GaAs.[62]

Two-dimensional solitons have been created in materials with a strong negative fifth order nonlinearity. This nonlinearity prevents the beam from focusing too tightly thereby avoiding damage to the optical medium.[63]

Dark solitons can be generated in materials with negative third order nonlinearities, and photorefractive materials can also self-guide optical beams. All of these alternate methods of creating soliton like self-guided beams, with the exception of the pure Kerr material, have some, but not all, of the properties of the mathematical soliton. As such, the term soliton will be used throughout the remainder of this dissertation with the understanding that the solitons measured in this work are not pure mathematical solitons.

1.4.3 SOLITON BEAM STEERING AND TRAPPING

The profile of the index of refraction creates a waveguide as long as the soliton exists. This waveguide can be used to guide, steer, and trap other beams. The form of the index profile of the soliton waveguide for Kerr like materials will be $sech^2$ in shape. The index shift is not typically large, however, the graded index nature of the waveguide permits better guiding without a large shift in the index of refraction. Kang used solitons to trap beams in AlGaAs waveguides, and Lawrence used 2 dimensional solitons to steer beams through a nonlinear crystal. A prime concern in passing a soliton through a steering prism is the soliton's ability to remain intact. Kang studied this problem and concluded that solitons remained stable even when ½ of the soliton passed through the prism area while the other half did not.[64]

1.5 STUDY TO FORM SOLITONS IN SOA AND TRAPPING/GUIDING OF SECOND BEAM

As shown in the previous sections, a positive third order optical nonlinearity of significant magnitude exists in the spectral region of the semiconductor gain for long pulses. This dissertation undertook the task of creating the conditions necessary to demonstrate spatial solitary waves using this nonlinearity, characterizing the nature of the nonlinearity and the resulting spatial solitons, and finally using these solitons to guide a signal beam. These experiments form the basis for continued work on a proposed single

stage optic switch using electro-optic steering prism to steer the information, and soliton waveguides to contain the information.

The work carried out in this dissertation was performed on an undoped bulk GaAs gain region sandwiched between n and p type AlGaAs clad regions. Although quantum well devices could potentially provide larger third order nonlinearities, the wafer foundry was not able to undertake the task of optimizing an optical quantum well structure.

1.6 OUTLINE OF THIS DOCUMENT

This dissertation comprises 6 chapters. Chapter 1 outlines the basic theory behind the generation of third order nonlinearities in semiconductor optical amplifiers. Chapter 2 discusses the fabrication details involved in fabricating the devices used throughout this research. Chapter 3 describes the experiments preformed to characterize the semiconductor material and confirm the positions and magnitudes of nonlinearities. Chapter 4 reports on the successes achieved in creating and characterizing a spatial soliton created by end fire coupling an input beam into the cleaved end of a wide-stripe, active, semiconductor waveguide. Chapter 5 builds upon the soliton measurements by guiding a second signal beam along with the soliton beam. Finally, chapter 6 reviews the important findings discovered throughout this research and lays out recommended additional experiments advancing this research towards the ultimate goal of creating a usable soliton matrix switch.

CHAPTER 2: DEVICE STRUCTURE AND FABRICATION

Although the optical and electrical characterization of the materials and devices is a prime concern, the ability to reproducibly fabricate these devices was an integral portion of this work. Particularly so as a new clean room facility, along with totally new equipment, required installation, checkout, calibration, and application. As such, this chapter will outline the calculations and procedures used to design the optoelectronic devices used throughout this work. In addition, critical process steps used to fabricate these devices will also be explained.

2.1 DEVICE STRUCTURE

2.1.1 ACTIVE SEMICONDUCTOR OPTICAL GAIN

As shown in the introduction, for photon energies near the bandgap, the self-focusing nonlinearity in a semiconductor optical amplifier exists only in the spectral range where the semiconductor possesses gain. Although the gain can be optically induced, this

research employed electrically injected carriers to create the population inversion necessary to provide gain.

Several requirements need to be fulfilled for optical gain to be realized. First, the k-selection rule must be met, i.e. the momentum of the electrons and holes must match for a radiative recombination event to occur. Second, impurities that result in deep level traps within the forbidden energy gap must be minimized because they will compete for the excited electrons. Third, the photons that are emitted, as result of radiative recombination, must be confined to the gain region containing a high density of inverted carriers. Finally, this inversion is obtained by electrical injection of electrons into the conduction band of a p-type material that contains a high population of vacancies in the ground state (holes).

The first, second, and third requirements are easily satisfied through proper material selection and device design. The k-selection rule is met by using direct bandgap semiconductors, in our case gallium arsenide (GaAs). The second requirement is met by using a p-doped material in the gain region for greatest gain efficiency. Injection of minority electrons into the p-type gain region ensures high probability of radiative recombination since there is already an abundance of holes The third requirement of confining the created photons to the gain region, is fulfilled by waveguiding the optical wave within the gain medium. This means that the gain region must possess a higher index of refraction than the adjoining regions. This index is adjusted in the vertical dimension by substituting aluminum for gallium during the crystal growth to form

$Al_xGa_{1-x}As$ where x is the molar fraction of aluminum in the crystal. The resulting index of refraction is related to the volume fraction (x) by the empirical formula

$$n(x) = 3.590 - 0.710x + 0.091x^2 \tag{2.1}$$

Samples used in this study contained $Al_xGa_{1-x}As$ cladding layers that had $x=0.20$. Confinement in the horizontal dimension can either be done by directly fabricating a fixed index profile across the device or by generating a nonlinearly induced spatial index profile with a self-focused wave. To satisfy the final requirement of having a spatially localized carrier inversion, a forward biased injection diode is used. Additionally, the use of the higher bandgap AlGaAs for the cladding layers has the effect of confining the electrons within a potential well located across the intrinsic region. The resulting structure and refractive index profile is shown in Figure 2.1. This type of device is called a double heterostructure device due to the n and p doped $Al_{0.2}Ga_{0.8}As$ along with the intrinsic GaAs region. The gain region in the actual structure was grown undoped because the optical quality of undoped GaAs is far superior to that of p-doped GaAs. On the other hand the efficient diffusion of holes across the p-doped AlGaAs layer ensures that the gain medium effectively contains a large population of holes for efficient recombination.

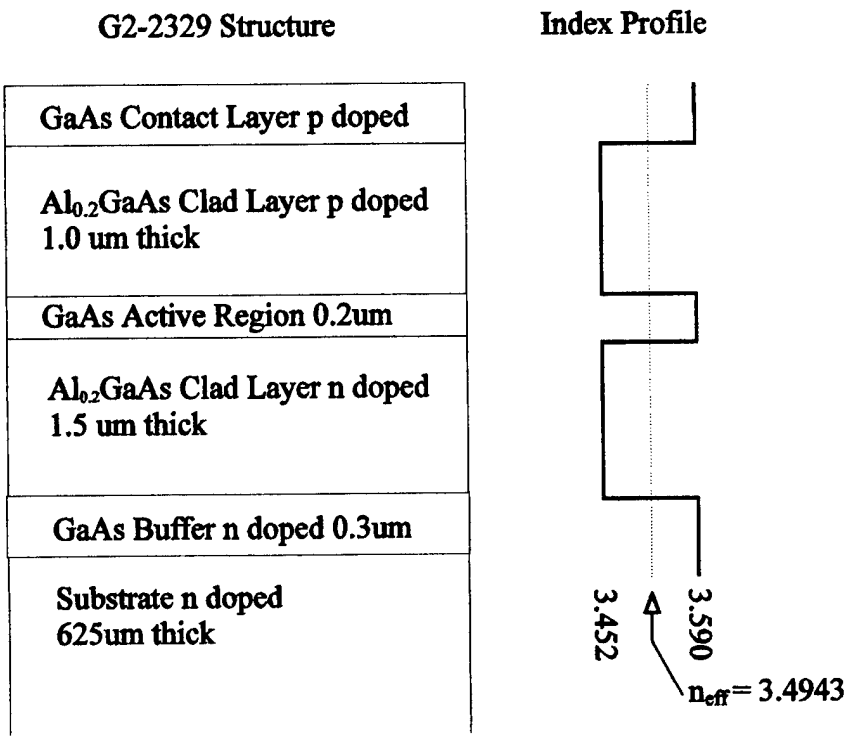

Figure 2.1 Cross section of the semiconductor optical amplifier. Right graph shows index profile of stack.

To describe the operation of this device, we must compare the band diagrams of the static and electrically pumped diode. When n and p regions of a diode are connected through a metallurgical junction, the holes in the p region diffuse to the n side and electrons in the n region diffuse to the p side leaving a depletion region, void of free carriers, between the two materials. This process, however, leaves unbalanced donor ions or net positive charges in the n region and unbalanced acceptor ions or net negative charge in the p region. This resulting space charge field restricts further diffusion of holes and electrons and equilibrium results. The addition of an intrinsic region between n

and p layers extends the length the depletion region. This condition is depicted in Figure 2.2a. When an external electric field is applied to the device, the depletion region grows for reverse bias or shrinks for forward bias. It is assumed that the externally applied electric field is dropped exclusively across the intrinsic region. When a large enough forward bias is applied, the region becomes very small, and holes and electrons easily diffuse across the junction and recombine. This condition is called the forward biased condition, shown in Figure 2.2b. As more forward bias is applied, the bands continue to move such that the field is dropped across the intrinsic region, the device eventually enters a degenerate state, Figure 2.2c. In this state, an excess of electrons exists locally with an excess of holes, creating an inversion.

2.1.2 OPTICAL CONFINEMENT

To design an efficient optical amplifier, the beam propagation in the slab (vertical) dimension must be determined. Treating the amplifier as a symmetric slab waveguide in the TE polarization state, we set the boundary conditions across the gain region and infinity points then solve the continuity equations to derive the transcendental equation relating the effective index and size of the gain region.

$$tan(\kappa h + m\pi) = \frac{\kappa(p+s)}{\kappa^2 - ps} \tag{2.2}$$

where h is the actual thickness of the guiding layer, m is the order of the propagated mode, $\kappa^2=n_f^2k_{vac}^2 - \beta^2$, $s^2=\beta^2-n_c^2k_{vac}^2$, and $p^2=\beta^2-n_s^2k_{vac}^2$. Within these equations, n_f is the

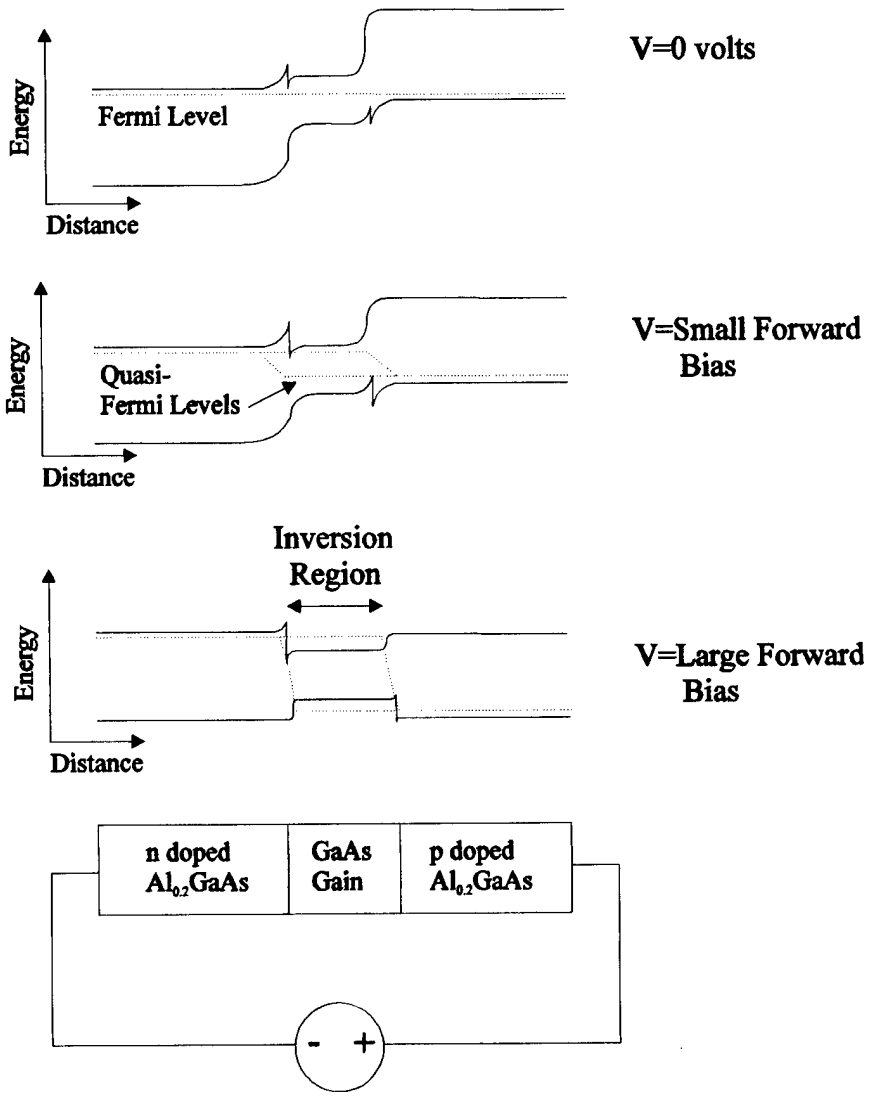

Figure 2.2 Band Diagram of a Double Heterostructure Amplifier. Top diagram (a) no bias. Middle diagram (b) small forward bias and bottom diagram (c) large forward bias.

index of refraction of the guiding layer, n_c is the index of the top cladding layer, n_s is the index of the lower cladding layer, k_{vac} is the vacuum wave vector of the optical wave, and β is the propagation constant of the wave inside the waveguide. β relates to the effective index of refraction of the waveguide by $n_{eff}=\beta/k_{vac}$. To ensure a single mode device, a thickness must be selected that is below the minimum thickness required for the m=2 mode. Additionally, to achieve the largest nonlinear action requires maximizing the optical intensity within the active region by making the guided region as small as possible, while also maximizing the overlap of the nonlinear region with the guided wave by making the guided region as large as possible. Maximizing these divergent requirements is accomplished by minimizing the effective thickness given by

$$h_{eff} = h + \frac{1}{s} + \frac{1}{p} \tag{2.3}$$

where h, s, and p are as defined previously. For the parameters used to design the devices used in this research, this formula minimizes at a thickness of 0.2 microns.

Although lateral confinement by solitary wave propagation is studied in Chapters 4 and 5, device characterization outlined in Chapter 3 required a two-dimensionally confined single mode waveguide design. The single mode confinement in the vertical dimension, as described above, is accomplished by fabricating the appropriate AlGaAs – GaAs layers during the MBE growth. Confinement in the horizontal direction is achieved by delineating a ridge waveguide. The propagation index of this structure is

found by using the effective index method. In this method, infinite slab waveguides are assumed for each of the propagation regions, the effective index is calculated for each, then a slab mode in the orthogonal direction is analyzed using these calculated refractive indices. The index profile for the ridge waveguide is formed by partially etching the top AlGaAs clad layer from the surface of the wafer. The deeper the etch, the lower the index of refraction for the area below the etch. The effective index in each of these slabs can be calculated by altering the boundary conditions for the top layer. Instead of assuming the field exponentially decays to zero in the top clad layer, we allow some of the field to enter the regions above the cladding layer. An alternate method of calculating the effective index in multiple layer systems is to evaluate the transmission using ABCD matrices through a multiple layer stack at differing angles. Propagation modes appear as resonant spikes in the transmission. Using this method, the index of refraction vs etch depth of our one micron upper cladding is shown in Figure 2.3. Computer code used for this method appears in appendix C.

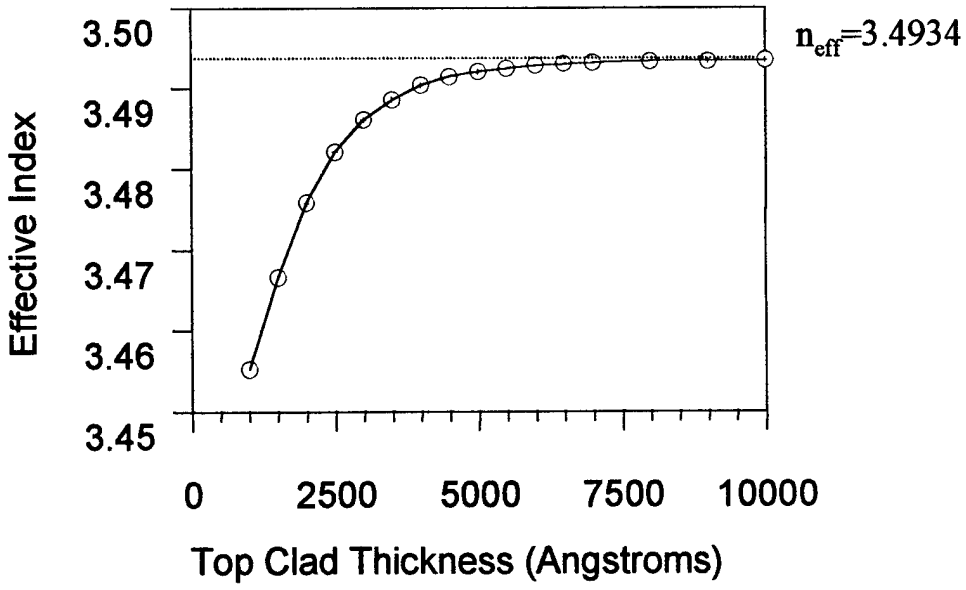

Figure 2.3 Dependence of effective index on top clad layer thickness. ns=3.45164, nf=3.59 df=0.2 um, nc=3.45164 thickness varies, top=air.

Using these design constraints, a wafer was grown using a Varian 360 Molecular Beam Epitaxy (MBE) chamber at the Air Force Wright Laboratories, Dayton OH. Structure as grown is shown in Figure 2.1. The buffer layer shown in this figure helps prepare the wafer surface for high quality epitaxial growth and reduces dislocation diffusion. This layer has no optical function.

2.2 FABRICATION

The devices used in this research were fabricated at CREOL using our class 100-cleanroom facility. An overview of the steps used for fabrication is shown in Figure 2.4. Each of the steps was developed for this clean room and a compendium of the fabrication follows below. The first step (not needed for the devices used in self-guiding

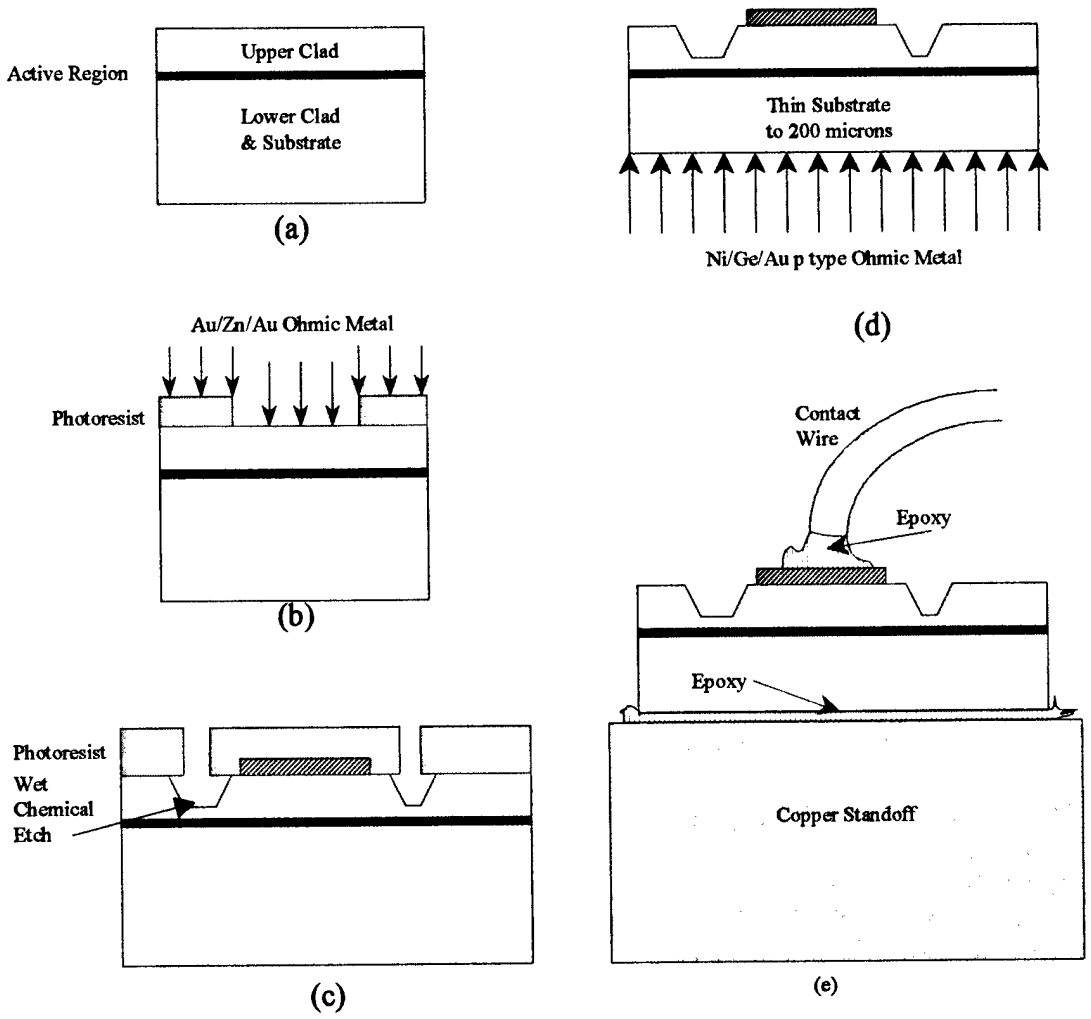

Figure 2.4 Fabrication Steps for Device Soliton Device

experiments) involved the formation of a ridge waveguide by wet chemical etching. Following this, a p-type top ohmic contact was applied using thermal vacuum evaporation. In some devices, current isolation trenches were required, and these were formed by wet chemical etching on either side of the p-type ohmic contact. Next the sample was thinned down to 200 microns to facilitate cleaving. After thorough cleaning,

an n-type ohmic contact was applied to the entire backside of the wafer. After this metallization, the wafer was cleaned and rapid thermal annealed to form the eutectic alloy ohmic contacts. Finally, the sample was cleaved to form clean facets for end-fire optical coupling and mounted on a copper post using conductive epoxy to enable an electrical contact to the n side of the sample and to permit efficient removal of heat generated in the active amplifier. Each of the tools used in this fabrication procedure is described separately below.

2.2.1 PHOTOLITHOGRAPHY

Regions for different processing were defined using photoresist and photolithography. In this process, a photoactive polymer liquid, the photoresist, is applied to the sample and spun at high speeds to forma thin uniform layer. The layer is cured, then selectively exposed to UV light using contact masks and a Karl Suss MJB-3 mask aligner. The MJB-3 delivers 25 mW/cm^2 at 405 nm (G line) and 18 mW/cm^2 at 365 nm (H line). The layer is developed (selectively removed) using a liquid developer. This process results in precise openings in a resistant polymer photoresist coating. These openings define the sections of the wafer affected by subsequent processing. The photoresists used in this work are as follows.

Shipley 1400-17: This is a thin positive photoresist best suited for high precision work to fabricate structures with feature sizes approaching 1 micron. It is best suited for wet chemical etching, and performs poorly for metal liftoff. The photoresist thickness is

4500Å using a 3000-rpm spin speed for 30 seconds. The photoresist is partially cured (soft-baked) at 100°C for 5 minutes on a hot plate. The optimum exposure time with the MJB-3 is 1.6 sec followed by a 30 second develop in one part Shipley 351 developer mixed with five parts water. After successful developing, the resist must be hot plate baked for 5 minutes at 100°C for more complete curing. The resist may delaminate without this post bake, especially in wet chemical etches.

Shipley 1823: This is a medium positive photoresist best suited for moderate precision work to realize structures with dimensions of 2-3 microns and larger. It is the best general-purpose photoresist, well suited for ohmic contact metal liftoffs. However, it may not be suitable for liftoff of thick metals or metal plating. The resist thickness is 1.3 microns using a 3000-rpm spin speed for 30 seconds. It cures at 119°C for 5 minutes on a hot plate. Exposure time with the MJB-3 is 3.5 seconds followed by a 30 second develop in one part Shipley 351 developer mixed with six parts water. After successful developing, the photoresist must be hot plate baked (post-baked) for 5 minutes at 119°C. The resist may delaminate without the post bake, especially in wet chemical etches. This resist is made by mixing 24 parts Shipley 1827 resist with 5 parts Shipley type p thinner, then gently mixing for 5 minutes. Appropriate care must be taken to ensure that mixing does not induce bubbles into the polymer liquid.

Shipley 1827: This is a thick positive photoresist that is useful for thick metal liftoffs and plating. This resist is unsuitable for high precision work. A photoresist thickness of 2.5 microns is obtained using a 3000-rpm spin speed for 30 seconds. Soft baking is performed at 119°C for 5 minutes on a hot plate. The optimum exposure time is 8

seconds with the MJB-3. Develop and post-bake are identical to the Shipley 1823 photoresist.

Edge Bead: A problem with using partial wafers is the formation of photoresist edge beads. Spinning any photoresist on a wafer without beveled edges causes an edge bead to form. The bead is several microns in thickness above the applied photoresist and extends for 10-20 microns from all edges. The bead impedes the direct contact of the center part of the wafer and the photomask causing fuzzy, undefined shadow exposures. This results in poor edge definitions in structures approaching one to two microns. The effect is not as detrimental to structures exceeding five microns. Although mechanical tools exist to remove edge beads, these are not available at CREOL. The beads can easily be removed, however, if positive photoresist is used. To remove the bead, the center portion of the wafer is covered and the edges are overexposed for 60 seconds. Because positive photoresist is not removed, or effected, unless exposed, the wafer can be developed using standard developer. After developing, the wafer is rinsed in deionized water for one minute and dried. Hot plate baking is not required between this step and subsequent exposure-develop cycles.

2.2.2 WET CHEMICAL ETCHING

After masking the substrate, the exposed areas can be thinned by using wet chemical etching. To be effective in forming the waveguides used in this research, the wet chemical solution must uniformly etch both GaAs and AlGaAs and must not be selective

in crystal plane orientation. The solution used was one part phosphoric acid (H_3:PO_4) at 1 molar concentration, two parts hydrogen peroxide (H_2O_2) in a 30% solution with water, and 50 or 100 parts deionized water. The etch rate in p doped GaAs and AlGaAs was 1850Å/sec for the 1:2:50 solution, and 1100Å/sec for the 1:2:100 solution. For best results, the solution was stirred after combining the constituents and allowed to stabilize for five minutes prior to use. Etching solutions were not re-used after four hours. Temperature variations also impacted etch rates significantly, and the etch rates reported here are for solutions at 23°C.

2.2.3 PLASMA PROCESSING

In plasma processing, materials can either be removed or deposited through the use of plasma exposure. Plasma processing enables material removal or deposition not available by other means and in geometries not available by other means. For example, organic polymers can be removed selectively leaving nearly a 90° sidewall. Or, silicon nitride can be deposited across the entire surface of a semiconductor wafer regardless of the shapes, geometries, or materials on the surface of the wafer. Both processes were accomplished in a PlasmaTherm 790 dual chamber plasma processing system. In this research, the plasma processing was used in three processing steps: oxygen descum, deposition of the dielectric layer silicon nitride, and selective removal of silicon nitride.

2.2.3.1 OXYGEN DESCUM

Ideally, after a photolithographic step where openings are created in an organic photomask, the openings are totally clear of any organic residue. In practice, however, a very thin film, usually less than 100Å thick, of organic residue, or scum, frequently remains. The film is not visible under a microscope, but the film causes metals to delaminate after vacuum metal deposition, or non-uniform wet chemical etches due to areas of organic scum. Removal of this material is termed a descum step.

Various methods exist to remove this film including a dip in very dilute ammonium hydroxide or exposure of the material to a weak oxygen plasma. The ammonium hydroxide method potentially can damage the substrate and is very isotropic, meaning that the openings in the photoresist will become slightly distorted as the ammonium hydroxide removes material from the side walls of the openings as well as from the open areas themselves.

The oxygen plasma descum method overcomes these shortcomings. First, the weak oxygen plasma is reactive only to organic materials, thus inorganic semiconductors, dielectrics, and metals are not affected. Second, plasma chemistry, pressure, and power combinations exist that are very anisotropic meaning that material is removed from flat surfaces, but not from sidewalls. Even though material is removed from all flat surfaces, including the areas that should be covered, the removal represents only a small fraction of the total resist thickness. In a typical descum step, 100Å of organic photoresist is removed from a layer that started at between 5000Å and 15000Å thick.

Organic removal by oxygen plasma requires that oxygen radicals, created in a plasma, contact the surface of the organic material and form volatile compounds such as carbon dioxide and water. In the PlasmaTherm 790 system, 13.8 MHz RF excitation between two parallel plates in the plasma chamber excites the plasma. A DC bias applied between the plates accelerates the plasma radicals towards the lower plate where the samples are. As the acceleration is directionally vertical, etch profiles tend to be anisotropic in the vertical direction. The addition of a light carrier gas, such as helium, to the plasma controls the oxygen radical concentration and aids in the mechanical removal of materials thereby increasing the anisotropic nature of the etch. Chamber pressure, gas concentration, and power primarily control etch rates, while gas flow rate controls uniformity. Figure 2.5 shows the characterization of three oxygen etch setups on organic photoresist. In this figure, the descum process, used as a mild removal of trace organics prior to metalizations or etches, is the slowest etch. The anisotropic etch process is designed as an anisotropic removal of photoresist. After etching through 1.5 microns of photoresist with the anisotropic process, no discernable increase in opening size was measured. Finally, the ash process is designed as a cleaning or blanket removal of all organic materials on the surface of a substrate.

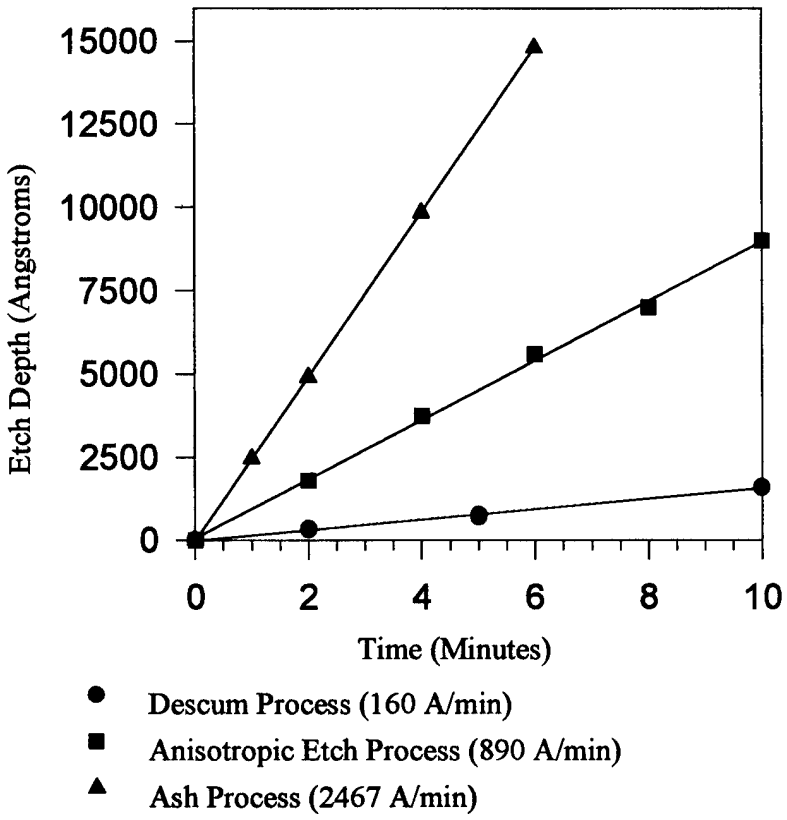

Figure 2.5 Etch Rate of Three Polymer Etch Processes: Descum, Anisotropic[65], and Ash Processes.

2.2.3.2 SILICON NITRIDE DEPOSITION

The devices used in this research require ohmic contact only over the active region, typically the size of the waveguide: four to 50 microns. This ohmic contact's size makes electrical contacting nearly impossible. Placing a large metal contact pad and metal current pathway over the ohmic contact permits current flow and contacting, however, any metal contact directly to the p-side of the wafer causes current leakage. To overcome

this, a dielectric layer is inserted between the contacting pads and substrate. This layer is created by blanket coating the entire surface with the dielectric, then selectively removing the dielectric above the ohmic contacts. Following this, the metal contact pads can be deposited without contacting the substrate.

Two processes were designed to create the dielectric layer. The first was to spin coat a polymer glass suspended in a carrier solvent, spin on glass, to the wafer. The carrier solvent was evaporated by hot plate baking the wafer at 100°C for 5 minutes, leaving an amorphous gel on the surface of the wafer. The wafer was then heated to 350°C for 30 minutes to cure the gel into a hard, inorganic silicon dioxide cap layer. Although spin on glasses from two venders were tested using a variety of application techniques, the silicon dioxide layer created using this technique delaminated from the wafer during the final thermal processing stages of ohmic contact formation.

The second method proved successful. In this technique, the substrate is patterned with waveguides. Prior to patterning the top ohmic contact, a uniform layer of silicon nitride was applied to the wafer using a PlasmaTherm 790 chemical vapor deposition system. In the system, silane, SiH_4, and ammonia, NH_3, gasses combine in a plasma. Silicon radicals combine with nitrogen radicals forming silicon nitride, Si_3N_4.

$$3SiH_4 + 4NH_3 \rightarrow Si_3N_4 + 12H_2 \qquad (2.4)$$

Although the silicon nitride deposits on the first surface it contacts, the substrates are heated to 250°C to help create uniform coatings and relieve deposition stress.

Adjusting the ratio of silane to ammonia can control the index of refraction in the resulting film from 1.85 to 2.2. Figure 2.6 shows the relationship between index and the silane to ammonia ratio. Control of the refractive index is useful in antireflective coatings, but does not provide practical control for dielectric insulators. Silicon nitride films grown in this research have a ratio of approximately 1.9.

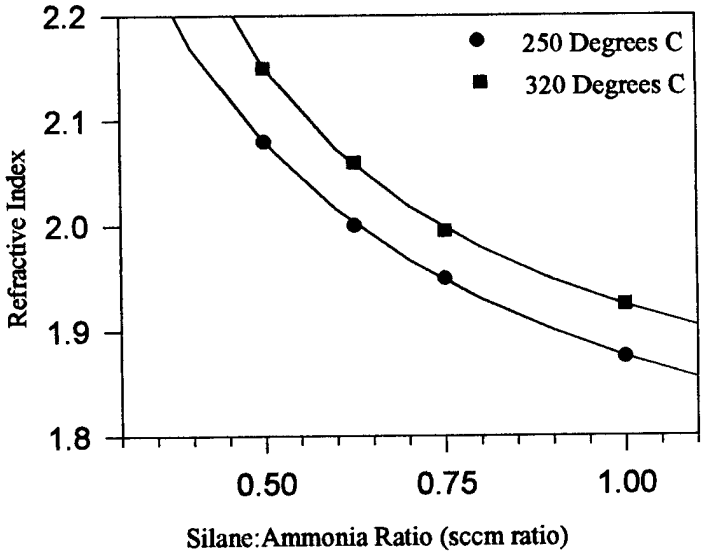

Figure 2.6 Dependence of Refractive Index on Growth Temperature and Silane/Ammonia Ratio[66]

The deposited silicon nitride films coat uniformly to most geometries, and adhere to all materials used in this fabrication including photoresist, semiconductors, and metals. Figure 2.7 shows an electron beam microscope photo of a typical conformal silicon nitride coating shown as a dark band, along the side of a waveguide ridge.

Figure 2.7 Electron micrograph of a uniform silicon nitride layer coating the sides of a laser diode ridge. Silicon nitride layer (arrows) appears as a dark black layer between the substrate and top contact metal.[67]

Deposition rates are dependent on RF plasma power. Uniformity depends on deposition and flow rates. Figure 2.8 shows the deposition rates of two silicon nitride deposition processes. The rate increases from 74 Å/min for the 20-watt plasma to 157 Å/min for the 100-watt plasma.

Residual stress in the film can be changed from tensile to compressive by adding varying amounts of helium to the plasma. Tensile stress in films deposited without helium at 13.56 MHz is in the range of 2.5×10^9 dynes/cm^2. By increasing the ratio of helium to nitrogen in the gas mixture used to deposit silicon nitride, the film stress can be controlled from tensile, through zero, to compressive. For a 100-watt plasma, a ratio of 30% nitrogen and 70% helium will produce a no stress film.[68]

Facilities to measure the index of refraction and stress of these films was not available at the time this work was preformed, thus, the system was not characterized for these parameters.

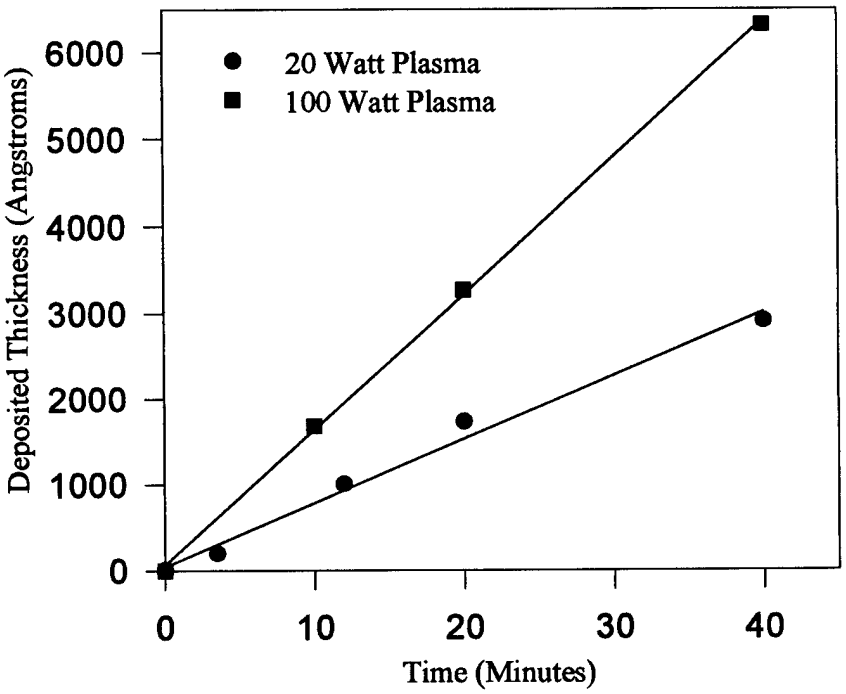

Figure 2.8 Deposition Rate Dependence on Plasma Power

2.2.3.3 SILICON NITRIDE ETCHING

Once a uniform silicon nitride layer was deposited over the substrate, a photomask as patterned over the nitride and the nitride removed. This exposed the area requiring ohmic contacts to the surface of the sample, thus the photomask used to pattern the silicon

nitride was also used to pattern deposited ohmic metal onto the substrate. This is termed a self-aligned process.

Wet chemical and plasma etching processes were studied to measure etch rates. In the wet chemical procedure, buffered oxide etch consisting of hydrofluoric acid and sodium fluoride was diluted with deionized water 1:5. Samples were immersed in the etching solution, then rinsed with deionized water for two minutes. This method produced etch rates of 951Å/min for the 20-watt plasma film, and 1012Å/min for the 100-watt plasma film.

Plasma etching was preformed using a mix of 92% $Freon_{14}$ and 8% oxygen cleaning gas in a 20-watt plasma. The etch rate for the 20-watt plasma film was 411Å/min. The etch rate for the 100-watt film was 461Å/min.

2.2.4 METALLIZATION

Electrical contact is made to the samples by selective deposition of a series of metals that, when annealed, combine with the surface of the semiconductor and form a layer without a potential barrier. The contacts exhibit only small resistance and are called ohmic contacts. The contact used for p-type GaAs is 50Å gold: 200Å zinc followed by 2000Å of gold. The contact used for n-type GaAs is 50Å nickel: 200Å germanium, and 2000Å gold. The samples were annealed only once at 420°C for 120 seconds in a rapid thermal annealer. Non-ohmic contact pads were deposited after the anneals, and were comprised of 50Å titanium: 200Å platinum: 2000Å gold. In these contacts, the titanium

formed an adhesion/wetting layer, the platinum formed a gold diffusion barrier, and the gold was the high conduction contact layer.

To form good ohmic contacts, surface preparation was critical. All photoresist and oxides must be removed from the area of deposition. To remove photoresist, an oxygen plasma descum should be used. This comprises the exposure of the sample to a low power oxygen plasma to remove 50-100Å of surface polymer uniformly across the wafer. Following the descum, the surface oxides are removed by dipping the wafer in a solution of one part buffered oxide etch with 50 parts water for 30 seconds. This gentle oxide etch removes surface oxides formed by exposure of the wafer to atmosphere and during the descum procedure. After the acid etch dip, the wafer is rinsed for 2 minutes in a flowing deionized water bath, then thoroughly blow dried with nitrogen. The sample is then immediately loaded into the metallization chamber without further heating. Heating will form additional oxides.

Following metallization, the sample was soaked in acetone for an hour to dissolve the photoresist on the surface of the wafer. This caused the metal covering the photoresist to peal off the surface of the wafer leaving only the metal in the exposed areas. The edges of the remaining metal pads possessed "wings" formed when the metal broke from the metal over the photoresist. Moving the sample to a clean beaker of acetone and using ultrasound for 1 to 5 minutes removed most of the "wings". A Cole-Parmer ultrasonic cleaner was used because it provided a lower ultrasound intensity than other units such as the Fisher ultrasonic cleaner that has been found to delaminate the metal pads and on occasions, even shatter samples.

2.2.5 THINNING AND CLEAVING

In this research, optical beams were launched into the devices using the end-fire coupling technique. End-fire coupling requires a highly polished and flat interface. Fortunately, the use of crystalline semiconductors provides an easy method of forming these near-perfect optically flat facets, namely cleaving. In the cleaving process, a small guide nick or short scribe mark, about ½ millimeter, is made on the front of the wafer perpendicular to the edge of the substrate. The direction of the nick must be nearly parallel to a crystal plane. Application of point pressure immediately behind the nick, on the backside, causes the wafer to split along the nearest primary crystal plane, starting at the nick point. Cleaving the wafer prior to fabrication permits the alignment of processed structures to the cleavage planes.

During fabrication, wafers require mechanical strength to avoid breakage. As such, wafers are typically 625 microns thick. This is advantageous for keeping the wafer whole during fabrication, however it makes cleaving difficult. In order to get better cleaves, wafers are thinned to 200 microns after the majority of processing is completed. Once thinned to this thickness, wafers are very fragile and must be handled delicately. The first step in the thinning process is to mount the wafer face down to a lapping block using an acetone soluble wax called crystal bond. Measuring the starting thickness of the wafer and lapping flat combination provides the reference point to determine the extent

of the thinning. Then the lapping flat is mounted to a stabilized lapping fixture, which holds the flat parallel to the lapping surface. This fixture rides on a South Bay Technology, Model 920 lapping table covered with a slurry of 10 micron alumina power and water. Removing 400 microns of material requires about 20 minutes, and the thickness is checked regularly. Once the thickness nears 225 microns, the lapping flat is removed from the fixture, and the substrate is cleaned. The 10 micron lapping slurry leaves a rough, flat, gray surface comprised of scratches. These scratches interfere with the cleaving and are removed by manual polishing using finer grit material. The wafer-fixture combination is moved in a figure 8 motion along a polishing pad covered with a slurry of 0.3 micron alumina in a mixture of 1 part Clorox bleach with 10 parts water. The surface of the wafer becomes shinny and free of scratches within 10 minutes. The wafer is thoroughly rinsed with water, then soaked in acetone until the wafer separates from the lapping flat.

At this point the exposed n-type backside of the wafer is mounted on a carrier glass slide and metallized with an n-type ohmic contact. After metallization, the wafer is detached from the glass slide, and thoroughly cleaned. To establish the substrate ohmic metal contact, the wafer is rapid thermal annealed for 120s at 420°C, which completes the fabrication process. Using the cleaving process described above, the sample is cut to the required length.

2.2.6 MOUNTING

The amount of electrical current passing through these devices causes a significant thermal load. Removing the heat, as well as making electrical contact to the backside of the samples, requires secure mounting onto an electrically and thermally conductive post. These posts were fashioned from 1mm thick copper sheets and milled to the required dimensions. In cases where a wide sample was used, the mount was formed by joining two sheets together using thermally cured conductive epoxy. In both situations, once the platform was fabricated, a thin coat of Epotech H20E epoxy was applied to the mounting area of the stud, and the sample was carefully placed into this epoxy ensuring that the epoxy did not wick up onto the facets of the sample. Heating the stud/sample to 125°C for 30 minutes permanently cured the epoxy and fixed the sample to the stud.

Electrical contact to the pad on the p-side of the sample was done using 0.3 mill (50μm) diameter gold wire. These wires were attached simultaneously to the device and an insulated standoff, which was mounted to the copper stud, using the same conductive epoxy used to attach the sample to the stud. A pair of tweezers mounted on a 3-axis positioner held the wire in place while the epoxy was heat-cured. To provide uniform current injection into the device, multiple wires were used for the p-side contact. The device-stud combination could then be mounted into the test fixture for evaluation. Figure 2.9 depicts a cross section of a wide device mounted on a T-stud and attached to the water-cooled testing fixture.

Figure 2.9 Photograph of a mounted sample containing 16 devices. n side contact is made through copper standoff. p side contacts are made with thin wires and insulated bonding pads shown to either side of the sample.

CHAPTER 3: CHARACTERIZATION

Determining a wafer's characteristics is important not only to avoid wasting time fabricating devices from material that is unsuitable for testing, but also to provide the necessary parameters to analyze experimental results. Additionally, the growth of semiconductor materials remains as much art as science, and each set of wafers grown at different times will invariably have different characteristics. Optical and electrical characterization techniques are designed to determine these variables.

3.1 PHOTOLUMINESCENCE CHARACTERIZATION

To achieve the best gain, our devices required a well-grown GaAs intrinsic region, free of major defects and compositional alterations, between the n and p doped AlGaAs cladding regions. To quantify the quality and growth composition, as well as the spectral dependence of the gain peak with carrier injection of this intrinsic layer, the photoluminescence and electro-luminescence techniques were used.

3.1.1 PHOTOLUMINESCENCE

In the photoluminescence measurement, excited carriers create electrons in the conduction band and holes in the valence band of the semiconductor, using an incident pump beam with photon energy greater than the bandgap of the semiconductor. In this case, a 3 mW HeNe laser emitting at 632.8-nm wavelength was used as the excitation source. The electrons in the material absorb the incident pump, and are raised in energy into the conduction band. As (thermal) phonon transitions within the conduction band occur 1000 times faster than the radiative decay of these electrons due to band-to-band transitions, electrons excited above the band edge rapidly settle to the base of the conduction band and then recombine with holes thereby creating photons. Vibrational broadening causes a Gaussian energy distribution around the bandgap energy with the peak remaining at the bandgap. The number of carriers excited into the conduction band stays relatively small, thus band renormalization experienced with high current injection is negligible. This allows an unperturbed measurement of the bandgap energy. The unperturbed bandgap of GaAs at room temperature is 1.425 eV corresponding to a wavelength of 870 nm; quantum effects are not expected with a gain region width of 0.2 microns.

The photoluminescence photons emitted from the intrinsic gain region pass through the AlGaAs clad layers, which are transparent to the incident photons because the AlGaAs bandgap is larger than the photoluminescence photon energy. The photons that are emitted from the sample in a Lambertian distribution are collected and focused into

the entrance slit of a spectrometer. A schematic of this experiment is illustrated in Figure 3.1.

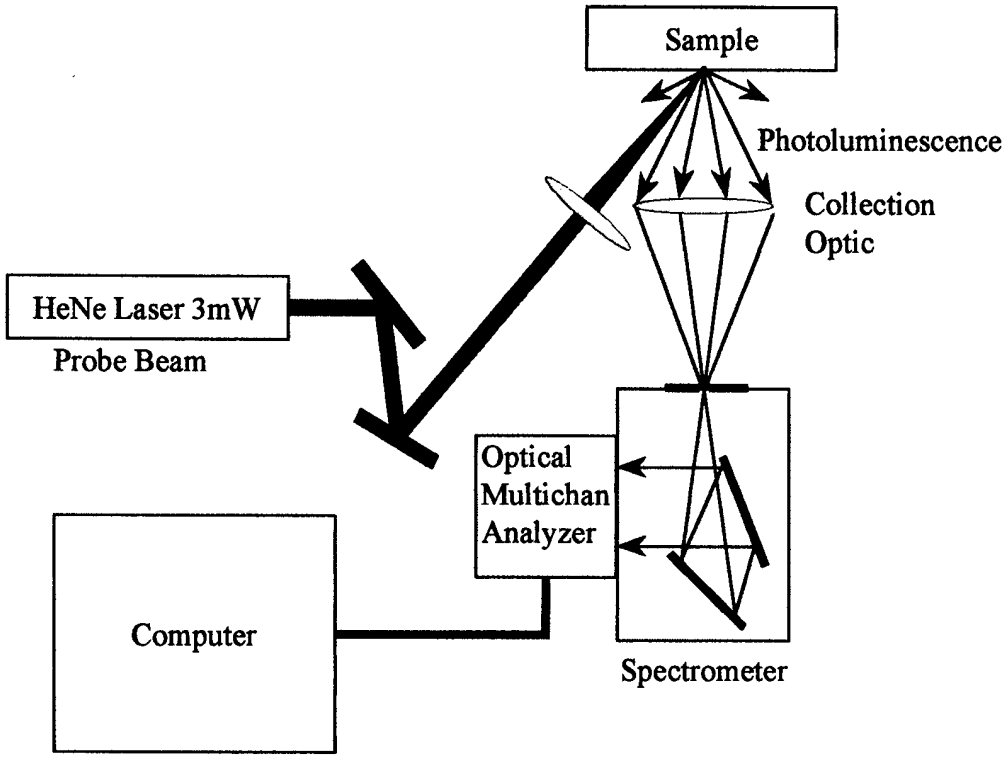

Figure 3.1 Photoluminescence Measurement

Although the emitted photons from the active region will pass out of the material without being absorbed by the $Al_{0.2}Ga_{0.8}As$ upper cladding region, the inbound 632 nm pump laser will be absorbed and may not penetrate to the gain region. Additionally, because the $Al_{0.2}Ga_{0.8}As$ upper cladding region does not absorb the photons that are emitted from the GaAs active region, it will efficiently absorb the excitation photons provided by the 632nm HeNe laser and prevent them from reaching the active region. To enhance the photoluminescence measurement, the top GaAs contact layer and 50% of the AlGaAs cladding layer were removed using wet chemical etching.

Using a three-milliwatt HeNe laser to excite electrons in the gain region, the photoluminescence spectrum shown in Figure 3.2 was obtained. The peak of the spectrum lies at 868 nm as would be expected; theory predicts 870 nm. To determine how the spectrum behaves at higher temperatures, the photoluminescence spectrum was re-measured with sample heated to 80°C.

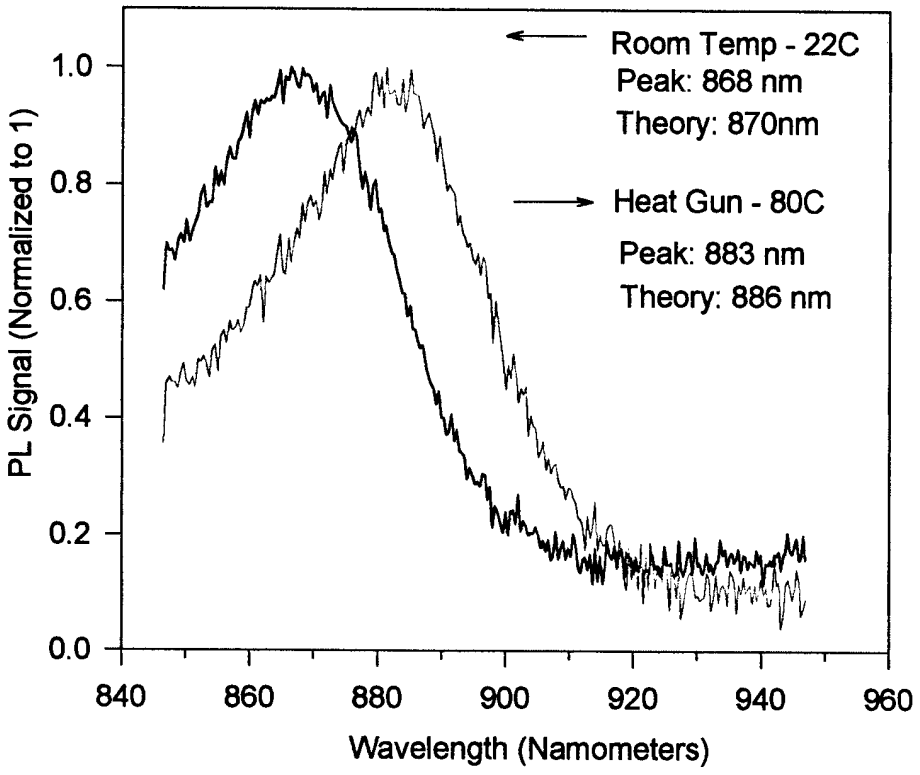

Figure 3.2 Photoluminescence Spectra of G2-2329 at Room Temperature (22°C), left trace, and at 80°C, right trace.

As shown in Figure 3.2, the peak of the photoluminescence spectrum of the heated sample lies at 883nm. Semiconductor bandgaps follow the Varshni empirical fit equation, equation 3.1.

$$\xi_g(T) = 1.519eV - \frac{5.405x10^{-4}(\frac{eV}{^\circ K^2})T^2}{T + 204^\circ K} \tag{3.1}$$

where the Varshni fit parameters for GaAs have been entered into this equation 3.1. At 80°C, this equation predicts that the photoluminescence signal should peak at 886nm. This is in good agreement with our measured value of 883nm. These measurements confirm that the material within the gain region is good quality intrinsic GaAs.

3.1.2 ELECTRO-LUMINESCENCE

A second analysis technique is electro-luminescence. Electro-luminescence characterizes the spectral nature of the semiconductor amplifier's gain. In this technique, the output of a laser diode fabricated from the material under characterization is spectrally analyzed at varying injected carrier levels as shown in Figure 3.3. The carriers are injected electrically into the gain region of the diode, and recombine with the holes injected from the opposite side thereby creating photons.

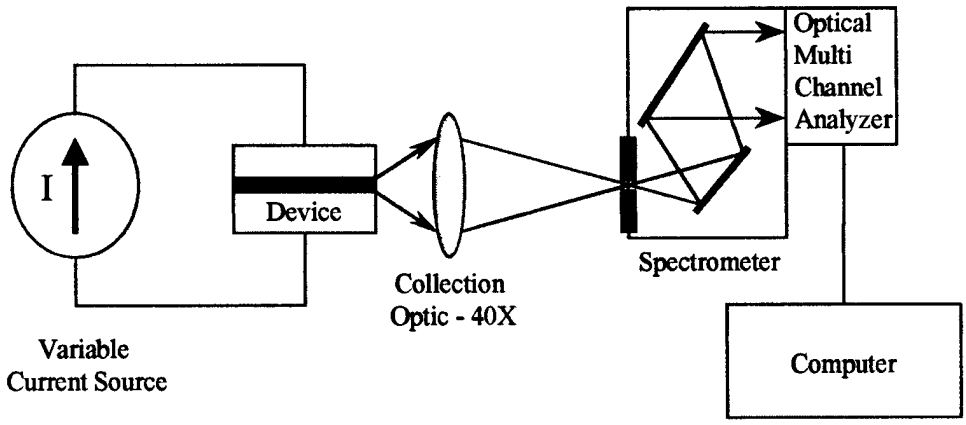

Figure 3.3 Electro-Luminescence Measurement Configuration

Under forward biased conditions, the quasi Fermi levels shift towards their respective bandedges, and eventually become degenerate by crossing the bandedge. Using double heterostructure devices enhances this increase in population by physically restricting the diffusion of carriers in the vertical dimension through the used of higher energy bandgap AlGaAs layers on either side of the active region.

The degeneracy resulting from the respective quasi-Fermi levels approaching the bands, causes an effect called bandtailing. Bandtailing bends the parabolic band edges into the bandgap. This results in a narrowing of the bandgap and a concentration of carriers below the expected bandedge. Studies done show that bandtailing shifts the bandedge lower by as much as 100meV.[69] In GaAs, this shift in bandgap corresponds to a wavelength change from 870 nm to 935 nm. As more carriers are injected into the gain region, the quasi-Fermi level continues to move further into the conduction band. This movement causes the peak of the carrier concentration to reside at higher energies in the conduction band and lower energies in the valence band. Because the spontaneous

emission intensity depends on the gap between these peak energies, as the current is increased, the peak of the spontaneous emission spectra will also increase in energy.

More carriers injected into the bands provide a larger optical gain. Eventually this gain will overcome any losses, at which time the device will move into the amplification regime. If a resonant cavity exists, the device will begin to lase and the output spectrum significantly narrows. At this point, carriers are rapidly removed from the upper state by stimulated emission, and the quasi-Fermi levels no longer increase in energy.

Electro-luminescence measurements reveal the behavior of the shifts in peak wavelength of the emission versus current injection. The maximum gain available exists at the peak of the electro-luminescence spectrum. The behavior and location of this peak must be determined to find the maximum nonlinearity.

Electro luminescence experiments were conducted on a single mode, 4-μm wide waveguide, with an offset angle of 0.9° to the primary cleavage plane to frustrate lasing. The 0.9° inhibits lasing except at very high currents thereby permitting the study of the behavior of the device well within the degeneracy region. The device was cleaved to an overall length of 5 mm.

As shown in Figure 3.4(a), the low injection case, 130mA, produces a broad spectrum with a peak of 920 nm consistent with the expected reduction of the bandgap. Application of additional current, plots (b) through (d), fills available band states and shifts the wavelength to higher energies. Finally, the gain available in the device overcomes the angular slant of the output facets, and the device begins to lase, Figure 3.4 (e). Figure 3.4(f) shows the output optical power versus current for this device. By

graphical extrapolation, the lasing threshold current is deduced to be 650mA. Also shown in Figure 3.4(f) is a plot of the position of the peak of the electro-luminescence spectra with injection current. In the region below lasing threshold, the peak shifts linearly with the increase in current then shifts very slightly in the opposite direction at current levels above the lasing threshold. Remember that the quasi-Fermi levels no longer shift with increasing current injection. Thus the increase in the amplifier's peak wavelength after the onset of lasing is most likely be a result of device heating.

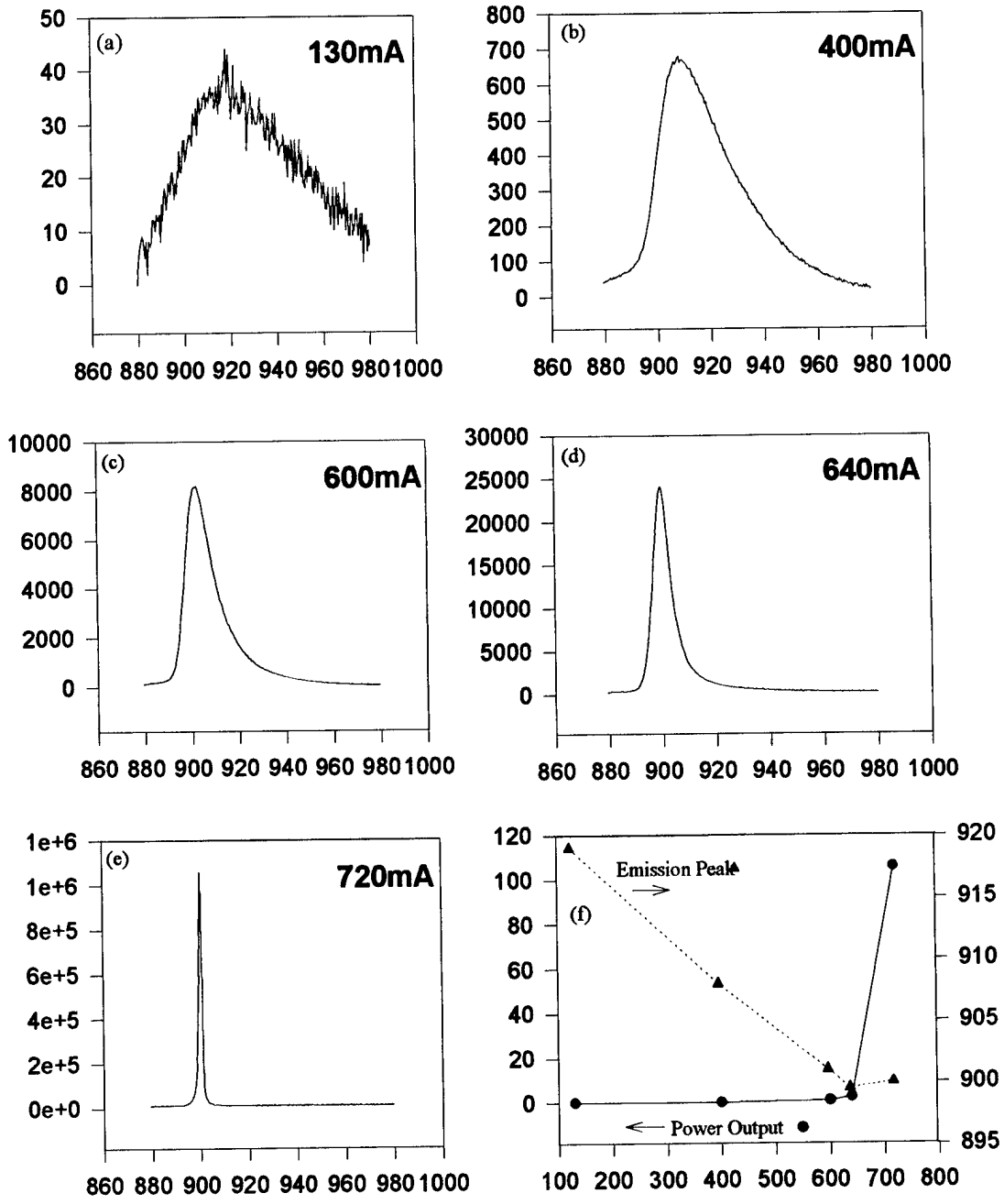

Figure 3.4 Electro-Luminescence Measurements on G2-2329 5.5mm long 4um wide waveguide. Plots (a) – (d) show spontaneous emission behavior, plot (e) shows the device after the onset of lasing. Plot (f) shows the output power and emission peak versus injection current.

3.2 MEASUREMENT OF GAIN SPECTRUM

Critical to the successful operation of the soliton device is the ability of an input optical beam to extract electrons from the conduction band thereby altering the carrier population. As discussed in section 3.1.2, the peak of the gain will follow the electro-luminescence peak, however, for a fixed current injection level, the magnitude of the gain will vary by

$$g(\xi) = \frac{\sqrt{2}(m_r^*)^{\frac{3}{2}} q^2 f_{CV}}{6\pi n_r \varepsilon_0 m_0 \hbar^2 c\xi} (\xi - \xi_g)^{\frac{1}{2}} \left[f_n(\xi_2) - f_p(\xi_1) \right] \tag{3.2}$$

where m_r^* is the reduced mass of the carriers in the gain region, f_{CV} is the oscillator strength of the transition from conduction to valence band (approximately 23eV for GaAs), n_r is the linear index of refraction which is 3.590 for GaAs, m_o is the electron rest mass, ξ is the energy where the gain is calculated, ξ_g is the unperturbed bandgap energy, and finally $f_n(\xi_2)$ and $f_p(\xi_1)$ are the values of the quasi Fermi functions at weighted energies ξ_2 for the conduction band and ξ_1 for the valence band. Equation 3.2 was developed in Chapter 1. Note that $\xi_2 - \xi_1 = \hbar\omega$, and the energies are set such that momentum is conserved by the transition. Using this equation is cumbersome, as the quasi Fermi functions require knowledge of the carrier concentration in the active region, which in turn, is directly proportional to the injection current. Assuming a quantum efficiency of unity, the carrier concentration is estimated by assuming that the injected

carriers recombine only in the active region with a characteristic recombination time τ_o, typically 0.6 nanoseconds for GaAs. Note that the lifetime used here is the combination of the spontaneous radiative and nonradiative recombination lifetimes. Thus the average carrier, electron and hole, concentrations are $N = \frac{qI\tau_0}{Ad}$, where I represents the injected current in amps, A is the cross sectional area of the topside contact, and d is the thickness of the active region. Next the quasi-Fermi levels, ξ_{fn} and ξ_{fp}, are found by fixing the valence band energy to zero and solving

$$\begin{aligned} \xi_{fn} &= \xi_g + kT\, ln\left(\frac{N}{N_c}\right) \\ \xi_{fp} &= -kT\, ln\left(\frac{N}{N_v}\right) \end{aligned} \tag{3.3}$$

where N_c and N_v are the effective density of states values for the conduction and valence bands respectively. In this case N_c=4.4x10^{17} /cm^3 and N_v=8.2x10^{18}/cm^3 were used. Now the Fermi distribution function can be evaluated using

$$\begin{aligned} f_n(\xi) &= \frac{1}{1+e^{\left(\frac{\xi-\xi_{fn}}{kT}\right)}} \\ f_p(\xi) &= \frac{1}{1+e^{\left(\frac{\xi_{fp}-\xi}{kT}\right)}} \end{aligned} \tag{3.4}$$

The last step, the weighted energies are calculated by maintaining the conservation of momentum in the transition.

$$\xi_2 = \xi g + \frac{m_r^*}{m_e^*}(\xi - \xi g)$$
$$\xi_1 = -\frac{m_r^*}{m_h^*}(\xi - \xi g) \tag{3.5}$$

The gain spectrum was measured by launching a beam through a single mode waveguide amplifier formed using a 4 μm wide waveguide electrically contacted at the top for carrier injection. The beam was end fire coupled into the waveguide using a 40x-microscope objective, and the output of the waveguide was focused onto a detector using a 20X-microscope objective. To isolate the gain from the spontaneous emission, the input was chopped and measured using a detector connected to a lock-in amplifier. The experimental set-up for this experiment is shown in Figure 3.5.

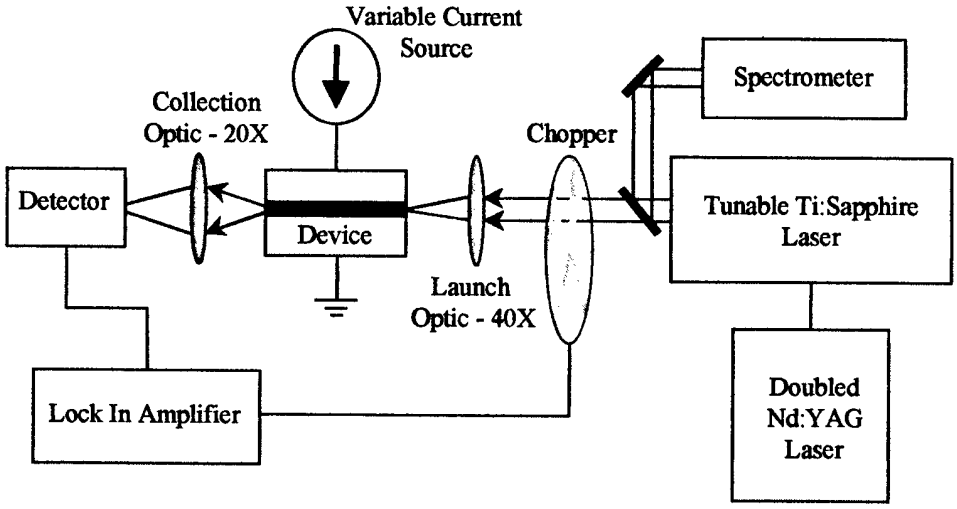

Figure 3.5 Experimental Setup for Gain Measurements

The absolute gain of this device could not be measured as there was no way of measuring coupling and cavity losses, however, the shape and spectral profile of the gain

are valuable in fitting to the model. Results of the measurement and a theoretical fit are shown in Figure 3.6. The modeled fit assumed unity quantum efficiency, oscillator strength of 46 eV, and a carrier lifetime of 0.6 ns. As described in chapter 1, the valence band quasi-Fermi level is a strong function of the hole injection from the AlGaAs cladding material. As such, the valence quasi-Fermi level is modeled as a constant energy of 10.5 meV above the valence band edge. This value was determined by best curve fit. Fitting parameters used here agree well with established constants for high quality GaAs.

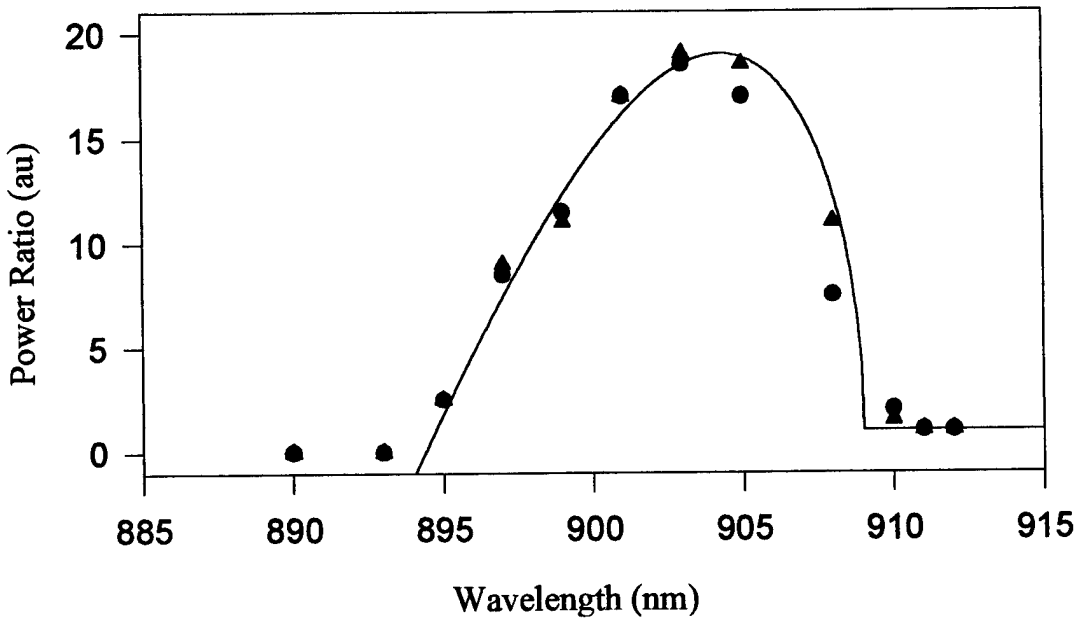

Figure 3.6 Experimentally measured gain response spectrum. Solid line represents theoretical curve.

3.3 MEASUREMENT OF OPTICAL NONLINEARITY

The third order optical nonlinearity was measured by using an interferometer to measure a phase shift induced onto an optical beam in one leg of the interferometer. In this experiment, a Mach-Zehnder interferometer was used, see Figure 3.7.

If the input beam is passed through an element with an intensity dependent index of refraction, $n = n_0 + n_2 I$, the beam will encounter an intensity dependent change in

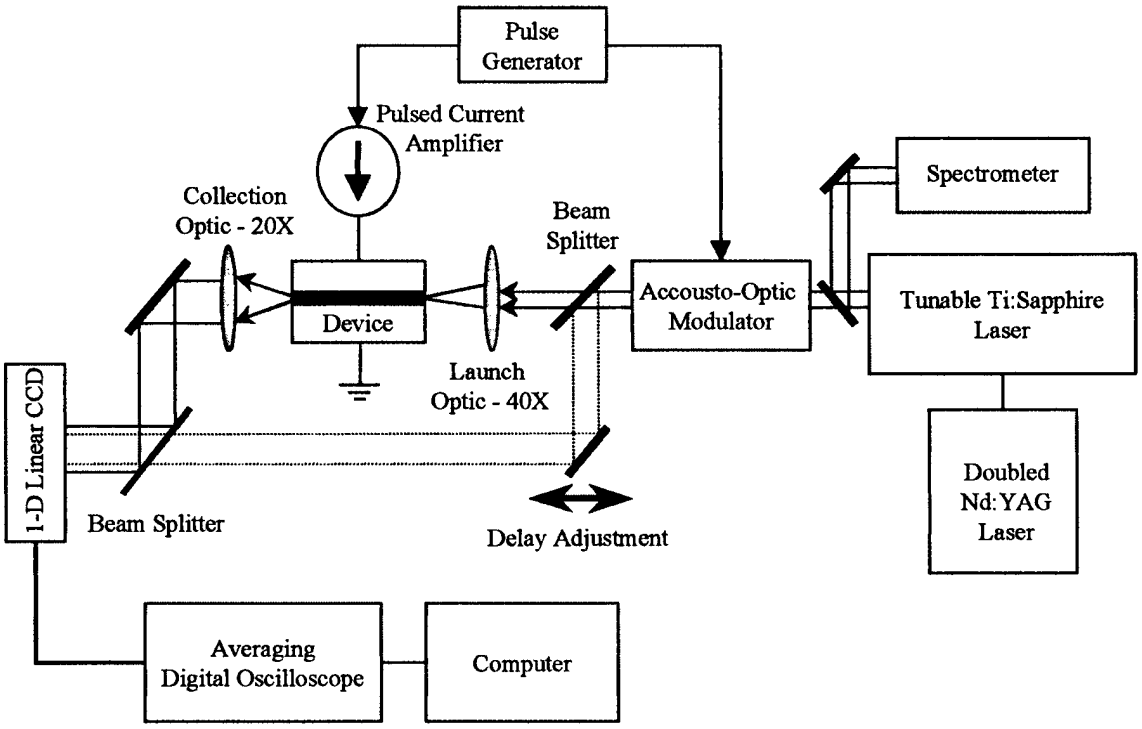

Figure 3.7 Mach-Zehnder Interferometer

optical phase, $\delta\phi = Lkn_2 I$, where L is the length of the device and k is the propagation constant. An interference pattern is established by offsetting the two arms of the interferometer slightly to create multiple peaks of spatial frequency $\lambda/tan(\theta)$, where θ is

the angle between the two beams recombining on the image plane. A one-dimensional CCD array captured the interference pattern and dumped the output to a digital oscilloscope with averaging capability. The averaging function was necessary to average out jitter in the interference pattern that is caused by air movements and mechanical vibrations in the room. The shift in the pattern was measured between two input optical powers of 12.5mW and 50mW at a variety of wavelengths. The input current to the device was pulsed using a 1.5 microsecond on to 48.5 microseconds off ratio to maintain consistency with the measurements of spatial solitons. The optical beam was also temporally shaped using an acousto-optic modulator to track the electrical modulation. The optical pulses were derived from a cw titanium sapphire laser pumped by a mode-locked, frequency doubled Nd:YAG laser. Each modulated optical pulse was one microsecond in duration and timed to pass through the amplifier ½ microsecond after electrical current started to inject into the amplifier. The delay allowed the amplifier to stabilize prior to the optical pulse arriving. Figure 3.8 shows the measured output from the interferometer. The maximum observable shift in the interference pattern was 3.5π. Using the phase shift equation, $\Delta\phi = kLn_2I_0$, this corresponds to a nonlinear coefficient of 5.7×10^{-10} cm^2/W and occurred at the peak of the gain spectrum. This corresponds with the normalized plasma and Kramers-Kronig theoretical fits shown also in Figure 3.8.

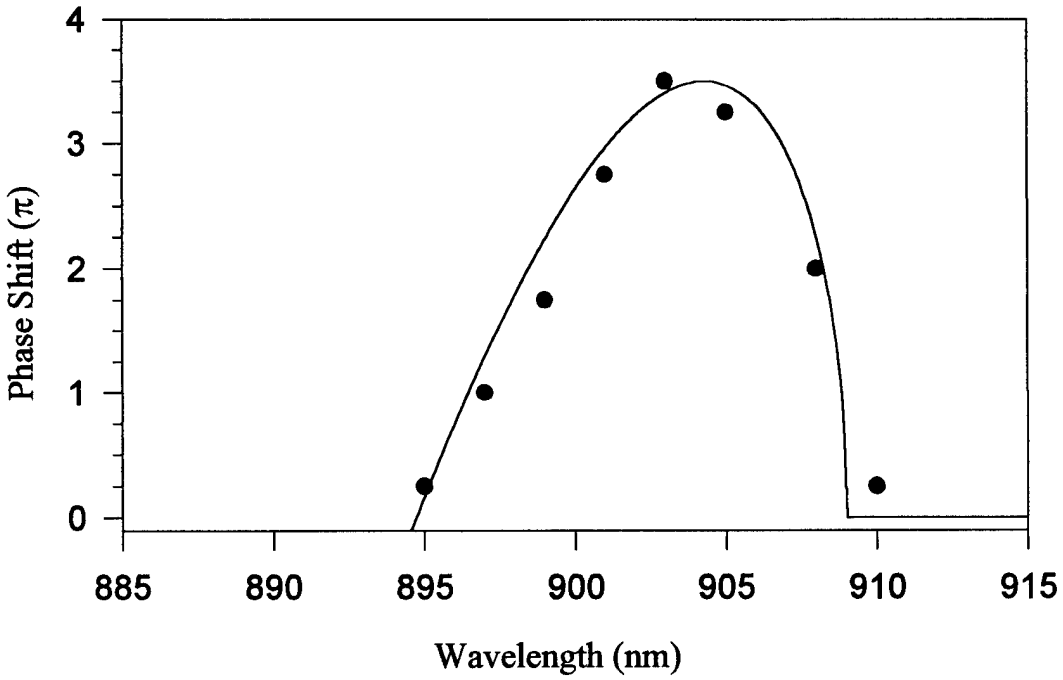

Figure 3.8 Mach-Zehnder phase shift measurements.

3.4 MEASUREMENT OF INDEX SHIFT WITH CARRIER INJECTION

Using the same setup used in the nonlinearity measurement, the phase shift induced by carrier injection was also measured. In this experiment, a constant optical power of 5mW was maintained at 904 nm, while changing the electrical injection into the waveguide. The results are shown in Figure 3.9. Using the linear relationship $\Delta n = n_c J$ where n_c is a constant relating the change in current concentration to the change in the index of refraction Δn, $n_c = -7.521 \text{x} 10^{-7} cm^3 / A$. This is used to predict the effect of the electro-optic steering mechanism used to steer solitons in devices considered later in this research.

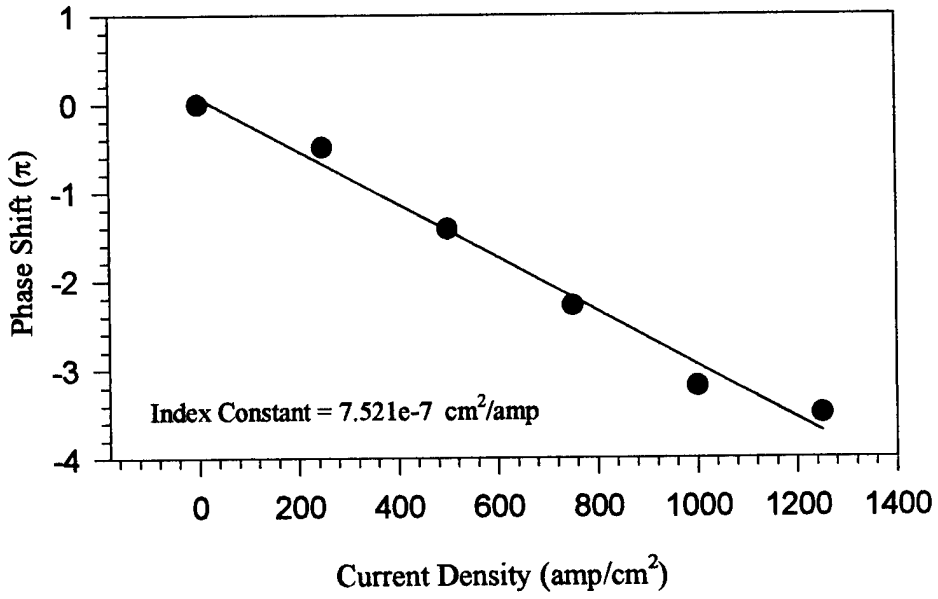

Figure 3.9 Device phase change with varying current. 4 um-wide waveguide, 1mm long measured at 904nm, Current injection 10-40ma.

3.5 CHARACTERIZATION OF THE OHMIC CONTACTS

Although not critical to the preliminary devices studied here, the quality of the electrical ohmic contact made to the p-side of the wafer is critical in the optimization of the device efficiency and in reducing resistive heating due to contact resistivity. To measure the resistivity to the contacts, a test pattern, called a Transmission Line Pattern (TLM), was fabricated onto the p-side of the wafer. The n-side contact was not analyzed as it was a large area metallization, in direct contact with the heat sink and separated from the devices by several hundred microns. The p side contacts, on the other hand, were

within 1 micron of the junction and were narrow contacts passing a large amount of current.

Resistance in the semiconductor can be modeled as a series of resistances. With an ohmic contact, the resistances are the resistance the contact forms with the surface, and the bulk resistance of the material between the contact pads. The resistance between two closely spaced pads where the distance between the pads is much less than the distance laterally along the interface, is $R = 2R_{contact} + d * R_{bulk}$, where $R_{contact}$ is the resistance between the contact and the material, d is the distance between the two contacts, and R_{bulk} is the resistivity of the material. The contact resistance can be found by measuring the resistance between two pads at different spacings and fitting the results to the equation.

The TLM pattern consists of a row of 50x300 micron ohmic pads separated by increasing distances of 2.5, 10, 20, and 40 microns. A diagram of this pattern is shown in Figure 3.10. Note that the distance between the pads is much less than the distance from side to side. Resistivity measurements are made between adjacent pads.

The specific contact resistivity can be calculated by assuming that the current passing between the two pads crowds through an area at the front portion of the each pad.[70,71] This greatly reduces the effective area the current passes through, and minimizes the increase in resistance created by the current passing underneath the contact through the semiconductor. The distance into the pad is referred to as the transfer length; denoted here by L_t. The width of the area is the width of the pad, *w*. The x axis intercept of the distance versus resistance plot denotes twice the value of this transfer length. As the transfer length is small compared to the length of the contact, the short surface resistivity

under the pad is ignored. Therefore, the specific contact resistivity in (Ω cm^2) of the pad becomes

$$\rho_c = R_{contact} L_t w \tag{3.6}$$

Additional formulas and measurement techniques exist to pinpoint exact specific contact resistances[72,73] however, the measurement and analysis preformed here are sufficient to judge the relative health of the p type contact.

A typical plot of these results is shown in Figure 3.11. The pad resistivity is ½ of the y intercept of the plot seen here as 0.4 Ω. The transfer length is ½ of the x-axis intercept or 5 microns. Therefore, the pad resistivity is $6.0x10^{-6}\,\Omega \cdot cm^2$. Using this equation 3.6, a 4-micron pad, 1-mm long will have a total resistance of 0.15 Ω.

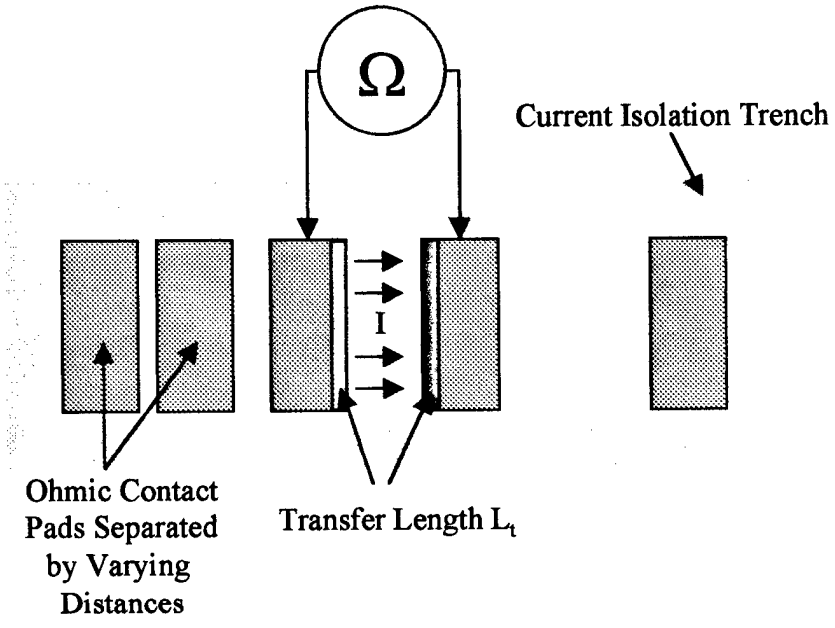

Figure 3.10 Diagram of a TLM pattern. Pad separation is 2.5, 5, 10, 20, and 40 microns.

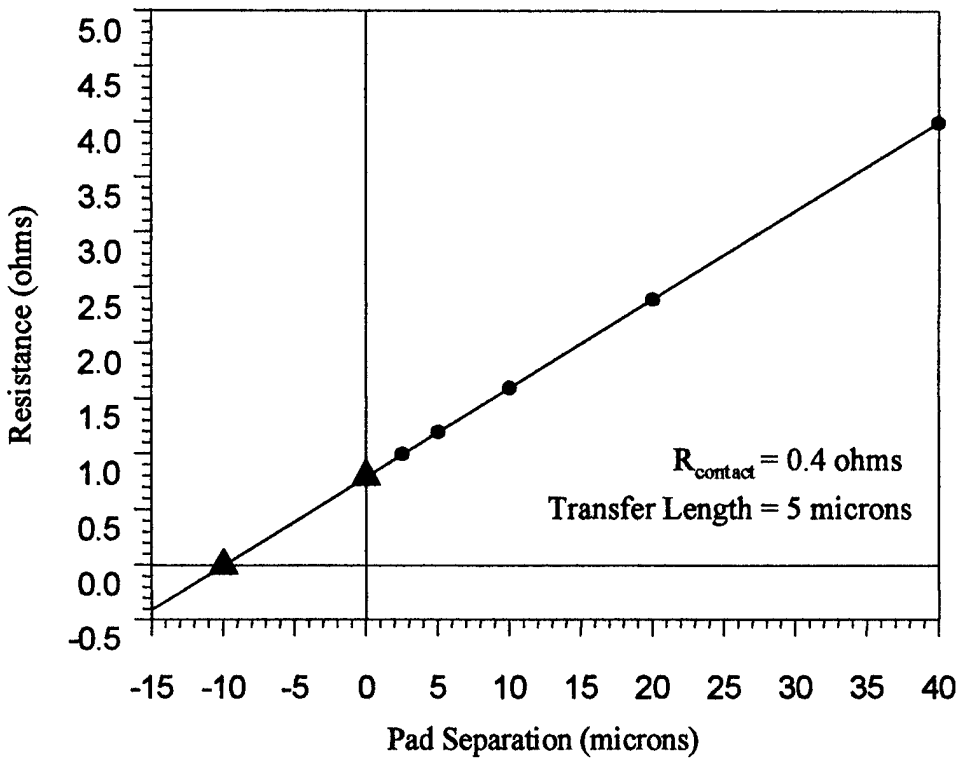

Figure 3.11 TLM p type pad resistivity measurements

CHAPTER 4: SOLITON MEASUREMENT

The theory and measurements outlined in Chapters 1 and 3, indicate that a nonlinearity strong enough to produce viable solitons exists in GaAs semiconductor optical amplifiers. This chapter describes the device that was fabricated along with the measurements that demonstrate and characterize these solitary waves.

4.1 DEVICE

The active semiconductor gain medium used in this work was a double heterostructure $Al_{0.2}Ga_{0.8}As$/GaAs p-i-n structure grown on a (100) oriented n-doped GaAs substrate, with an intermediate 3000Å thick n-doped GaAs buffer layer. The lower n-doped AlGaAs layer was 1.5 μm thick, the intrinsic GaAs active region was 0.2 μm thick, and the p-doped upper cladding layer was 1.0 μm thick. A 1000Å p-doped contact layer covered the upper clad layer. The devices, shown in Figure 4.1, were formed by depositing a 60 μm wide Au/Zn/Au contact over the wafer and then etching 5 μm wide, 2000 Å deep current isolation trenches to either side of the gold contact. The sample was then thinned down to 200 μm and a Ni/Ge/Au n-type ohmic contact was applied to the backside. After annealing at 420°C for 120 sec to form the n and p ohmic contacts, the

device was cleaved to 650 μm and mounted on a copper stud. To frustrate lasing in the active device, the contact stripes were angled at 4° from the primary cleavage plain and then aligned to the corresponding 15° launch angle. Anti-reflection coatings were not applied. The size of the semiconductor amplifier's active area, the lack of facet antireflection/protective coatings, and the amount of current required to drive the device

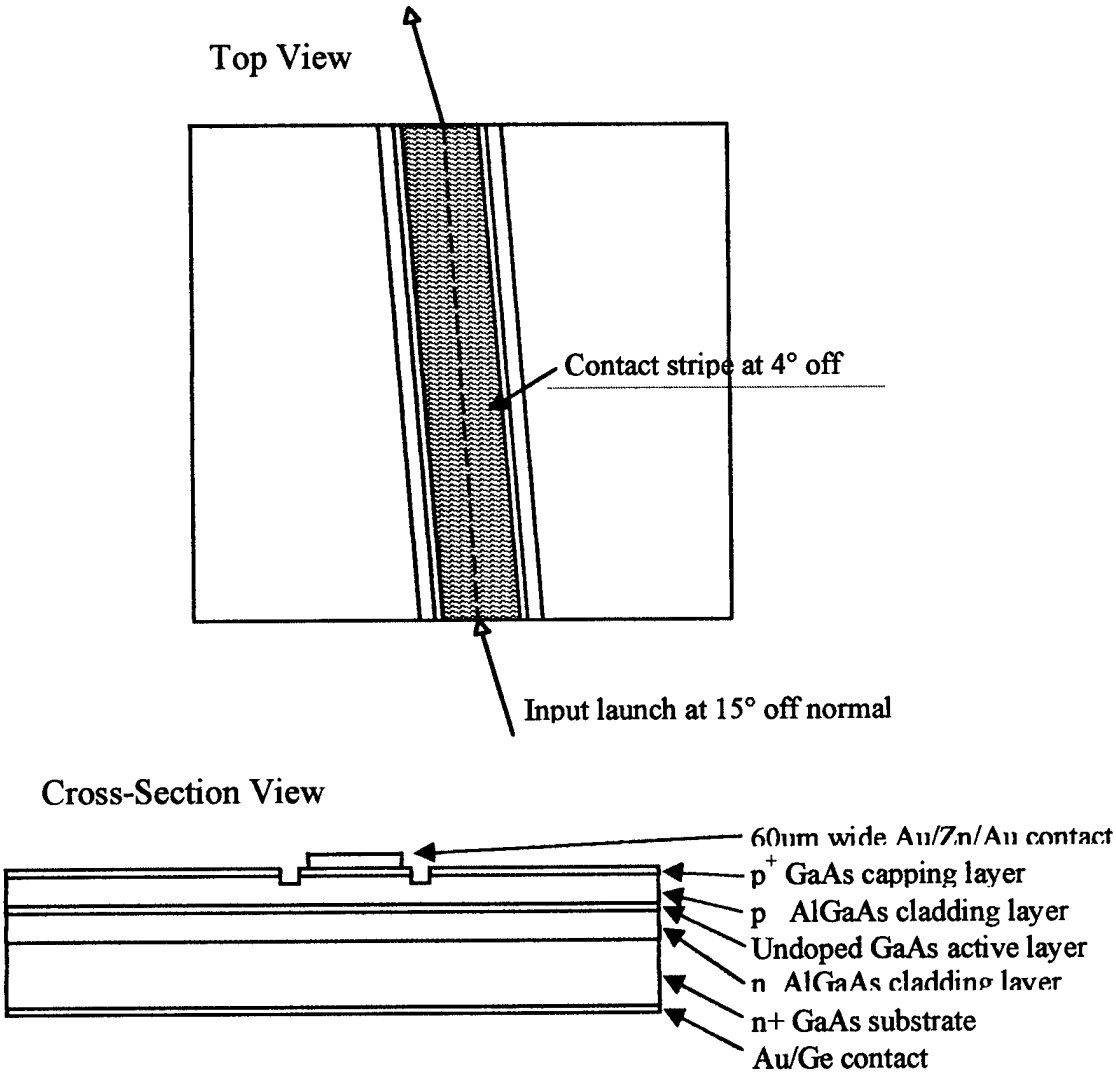

Figure 4.1 Diagram of soliton device

into inversion mandated the use of a pulsed current driver. The current pulses were 1.5 μs in duration, had a repetition frequency of 20 kHz (50 μs cycle) and had a peak amplitude of 750 mA, unless otherwise stated in the experiment. The device was found to lase at an instantaneous current of 1.2 Amps.

4.2 EXPERIMENTAL SET-UP

The experimental setup that was used to measure spatial solitons is shown in Figure 4.2. This experiment used the same tunable Lexel Model 480-D-1X, Ti-sapphire light source pumped by a Coherent Antares Model 76-S, frequency doubled, mode locked, Nd:YAG laser as the Mach-Zehnder experiment described in Chapter 3. As with the previous experiment, the beam was temporally shaped to 1 μs in duration using a Quantum Technology Model 304A acousto-optic modulator to match the 1.5 μs current pulses applied to drive the amplifier. This modulator provided 300-mW power at the peak of each pulse. Following a polarization filter and rotator, the beam diameter was then spatially reduced using a 2X-reducing telescope, so that it would fit within the launch objective lens. No attempt was made to adjust the spatial profile of the beam to match the input astigmatism of the waveguide. The beam was end-fire coupled using a 40X long working distance fiber launch objective, and the output facet of the amplifier was imaged onto a Watek Model 09 calibrated CCD camera using a 20X microscope objective. The output beam profiles were measured by frame grabbing a unity-gamma calibrated camera image of the amplifier output with a Snappy frame grabber and the

beam profiles were analyzed using Image Tool, a software downloaded from the University of Texas Health Science Center.

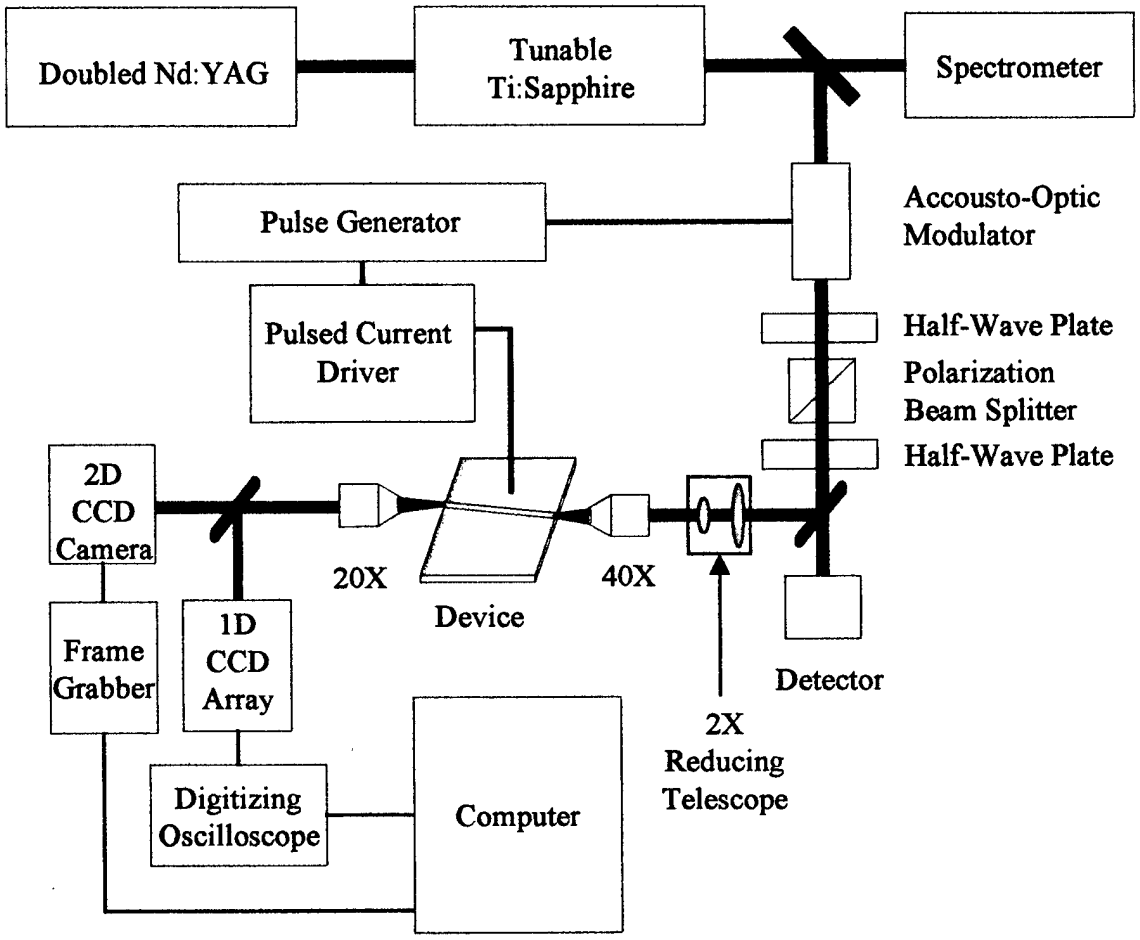

Figure 4.2 Soliton Measurement Experimental Setup

4.3 COUPLING AND PROPAGATION LOSSES

Coupling of a laser beam into a semiconductor slab waveguide using a single objective lens is invariably an inefficient process. Firstly, the uncoated facet of the high

refractive index semiconductor leads to large Fresnel's reflection losses. Secondly, focusing the beam from the Ti:sapphire laser to a spot size equivalent to the thickness of the active waveguide core (0.2μm) is impracticable. Furthermore, the asymmetric numerical aperture of a slab waveguide is another tough obstacle to overcome and indeed the optimum launch condition for a slab waveguide does not correspond to the ideal condition for launching a soliton waveguide. However, in order to measure the coupling efficiency, the waveguide propagation losses needs to be known. There are insurmountable obstacles that prevented us from determining the actual propagation losses. In particular, the propagation losses need to measured at either some specific injection current density or at a wavelength where the corresponding intrinsic band-to-band absorption losses are less severe. Although in a single mode waveguide, the propagation losses could have been measured by thermal scanning of the Fabry-Perot transmission resonances of the waveguide resonator cavity, these losses would not be meaningful for the slab waveguide. Consequently, the coupling losses due to mode mismatch were estimated by calculating the overlap integral of the waveguide mode with the focused laser beam spot size. The coupling losses due to Fresnel's reflection at the dielectric interface was also evaluated theolretically. Reflectivity Losses

Light was coupled into the soliton devices by end-fire coupling. This type of coupling suffers from losses induced by the reflectivity created at the interface of air and the semiconductor facet. The reflectivity losses can be calculated by using the linear index of refraction of the GaAs and the angle of coupling in Fresnel's equations, equations (4.1) and (4.2). Although the input beam propagates in the TE mode inside the

slab waveguide, the polarization is TM to the physical interface, which is positioned at 15°. The power transmittance at this interface is found using the Fresnel's equation for dielectric interfaces,

$$T = |\tau_\pi|^2 \frac{n_{GaAs} \cos(\theta_{GaAs})}{n_{air} \cos(\theta_{air})} \tag{4.1}$$

and the transmission coefficient, τ, is found using the equation

$$\tau_\pi = \frac{2 n_{air} \cos(\theta_{air})}{n_{GaAs} \cos(\theta_{air}) + n_{air} \cos(\theta_{GaAs})} \tag{4.2}$$

using n_{GaAs}=3.59, and the incident and transmitted angles of 15° and 4° respectively, the power transmittance is T=69.4%. Note that the Brewster's angle would be 74.4°.

In addition to reflection losses, the mismatch between the mode created by the launching objective and the waveguide mode reduces the energy coupled into the waveguide. The loss is particularly bad in the vertical direction where the size of the waveguide is only 0.2 microns, while the size of the beam at the facet is 6.0 microns full width half maximum. The loss in the horizontal direction is less critical as the waveguide is a slab and is able to accept any width of input beam. The coupling efficiency between the input mode and the waveguide mode, Γ, is expressed as the integrated overlap of the guided mode and the launched beam mode

$$\Gamma_{m,n} = \frac{\left| \int_{-\infty}^{\infty} \int_{-\infty}^{\infty} u_{m,n}(x,y) E(x,y) dx dy \right|^2}{\int_{-\infty}^{\infty} \int_{-\infty}^{\infty} |E(x,y)|^2 dx dy} \tag{4.3}$$

$u_{m,n}$ are the normalized modal shape functions (x and y) of the waveguide and $E(x,y)$ is the total field of the input beam. Assuming that the input beam is Gaussian with a FWHM of 6 microns, the coupling efficiency to a slab waveguide mode in a 0.2-micron waveguide is 9.18%. The coupling between a 6 micron FWHM Gaussian input beam and a 6-micron FWHM $sech^2$ beam is 93%. The resulting total coupling becomes $\Gamma = 0.93 * 0.0918 * 0.694 = 0.059$ or 5.925%. Other effects such as aberrations, dust, and noise will decrease this number. As such, 5.0% coupling efficiency is used throughout the rest of these calculations.

4.4 BEAM PROFILES THROUGHOUT SYSTEM

In order to characterize the magnitude of a soliton using the soliton stability equation (4.4), the magnitude and size of the launched beam must be determined.

$$Pa = \frac{2w}{n_0 n_2 k^2} \tag{4.4}$$

P is the power in the soliton beam, a is the waist of the soliton, w is the waist of the confined mode in the slab waveguide, n_0 and n_2 are the linear and third order nonlinear indices of refraction, and k is the propagation constant.

Beam powers were measured using a Newport Model 835 calibrated power meter, and the beam size was measured using a Watek Model 09 CCD camera to image the beam, and a Sensor Physics Laser Test LS-4W beam profiler to analyze the captured images. Calibration measurements confirmed that the Watek camera's gamma correction factor was 0.45, and the gamma correction was accounted for in the program. Beam

waist positions and size were determined by measuring beam shape at several points and fitting the waist to the Gaussian propagation equation

$$w = w_0 \sqrt{\left(\frac{(z - z_0)\lambda}{w_0^2} \right)^2 + 1} \tag{4.5}$$

where w_0 is the beam waist, z is the distance from the waist, z_0 is the position of the waist, and λ is the wavelength of the radiation. The familiar Rayleigh range is given in equation (4.5) by $Z_r = \frac{w_0^2}{\lambda}$. The beam waist equation (4.5) describes the propagation of a perfect Gaussian beam; deviations in the fit to this equation are expected as the beam emitted from the Ti:sapphire laser is close to, but not perfectly Gaussian. Of prime importance is the waist of the beam at the input to the device. Figure 4.3 shows measurements taken to confirm a beam waist of 5.8 microns. The Gaussian profile of the beams measured by calibrated camera is shown in Figure 4.4. These beam profiles matched a $1/e^2$ Gaussian fit by 96% and 94% for the x and y axis respectfully.

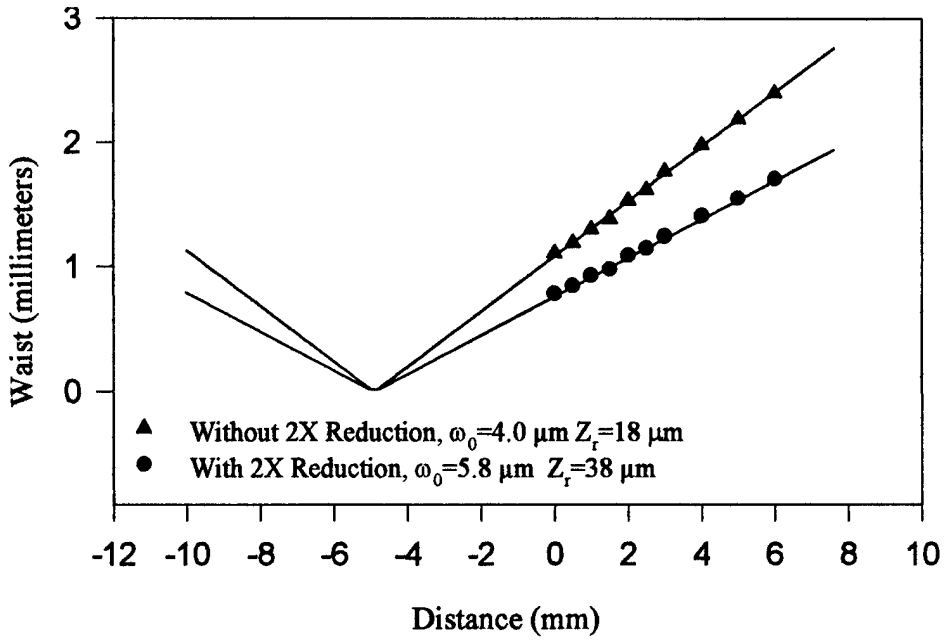

Figure 4.3 Profile of launched beams. ω_0 is the beam waist, Zr is the Rayleigh range.

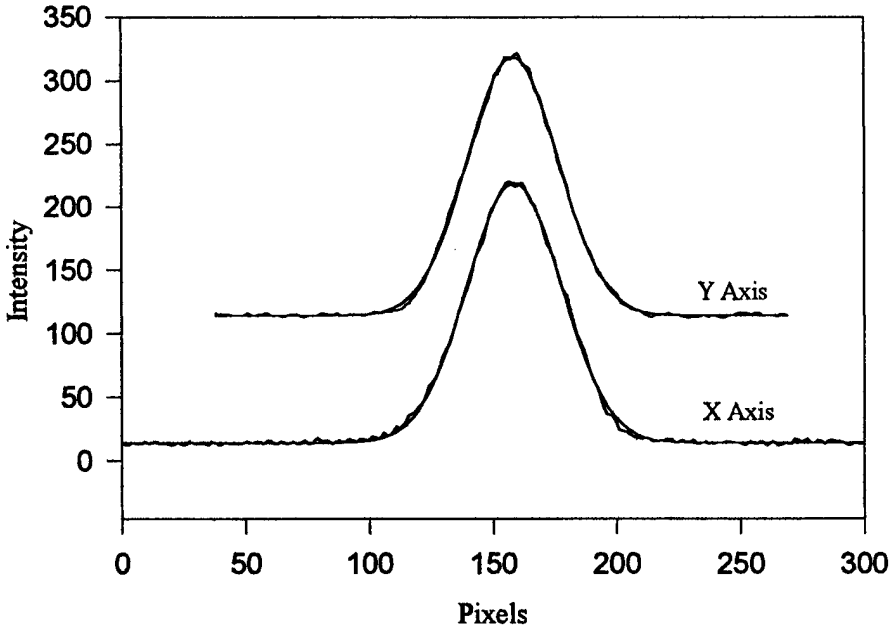

Figure 4.4 Intensity profile of beam in the x and y directions. Gaussian fit is shown.

4.5 SOLITARY WAVE FORMATION

The solution of the nonlinear Schroedinger wave equation (NSWE) states that the spatial transverse envelope of the soliton is $sech^2$. The input beam, however, is Gaussian. Thus, the beam must transform from a Gaussian profile to the $sech^2$ profile along the length of the device. The nonlinearity that leads to the formation of the soliton within the device assists in the transformation, as one of the properties of solitons is their ability to form in the presence of noise. Energy not conforming to the soliton mode is not contained in the solitary wave and diffracts away from the soliton. Conducting soliton formation measurements along the device would not be feasible, however, using a simulation (beam propagation code, appendix C), the solitary wave formation can be modeled. Figure 4.5 shows a graphical representation of the evolution of a Gaussian beam with the same waist as that launched in the experiments as it propagated through the sample.

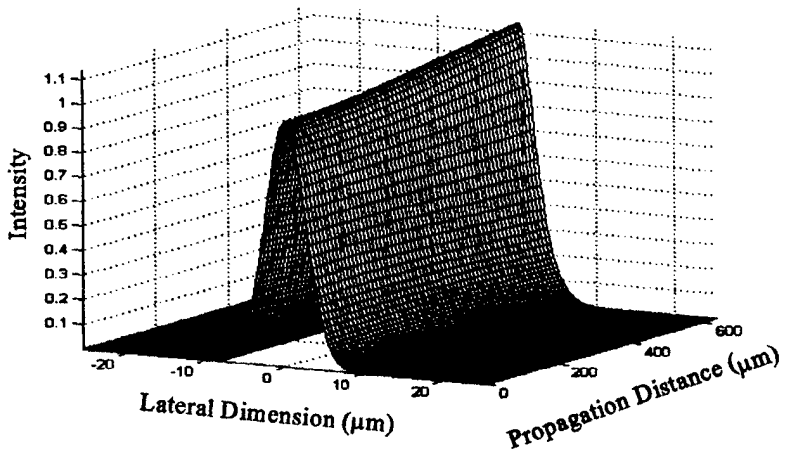

Figure 4.5 BPM Simulation of a Gaussian beam launched into a nonlinear optical slab waveguide.

In the experiment, 904-nm wavelength light was launched into the device with a focused beam waist of six microns. The measured input intensity was 1.1 MW/cm^2 in this experiment and the propagation distance was 650 microns. 18mW of instantaneous output power was measured coming out of the device after subtracting the spontaneous emission the device produced without any optical input. Figure 4.6 shows an actual measured output of the device along with the theoretical prediction made by the BPM. Using the BPM code to iteratively fit the peak, the nonlinear n_2 coefficient was $n_2=8.83x10^{-10}$ cm^2/W. From the measured soliton beam waist, of 6 microns, and the input optical intensity of $1.1MW/cm^2$ and taking into account the coupling losses described above, the nonlinear coefficient n_2, was calculated to be $5.6x10^{-10}$ cm^2/W.

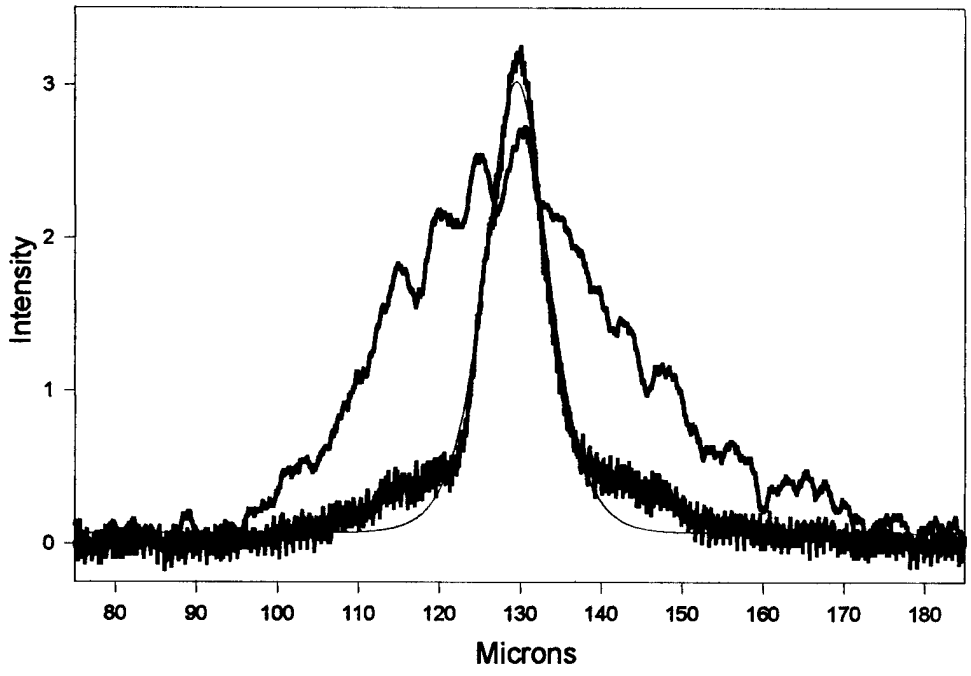

Figure 4.6 Output beam profile of a slab-guided soliton. Solid line is theoretical fit to the expected beam profile generated using a beam propagation code. The wide function is the beam output without the nonlinearity.

4.5.1 NONLINEARITY VS. WAVELENGTH

The soliton waist was measured at a variety of wavelengths while keeping the device electrical current and input optical intensity constant. These optical and electrical parameters were carefully selected such that the solitons that were formed contained the largest percentage of the launched energy at the lowest input optical intensity. This was necessary in order to produce a solid soliton, but not to saturate the nonlinearity. According to the theory developed in Chapter 1, the nonlinearity should be directly proportional to the gain measured in the material. This hypothesis is confirmed by the plot of Figure 4.7, which shows the normalized nonlinearity as a function of the input wavelength. A normalized shape of the measured gain curve is plotted on the same axes for comparison.

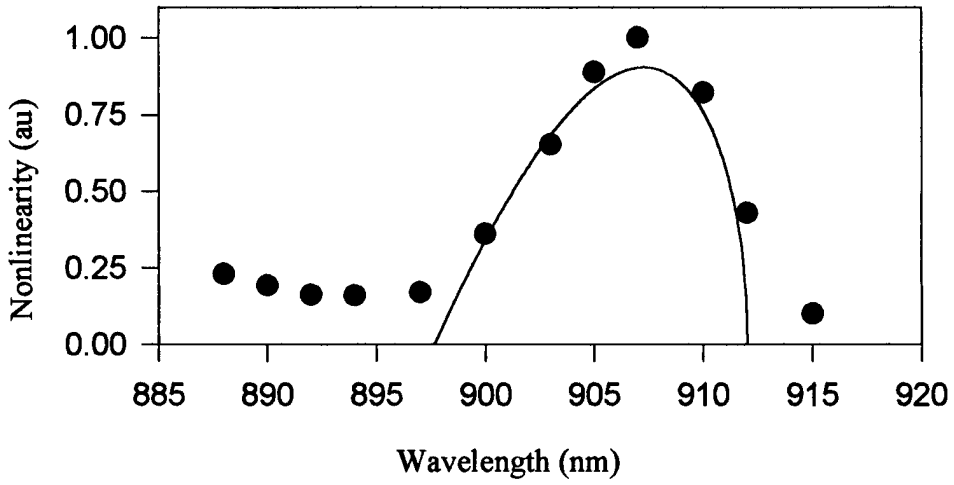

Figure 4.7 Nonlinearity versus wavelength. Nonlinearity found by taking the inverse of the product of the beam power and the beam width. Normalized gain curve displayed as the solid line.

4.5.2 NONLINEARITY VS. CURRENT

The same measurement as the previous section was performed, but in this experiment the current was varied while keeping the intensity and wavelength fixed. The theoretical calculation in this situation as shown previously predicts that the nonlinearity should follow the gain curve. The peak of the gain curve, however, shifts with changing current. These effects, taken together, may result in the nonlinearity remaining relatively constant. This effect was seen in beam waist measurements taken against increased current, shown in Figure 4.8. The inset of Figure 4.8 shows the dependence of the output power and beam waist on the injection current. At very high currents, the beam waist remained constant, while the output power continued to increase. At this point, side lobes began to form around the main lobe possibly signaling the onset of higher order self-guided modes.[74] The falloff of the nonlinearity results from energy transferring into the side lobes of the output beam.

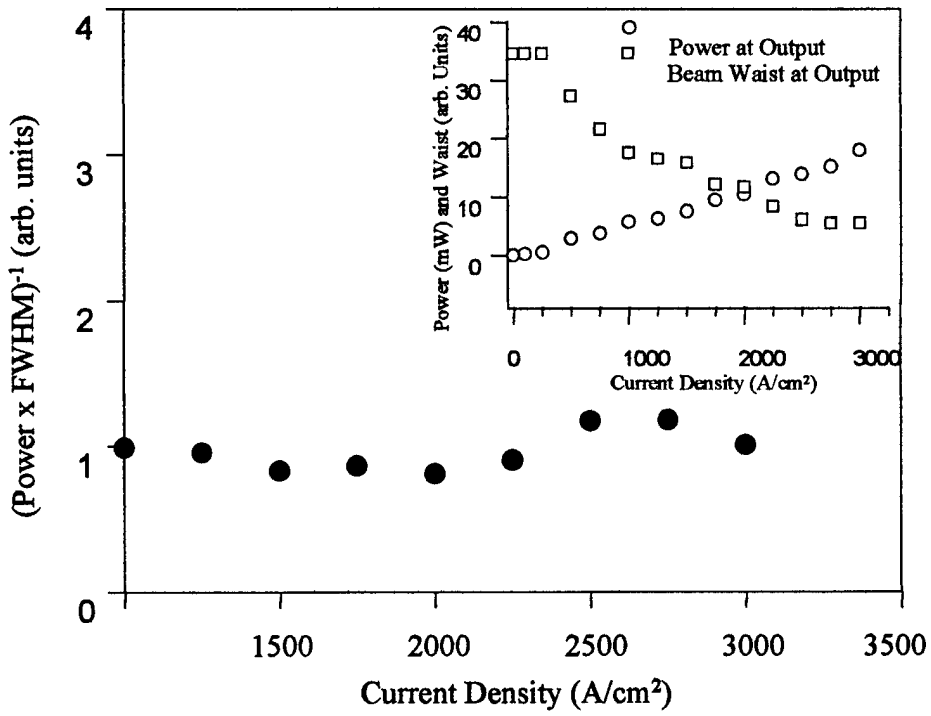

Figure 4.8 Nonlinearity versus Current Density. Inset shows the relationship between beam waist and output power. At high currents, the beam waist no longer shrinks, however, side lobes begin to form around the main lobe.

4.5.3 NONLINEARITY VS INTENSITY

In the next series of measurements, the best soliton was formed using the lowest input optical intensity. The input optical intensity was then varied and the soliton waist was measured. Figure 4.9 depicts the measured soliton beam waists versus input intensity. In theory, the gain, and thus the nonlinearity must eventually saturate.

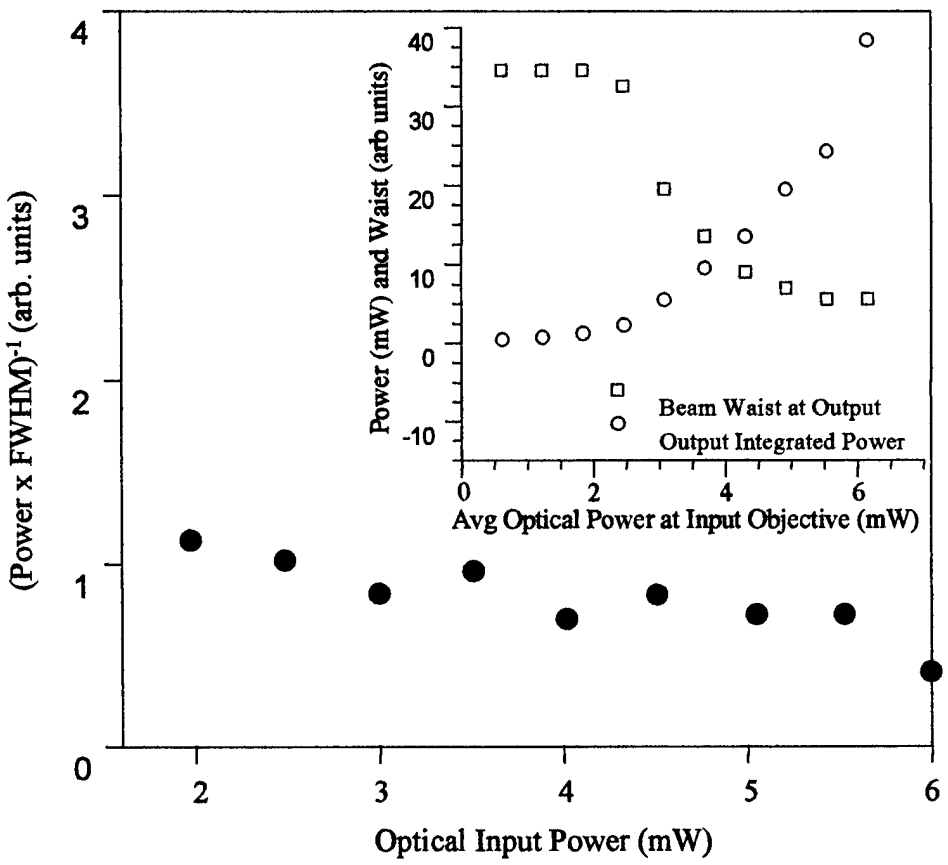

Figure 4.9 Nonlinearity versus input optical power. Inset shows how beam waist and power change with input optical power.

This measurement, although producing a small roll-off in the nonlinearity, may not give a precise measure of the saturation intensity. As the intensity was increased, a pedestal and side lobes began to form around the soliton. This pedestal may be excess energy not able to be contained within the soliton, or may be the onset of a higher order mode as suggested in other soliton experiments.[74] Although a second order soliton in a pure Kerr like material would not form 3 distinct peaks, the nonlinearity in this material is not entirely Kerr like.

4.5.4 NONLINEARITY VS. WAVELENGTH: PEAK INTENSITY

As a final confirmation of the nature of the nonlinearity, the peak of the soliton was measured versus wavelength. The power contained in the beam is proportional to the peak of the function, thus, the behavior of the peak provides insight into the spectral nature of the nonlinearity. Figure 4.10 displays the measured peak intensity of the soliton against the wavelength. As expected, the nonlinearity tracks the gain curve. The measured and normalized gain curve is overlaid for reference. As expected, the nonlinearity tracks the gain curve. As noted in the experiments above, the final width of the output will only reduce to the width of the diffracted mode, or approximately 34 microns FWHM. This produces the non-zero intensities to the lower energy side of the gain peak. To the high-energy side, no signal appears due to absorption in the semiconductor.

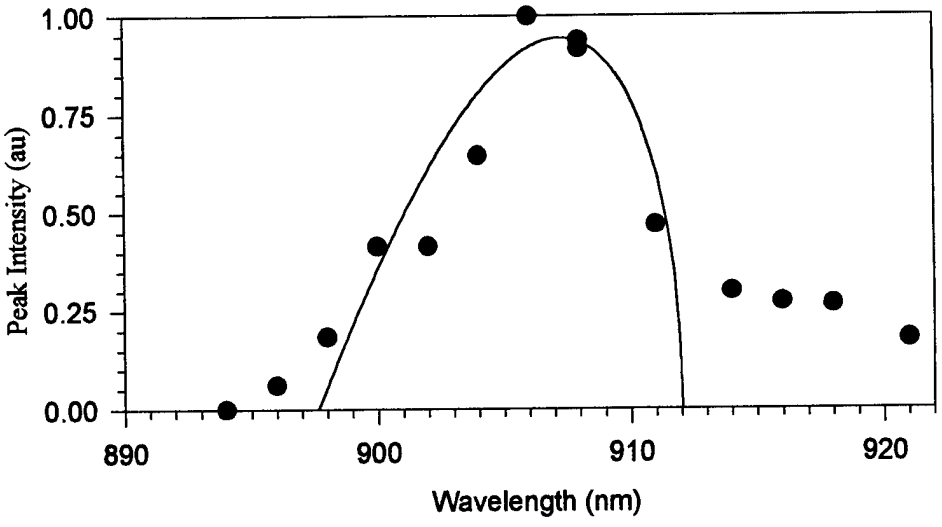

Figure 4.10 Measurement of absolution signal peak with varying wavelength. Nonlinearity continues to follow the rough gain outline.

CHAPTER 5: GUIDING OF OPTICAL BEAM BY SOLITON WAVEGUIDE

The solitons studied in the previous chapter have demonstrated the ability to form waveguides capable of guiding other beams within the index of refraction wake of the soliton. The ability to guide unrelated beams leads to the formation of devices capable of switching information from one input to a variety of outputs in a single stage if the soliton can be steered electro-optically.

5.1 CROSS POLARIZED SIGNAL BEAM

If coherent beams are employed then the addition of the second beam coincident upon the soliton beam requires cross phase modulation to be taken into account. The coupled equations governing the interaction are

$$\frac{dE_\sigma}{dz} = \frac{i}{2k}\frac{d^2E_\sigma}{d^2x^2} + \frac{g_\sigma}{2}E_\sigma + ik_0 n_{2,\sigma}\left(|E_\sigma|^2 E_\sigma + A_\sigma |E_\pi|^2 E_\sigma\right)$$

$$\frac{dE_\pi}{dz} = \frac{i}{2k}\frac{d^2E_\pi}{d^2x^2} + \frac{g_\pi}{2}E_\pi + ik_0 n_{2,\pi}\left(|E_\pi|^2 E_\pi + A_\pi |E_\sigma|^2 E_\pi\right) \qquad (5.1)$$

In these coupled equations, E_σ represents the TE polarized field creating the soliton, E_π represents the weak TM signal beam guided by the first beam. k represents the propagation wave vector of the two beams. The n_2 terms are the nonlinear coefficients for the two polarization states (self phase modulation), and the A terms are the ratio of the cross phase to self phase modulations. As the cross polarized signal beam is well beyond the range of the gain creating the nonlinearity, the $n_{2,\pi}$ and g_π terms are expected to be very small, and the A_π term large. Additionally, the signal beam is weak compared to the soliton beam, thus the signal beam is not expected to contribute significantly to the phase modulation of the soliton beam. Finally, because the index profile created by the soliton results from the depletion of unpolarized carriers in the conduction band, the change in the index of refraction for the cross polarization state is anticipated to be nearly equal to that created by the soliton. The index will be ratioed by a factor, B, due to the dispersive nature of the index shift with wavelength as discussed in section 5.2. Thus, as a first order hypothesis, the coupled mode equations reduce to

$$\frac{dE_\sigma}{dz} = \frac{i}{2k_\sigma}\frac{d^2E_\sigma}{d^2x^2} + \frac{g_\sigma}{2}E_\sigma + ik_0 n_{2,\sigma}\left|E_\sigma\right|^2 E_\sigma$$

$$\frac{dE_\pi}{dz} = \frac{i}{2k_\pi}\frac{d^2E_\pi}{d^2x^2} + ik_0 B n_{2,\sigma}\left|E_\sigma\right|^2 E_\sigma \qquad (5.2)$$

5.2 REFRACTIVE INDEX PROFILE (K-K RELATIONSHIP) WITHIN SOLITON TRACK

The relationship between the localized index of refraction change and the solitary wave was developed in Chapter 1 and confirmed by measurements in Chapters 3 and 4. This index of refraction, however, was the self-action index, or the index that the photons creating the soliton see. Photons outside this spectral range encounter a different index of refraction. As shown in Chapter 1, the mechanisms creating the change in the index fall into two categories: contributions from a carrier plasma effect, and contributions from the shift in the absorption edge due to the gain depletion. In the first effect, the index contribution from the plasma effect is proportional to the wavelength squared, as long as the wavelength remains far from the resonance, as is the case at 960nm. The spectral dependence of the change in refractive index resulting from the shift in the absorption, however, is related by the Kramers-Kronig relationship, developed in appendix B, to the spectrum of the absorption change. The spectral relationship between the band edge shift and refractive index is given by

$$\Delta n(\omega) = -\int_{-\infty}^{\infty} \frac{\Delta\alpha(\omega')}{\omega - \omega'} \partial\omega' \tag{5.3}$$

where $\Delta\alpha(\omega)$ is the change in the absorption spectrum. This change is modeled by changing the carrier concentration in the semiconductor gain equation, and taking the difference between the gain curves. The Kramers-Krönig transform is applied to the

resulting gain difference yielding a spectral dependence of the change in the index of refraction. Combining these two effects yields the plot of the index of refraction curve shown in Figure 5.1. Using this spectrum and the fact that the maximum calculated change in the index across the soliton is $5x10^{-4}$, the maximum expected change in the index of refraction experienced at 960nm would be $2.49x10^{-4}$. The *sech*^{2} shape of the soliton defines the refractive index profile of the waveguide.

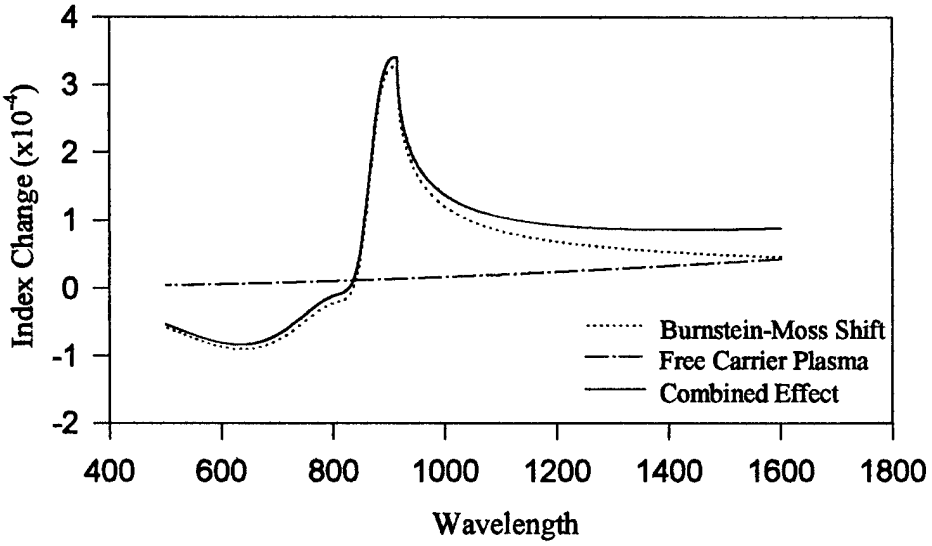

Figure 5.1 Change in refractive index due to carrier induced nonlinearities. Nonlinearity caused by a depletion of carriers at 904nm by an injected pump beam.

5.3 GRADED INDEX WAVEGUIDING (EXPECTED BEAM SHAPE)

Waveguide modes can be calculated analytically for only a very few specific set of waveguide geometries. A development for square profile waveguides is shown in

appendix C. In this method, trial functions are established for each of the zones of the waveguide, and boundary conditions are matched to provide a solution. This method can be extended to multiple square index systems using a computer to approximately solve the complete set of simultaneous equations. Using this method, the hyperbolic secant squared shaped index profile can be approximated by a series of small square index waveguides, shown in Figure 5.2, and boundary conditions set to solve for the mode profile of this system, overlay on Figure 5.3.

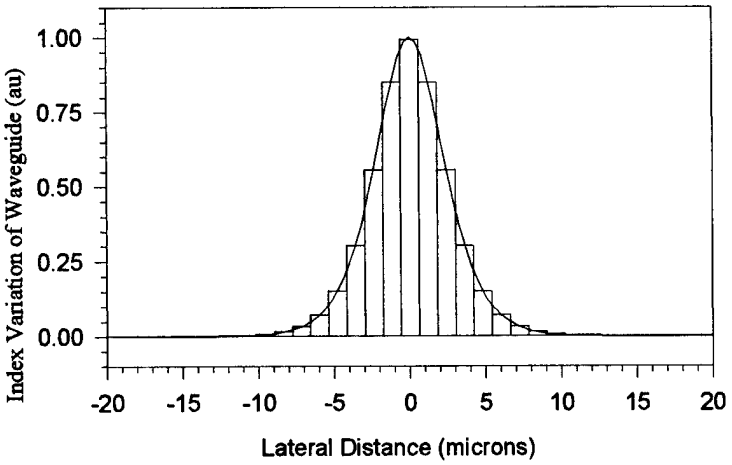

Figure 5.2 Square approximation used to solve mode profiles for a *sech*^{2} shaped waveguide. Solid line is the calculated field profile for this waveguide.

As a second confirmation of the mode profile of this waveguide, the Beam Propagation Method, appendix C, is used to simulate the index profile of the solitary wave waveguide. In this simulation, the hyperbolic secant squared shape is assumed fixed with an end-fire coupled signal wave guided down the length of the waveguide. This simulation and the resulting output beam shape are shown in Figure 5.3.

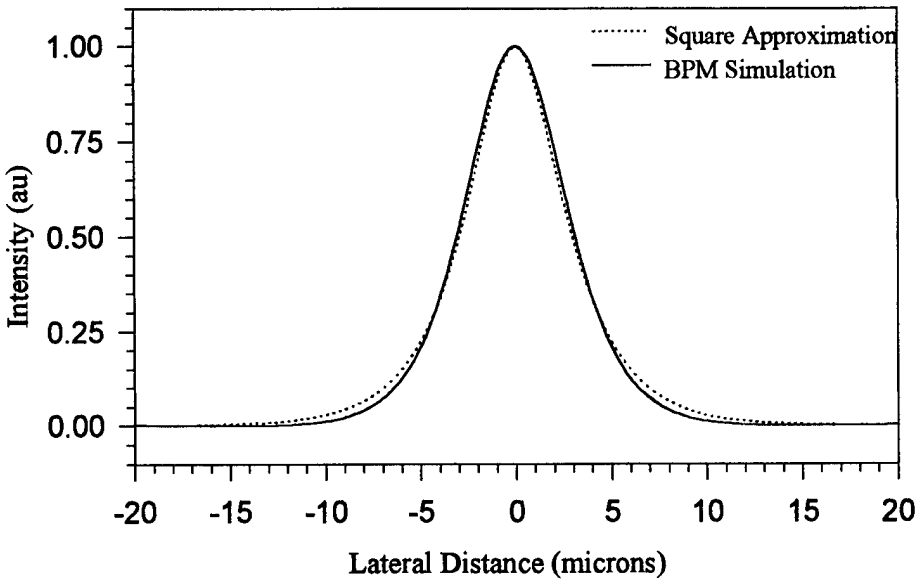

Figure 5.3 Calculation and Simulation of Intensity Profile in a 6 micron FWHM $sech^2$ graded index waveguide. BPM assumed a 6-micron FWHM Gaussian launch beam.

The peak magnitude of the guiding region was set at $5x10^{-4}$ above the base index of refraction. In both of these simulations, it is seen that the waveguide guides the beam, and the final confinement beam has a FWHM of 6 microns using a FWHM on the soliton beam of 6 microns.

The analysis shown above is accurate for a perfectly Gaussian, single mode input beam. The device used to create the signal beam, however, did not emit a single mode output. The laser used was an InGaAs wide stripe laser diode mounted and bonded in our laboratory. The beam profile was measured using a Watek 09 calibrated camera (Γ=0.45) and analyzed by a Spectra Physics LM-4W software package, Figure 5.4

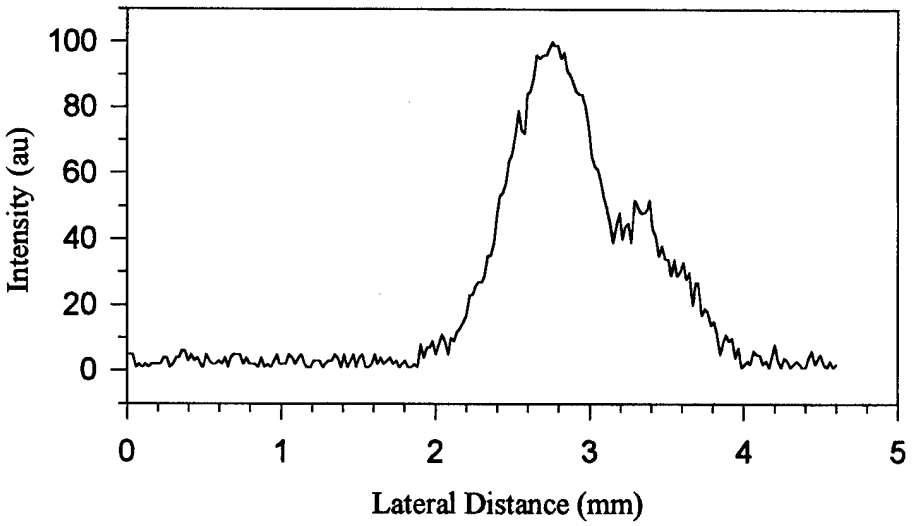

Figure 5.4 960nm input beam before 2x reduction telescope.

The waist size of this beam was set to match the waist position of the Ti:sapphire laser beam that was used to generate the soliton wave. The success of the match, however, is suspect as small adjustments that were required to align the launch optics, lens material dispersion, and material dispersion through the 15° launch angle make an exact match of this direct launch system impossible. Using this beam profile as the input to the soliton waveguide, a BPM analysis of the output of a soliton waveguide device is shown in Figure 5.5. As can be seen in Figure 5.4, the input beam irregularities provide a large array of possible launch conditions. The simulation results of Figure 5.5 were iteratively matched to the actual output by varying the input launch position and angle.

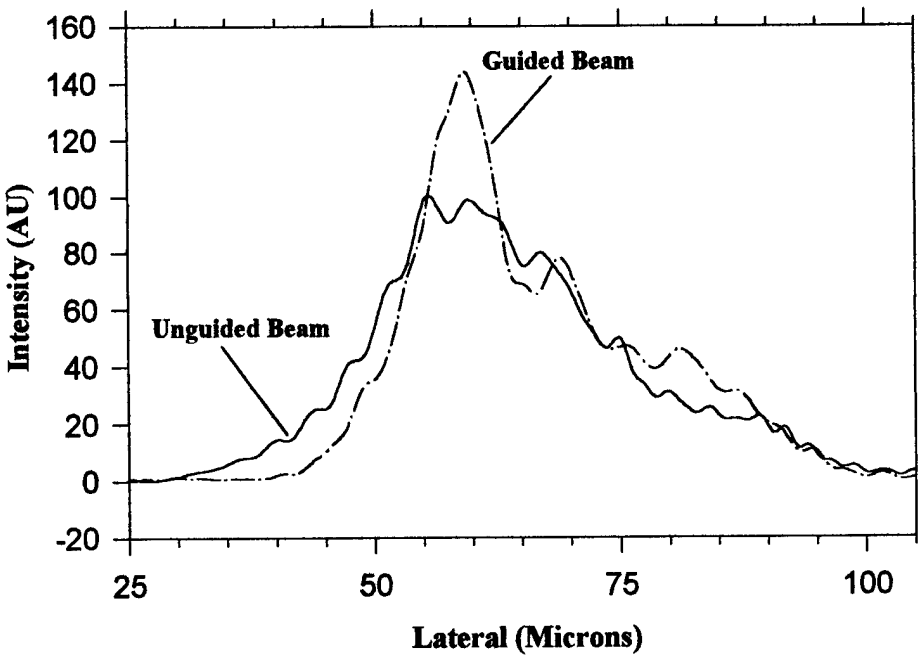

Figure 5.5 BPM simulation of the 960nm diode beam passing through the semiconductor optical amplifier with and without the guiding soliton beam.

5.4 BROAD AREA SOLITON DEVICE

The device characterized in Chapter 4 was used to demonstrate the ability of a soliton to guide a second unrelated beam. Remember that this device consisted of a 60-micron wide active region across a 650-micron long device. The stripe was angled at 4° to the cleaved facets to frustrate lasing. Due to the high refractive index (3.5) of GaAs, the non-orthogonal orientation of the stripe made it necessary to maintain a 15° launch angle external to the cavity. This launch angle contributed to difficulties in confining the signal beam within the soliton beam due to the fact that the index of refraction dispersion of the

semiconductor made the launch angles different. The use of a single mode injection waveguide is anticipated to alleviate this problem, however, a thorough investigation of this type of device shall be the subject of additional research.

5.4.1 EXPERIMENTAL SETUP

An experiment to demonstrate the ability of the solitary wave waveguide to carry signal information was conducted. The experiential setup that was used to measure spatial soliton beam guiding is shown in Figure 5.6.

This experiment used the same setup as the soliton measurement scheme used in Chapter 4 with the inclusion of an orthogonally polarized 960nm signal that is added at the polarization filter/beam splitter. A tunable Ti-sapphire laser served as the soliton creating light source. The Ti-sapphire laser was optically pumped using a frequency doubled, mode locked Nd:YAG laser. As with the previous experiment used to measure the soliton characteristics shown in Chapter 4, the beam was temporally shaped to 1 μs in duration using an acousto-optic modulator to match the 1.5 μs current pulses applied to drive the amplifier. This arrangement provided 300-mW power at the peak of each pulse. The beam diameter was then spatially reduced using a 2X-reducing telescope, so that it would fit within the clear aperture of the launch objective lens.

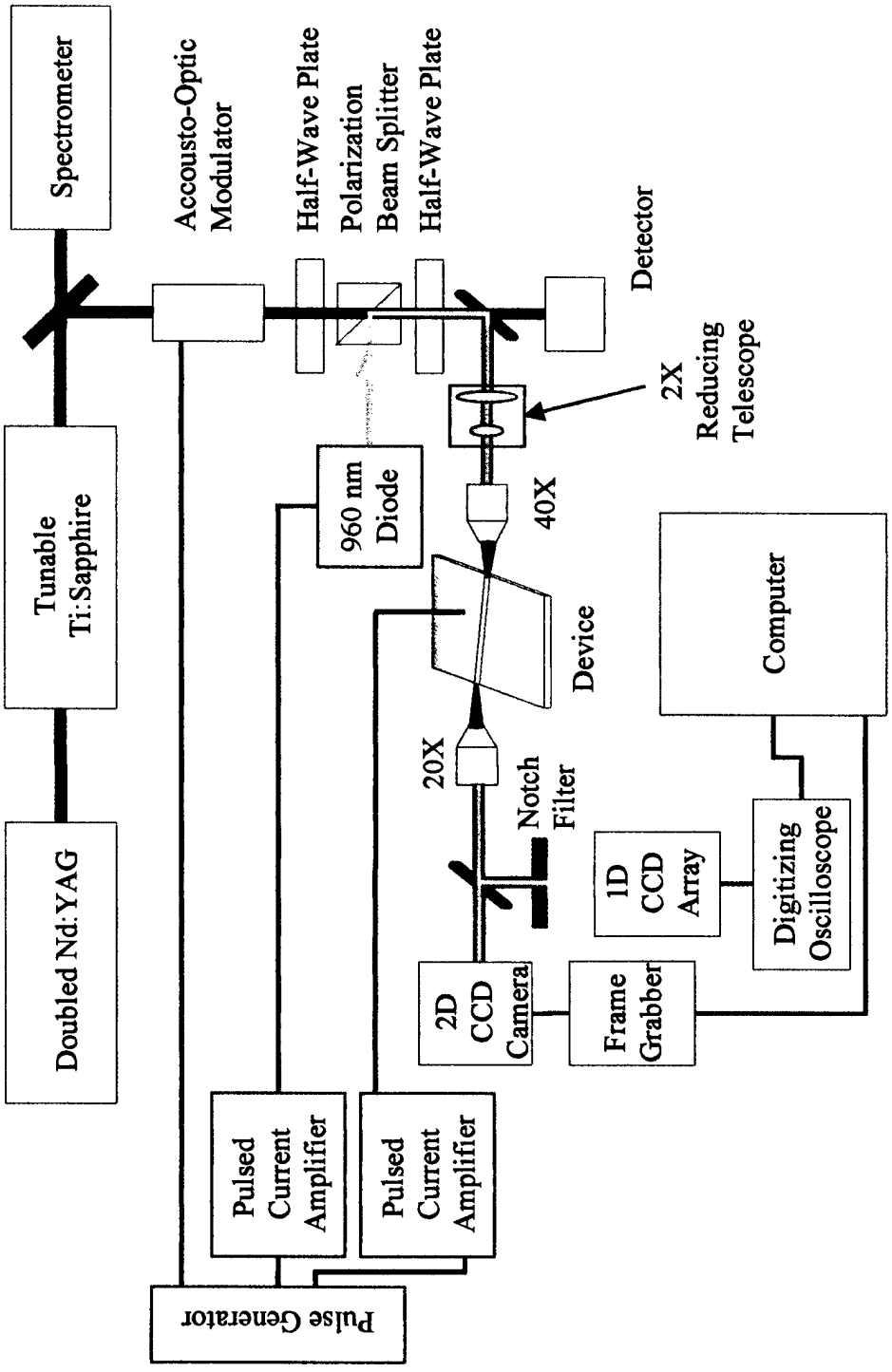

Figure 5.6 Experimental Setup for Soliton Guiding

This beam was end-fire coupled into the wide stripe semiconductor optical amplifier using a 40X long working distance fiber launch objective, and the output facet of the amplifier was imaged onto a calibrated CCD camera using a 20X microscope objective. To demonstrate self-guiding, a second laser beam, 62 nm longer in wavelength than the soliton writing beam, was added to the first beam using a polarization beam splitter. This second laser was a partially collimated, InGaAs multimode, wide-stripe laser, operating at 960nm. At the output, the 960nm guided beam was imaged independently from the 904nm soliton forming beam using a narrow bandpass interference filter. The beam output profiles were measured by frame grabbing a calibrated camera image of the semiconductor amplifier output and plotting the intensity distribution along the active region of the amplifier.

5.4.2 BEAM GUIDING MEASUREMENTS

Figure 5.7 displays beam profile plots of the best confined output of this device revealing the region where the soliton waveguide contained the 960nm signal beam. Nearly 3dB increase in signal strength is obtained in the region corresponding to the peak of the soliton profile. The input signal beam was highly multimode contributing to the lack of confinement in the output of the device. This type of poor collection is predicted in the BPM simulation shown in Figure 5.5. In Figure 5.7, the dotted line represents the theoretical shape of the output mode of the signal beam if a perfect launch beam was used. It is observed that the shape of the theoretical curve matches the section of the

output corresponding to the area guided by the soliton beam. The guiding soliton generated in this experiment had a FWHM waist of 8 microns.

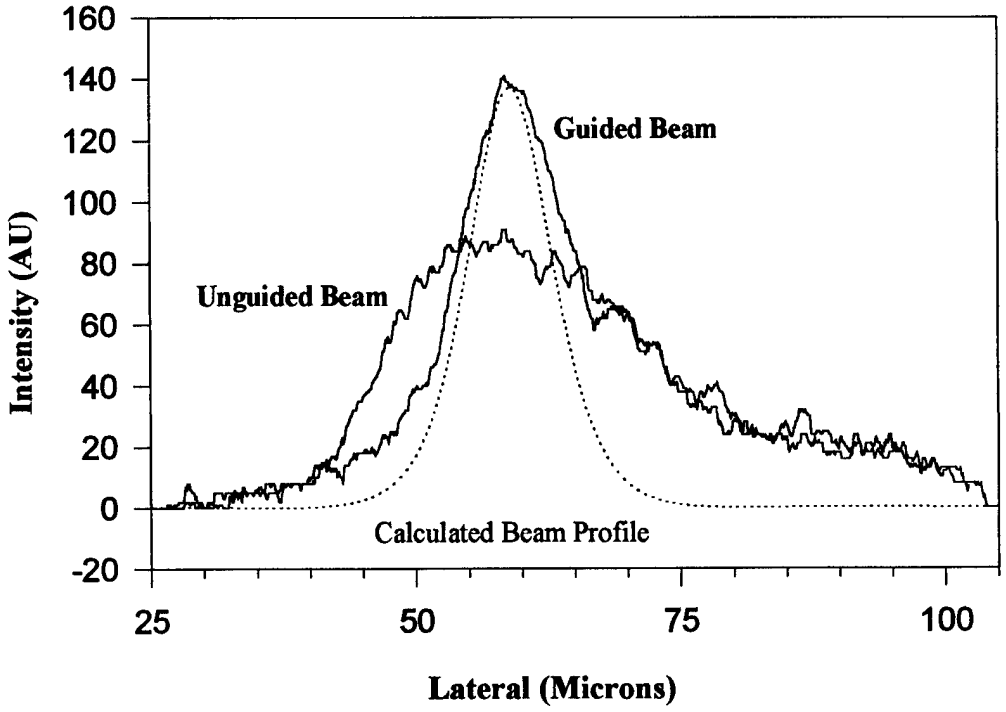

Figure 5.7 Soliton Guiding showing theoretical shape of the guided beam.

5.4.3 BEAM TRAPPING MEASUREMENTS

For optimum beam guiding, the soliton beam and signal beam must be spatially overlapped at the input to the device. An analog to this would be the alignment of the signal beam into a single mode waveguide. As with a fixed waveguide, the soliton will guide the portions of the input beam that leak into the soliton waveguide. This can be

viewed as the overlap of that portion of the signal beam's wave vectors with the propagation modes of the soliton waveguide. This is also referred to as beam trapping.

To measure the angular acceptance of the soliton trapping, the experimental setup shown in Figure 5.6 was used. To maintain coupling at various angles, the soliton and signal beams should overlap exactly at the input to the device. Offsetting the input angle of the signal beam from a point 2 meters from the launch objective approximated a collinear input to the launch objective. The percentage of power guided by the soliton beam was calculated using a beam propagation code with the actual measured signal beam at incremental angles as the input.

The measured amounts of energy at various input angles contained in the guided signal beam, along with a theoretical simulation, are graphed in Figure 5.8. Deviations from the shape of the curve are the result of the misalignment between soliton and signal when the signal beam was deviated, and also from the aberrations caused by the deviation of the signal beam.

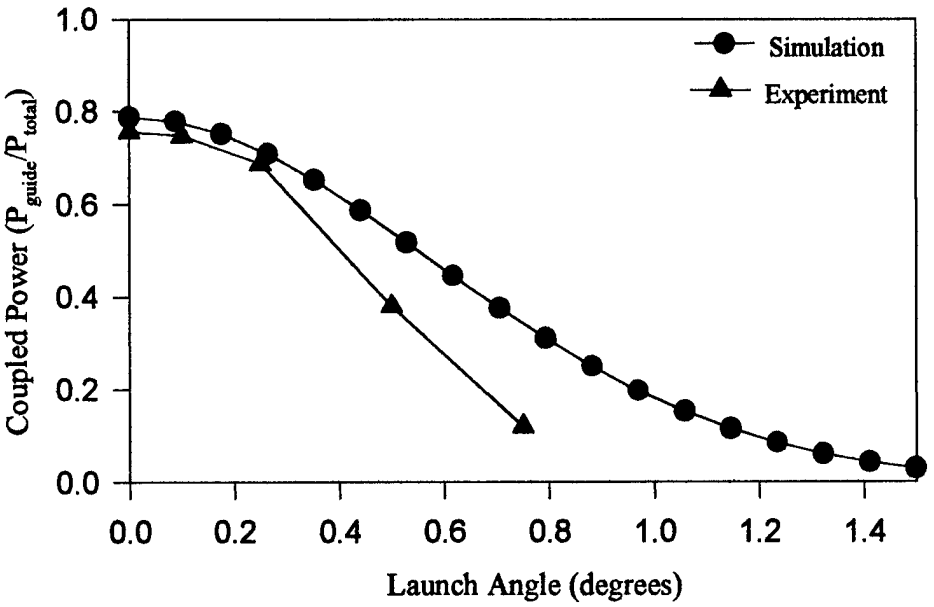

Figure 5.8 Ratio of signal diode power trapped by the soliton waveguide at the output of the semiconductor optical amplifier.

5.5 SINGLE MODE LAUNCH DEVICES

A primary shortcoming in the evaluation of the solitons was that the launch angles and modes could not be precisely controlled and aimed. To overcome this, a soliton propagation device was designed with a single mode waveguide as the input to the soliton guiding region. This single mode waveguide provided gain as well as confinement to the launched beam. To determine the ability of the soliton to be deflected, a triangular region was inserted between the end of the single mode waveguide and wide area, soliton propagation region. As the index of refraction could be altered by carrier injection, the triangular region could be used to steer waves across it. Finally, the input to previous

devices required arranging the stripe off-normal to the facet to prevent the device from lasing. Although the design of this device permits the waveguide to be normal to the cleaved facet, a slight angle of 0.5° (1.75° external launch angle) was built into the waveguide to ensure lasing would not occur if the prism angle was set such that a lasing cavity could be created across the device.

5.5.1 DEVICE LAYOUT

Following the successful beam guiding experiments, a device designed to launch, steer, and guide a signal beam from a single input to any number of outputs was fabricated. The basic device, shown in Figure 5.9, incorporates a single mode waveguide, a steering prism, and finally a wide area, soliton propagation region. The input single mode waveguide acts as an amplifier to the soliton generation beam and as a low loss waveguide to the signal beam, assuming that the wavelength of the signal beam is below the absorption band of the semiconductor. Thus, the waveguide is a fixed ridge waveguide with an active contact to allow current injection into the ridge. This first waveguide also restricts the soliton generating beam, as well as the signal beam, to a very specific launch point and direction.

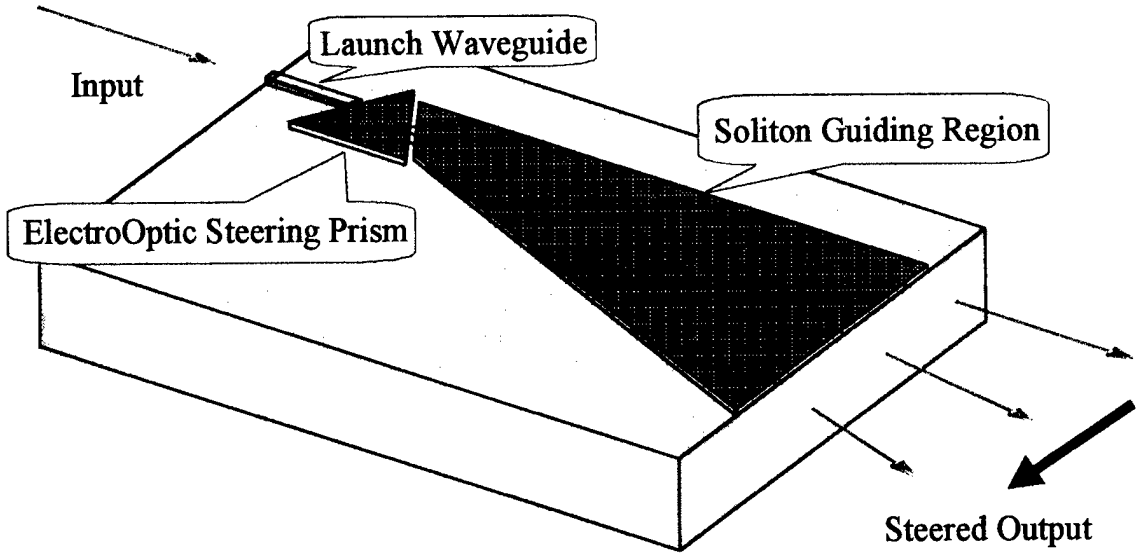

Figure 5.9 Prototype Soliton Steering Device

An electro-optic steering prism immediately follows the single mode launch waveguide. Creating a ridge weighted and electrically active triangular region following the single mode device forms this steering region. Deviation of the beam occurs when the beam encounters a spatial linear phase chirp created by a difference in the index of refraction between the prism region and the surrounding region.

Two geometries of prisms were designed into the testing mask. In the first, a right angle prism is placed close to the waveguide. This prism minimizes the distance the soliton pump beam travels without amplification, however, it is the most inefficient for steering. The second uses an equilateral prism which does just the opposite, by providing most loss, however, with the best steering. If this prism is operated into the gain region,

the maximum distance the soliton launch beam travels without amplification is eight microns.

To permit independent control of the soliton steering, the prism's electrical contacts are isolated from those of the other two regions. This isolation requires an electrically inactive gap on either side of the prism. The gap, however, forms an absorption region for the soliton beam and must be minimized. Physical fabrication limits impose the tightest restrictions upon this separation. Our fabrication tools provided the ability to faithfully reproduce devices possessing a feature size of one micron or larger. Consequently, the separation between the single mode waveguide and the closest edge of the steering prism was selected at 2 microns to permit high yield during subsequent fabrication runs. Finally, a wide area waveguide forms the gain region necessary for a soliton to form. This region is identical to the regions tested in Chapter 4.

5.5.2 THEORETICAL DEFLECTION

Because etching a ridge around the prism changes the upper cladding boundary conditions, there is a constant fixed shift in the index of refraction. This is the same shift as formed by the ridge of the single mode waveguide. Appendix B describes methods for calculating this index shift. In addition of the fixed shift, a controllable shift can be imparted onto the prism using either the electro-optic, or reverse biased, effect where

$$\Delta n = n_r^3 r_{41} \frac{V}{d} \tag{5.4}$$

where r_{41}, the electro-optic coefficient, for GaAs is $1.4\times10^{-12}\ m/V$ and V is the voltage applied across the device[75]. Since the bulk of the field drops across the active region, d=0.2 microns, the expected change in the index of refraction is $\Delta n = 3\times10^{-4}V$. This method for steering the beam cannot be used because the prism acts as a strong absorber when reverse biased. Additionally, imparting an index change of 0.01 on the material requires 33 volts across the **pn** junction. This is well beyond the reverse bias breakdown voltage and would destroy the device.

On the other hand, forward biasing the region can reduce or eliminate absorption and induce a change in the index of refraction through both the Burstein-Moss effect and the plasma effect, discussed earlier. Phase shift measurements on a single mode device, described in chapter 3, indicate that the shift in the index will approximately be $\Delta n = 7.52\times10^{-7}J$ where J is the current density through the device. Using this number and the right angle prism scheme, the angular for a right prism with an apex angle α will be

$$\Delta\theta = a\sin\left(\frac{(n+\Delta n)}{n}\sin(90-\alpha)\right)-\alpha \tag{5.5}$$

The deviation angle created by the equilateral prism is given by[76]

$$\Delta\theta = a\sin\left\{\sin(60°)\sqrt{\frac{(n_0+\Delta n)^2}{n_0^2}-\sin^2(30°)}-\sin(30°)\cos(60°)\right\}-30° \tag{5.6}$$

assuming the apex angle of the prism is 60° and the input beam is parallel to the base of the equilateral prism. Decreasing the apex angle of the right prism to very small number can yield large deviations for small changes. The negative aspect of using this prism is that the distance the wave must travel prior to entering the gain region increases drastically for decreasing angles. As such, only the 45-degree right and 60-degree equilateral prisms were analyzed during this research.

5.5.3 MEASURED DEFLECTION

A soliton creation beam was launched into this device and the output imaged in the same manner as the measurements taken in Chapter 4. In this experiment, however, the single mode area, triangular prism area, and soliton area all required separate contacts and drivers. The input waveguide and soliton creation regions were pulsed, but high to destructive continuous currents drove the triangular steering region. The position of the soliton measured against the injection current in the triangular region is shown in. Using the electro-optic data presented in Chapter 3, the deviation angle versus change in refractive index along the theoretical deviation, is shown in Figure 5.11. The departure of the measured deviation from theory results from leakage of current through the sides of the device and in the area leading up to the prism. Other deviations result from the current spreading away from a strictly triangular region just below the contact area resulting in a "fuzzy" prism. Finally, the current density entering the device is very high. As such, thermal or carrier saturation effects, which increase the index of refraction, may

limit the ultimate shift in the index. The angular deviation theory can be fit to the data by including an efficiency term that ratios the injection current. Fitting to the measured data yields an efficiency of 0.33, which is the solid line shown in Figure 5.11.

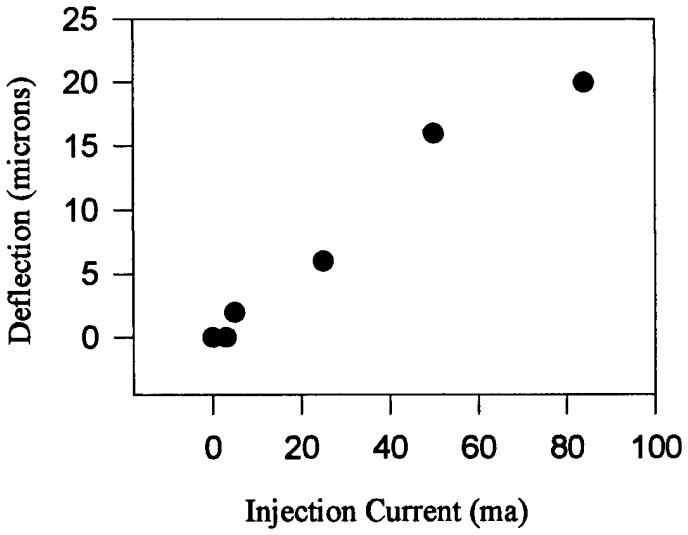

Figure 5.10 Measured Soliton Deflection at various injection currents

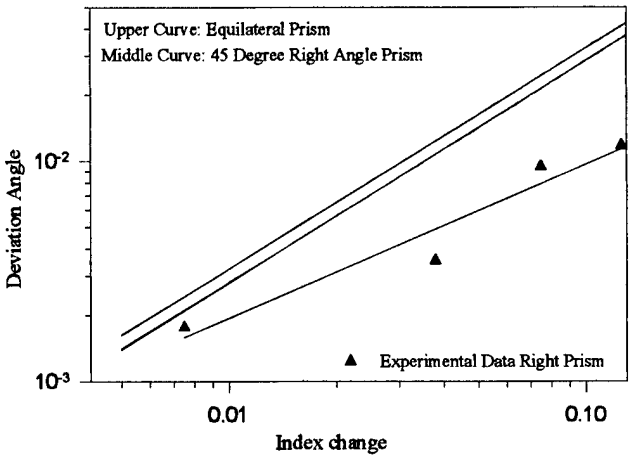

Figure 5.11 Beam deviation with injected current. Theoretical deviations shown for a right angle and equilateral prism.

5.6 CRITERIA FOR FUTURE DESIGNS

The beam guided using this experiment had a FWHM beam waist of 8 microns with a very multimode guided beam. As other experiments have shown nearly perfect guiding, it can be assumed that a 6-micron soliton could guide a 6-micron wave. If this distance is used to separate output waveguides, this device could theoretically switch a single input beam to 4 output waveguides while maintaining a cross talk ratio less than 2 to 1.

The amount of beam deviation created by the steering prism depends upon the change in the index of refraction in the prism. Increasing or decreasing the number of carriers in the prism area through electrical injection accomplishes this task. It should be noted, however, that the carrier-induced shift is dispersive in nature and will steer the soliton and signal beams differently. The amount of deviation the prism can effect no more than 0.6 degrees, and the variance in the index of refraction between the signal and soliton beam has been calculated to be about 60%. Using this 60%, the variance in angle between soliton and signal will be 0.2 degrees and the amount of energy confined in the soliton beam will drop from 80% for a perfect launch to 70%. Although the energy confined will decrease, the increase in cross talk is small, and the device continues to show promise as an effective method of steering information between points.

The angle of the output soliton to the cleaved edge of the device is the angle of launch at the input side. If the information guided through the device is to be coupled to output waveguides, the angle of the incoming information must be matched to the angle of the output waveguides. Using a 1xN device permits the output waveguides to be angled to

match the angle of the approaching soliton. However if an NxN device is designed, the soliton could approach from a variety of angles. Placing prisms on the input as well as the output will provide angular compensation for an array of input angles. Note that the continuous matching of input and output prisms may prove a daunting task for a commercial device.

The maximum reconfiguration time of the device is the time required to return the material to its equilibrium condition. This is the time to pump carriers into the conduction band to replace those depleted by the soliton beam. Measurements done on semiconductor optical amplifiers indicate that the re-pumping time constant is on the order of 1 ns. It should be expected that this would be a worst case time constant due to the fact that a large pool of carriers spatially exist in the conduction band to either side of the generated soliton that may return the soliton region to near equilibrium in much shorter times. Thus, this would permit the device to be reconfigured at a minimum rate of 1GHz.

Experiments measuring these effects are the subject of a future research project.

CHAPTER 6: CONCLUSION

6.1 OVERVIEW

During the introduction of this dissertation, the mathematical derivation behind solitary wave formation was reviewed. This provided the minimum requirements that a material should possess to support the possibility of solitary wave formation. In any system, the major factor to overcome was the amount of optical intensity needed to produce a large enough shift in the spatially localized index of refraction to overcome diffraction. Typical materials used require optical intensities in excess of 1 GW/cm^2 to form solitary waves. Although new polymer materials possessing high nonlinearity coefficients have been fabricated and tested, they tend to be unstable over long periods of time. In addition, materials compatible with current electronic circuitry and processing technology could provide an advantage in future monolithic integration of electrical driving circuits with, optical sources, photonic processing, and transmission circuitry as well as optoelectronic receivers.

Theoretical studies indicated that semiconductor optical amplifiers may provide enough intensity dependent refractive index changes to produce spatially self-confined

waves. In particular, GaAs devices possess these optical qualities as well as the potential for monolithic integration of this material with electronic circuitry in a relatively mature fabrication technological base. Although time resolved studies of the response of the electronic nonlinearities in the femptosecond regime indicated that a large negative nonlinearity existed during the first 50 femptosecond of the pulse, this nonlinearity quickly vanished and a large, slower speed, positive self-focusing nonlinearity resulting both from the direct influence of a decrease of excited carriers in the device and the causality effect due to the shift in the absorption edge. The penalty paid, however, is that the speed of the nonlinearity required that the optical pulse creating this nonlinearity must last several times longer in duration than the period of the initial negative going intensity dependent index shift, or several tens of picoseconds. Furthermore, the index of refraction shift created by the incident solitary wave existed within the device until the depleted carriers could be replaced by electrical pumping, commonly acknowledged as requiring 1 nanosecond. A quick analysis shows that a device employing this mechanism to transport information from an input to a corresponding output requires approximately 1.0 nanoseconds for reconfiguration, allowing such a device to be reconfigured at a rate of 1/2 gigahertz. As this would be a single stage switch, this technology could provide a 100x improvement in switch configuration over traditional fixed networks fabricated using 2x2 couplers in a tiered network.

In our venture to demonstrate optical self focusing and beam guiding within GaAs semiconductor optical amplifiers, a characteristic double heterostructure waveguide was designed, grown, and fabricated using the techniques outlines in chapter 2.

Characterization of these devices showed that a strong optical nonlinearity exists at the peak of the gain spectrum. This not only agreed with theoretical calculations of the device, but quantitative measurements of the nonlinearity indicated that the effect was strong enough to produce self focusing with relatively small input optical intensities. Following this, a device was fabricated to demonstrate and analyze spatial self focusing and the subsequent successful creation of spatially self focused waves. After analysis of the characteristics of these waves, a second beam spectrally separated from the first one by 60 nanometers was added to the beam and was found to be spatially contained by the index profile created by the solitary wave.

As a demonstration of a device using this effect, an electro-optic steering prism was added into the device, and used to steer the output of the device between an array of outputs. These demonstrations showed the ability of the device to direct an output over a 30 microns output region using as little as 5 volts on the steering prism, thereby completing the initial phase of the overall project and this dissertation.

6.2 PRIMARY CONTRIBUTION AND MEASUREMENTS

Specific measurements of relevance were made using several characterization and soliton measurement techniques. The primary measurements made using single mode devices produced the following important conclusions

A) The nonlinearity follows the gain spectrum and the peak of the nonlinearity and gain correspond.

B) The magnitude of the nonlinearity when the device was biased near lasing was measured to be $n_2=5.7x10^{-10}$ cm^2/W using a single mode waveguide and a discrete Mach-Zehnder interferometer.

C) Spatial solitary waves were demonstrated using an input intensity of $1.1MW/cm^2$. Measuring the spatial profiles of these waves, the nonlinearity was estimated to be $2.8x10^{-10}$ cm^2/W which was in good agreement with the value measured with the interferometer.

D) The change in the index of refraction was theoretically shown to be $5.6x10^{-4}$ by comparing the output mode profile of a second wave guided by the primary solitary wave.However using the nonlinear refractive index found above would give a net change in the refractive index of $1.4x10^{-3}$.

6.3 FUTURE WORK

In the quest to answer the basic questions concerning spatial soliton creation in a semiconductor optical amplifier, many more questions have arisen. In an attempt to promote and guide future research, the following is a list of issues I feel should be explored in depth to answer the questions of whether this technology is an interesting scientific research topic, or a potentially viable commercial product technology.

6.3.1 SOLITON LIFETIME

The lifetime of the induced index of refraction created by the soliton requires analysis. This information determines the amount of time the created waveguide can exist and still be used, as well as determining the time the waveguide region requires to completely recover and return to the non-soliton state. This experiment requires a pump probe type of measurement where the pump and probe are synchronized. The easiest method initially considered is to pass a pump and orthogonal probe through a single mode active waveguide placed in the arm of an interferometer. This method, however, may not work due to the large amount of spontaneous emission in the orthogonal polarization state, thereby swamping the probe signal. A method that may work better, but one that requires more laser power, is to pass a chopped probe as a signal beam just behind the large soliton creating pump pulse. The polarization filtered peak of the probe output would be measured and analyzed as the probe is delayed further from the pump. The drawback here being that the response of the device would be convoluted with the moderately long probe pulse. As the general shape of the response function can be assumed to be exponential and the temporal shape of the probe in known, the two functions may be reasonably deconvolved.

6.3.2 WAVEGUIDE LAUNCH AND COLLECTION EFFICIENCY

Although we have demonstrated that solitons created in a semiconductor optical amplifier can be used to guide other information, the question of launch, guiding, and collection efficiency remains to be analyzed. In addition, the distance an optical wave can travel without gain and be resurrected into a soliton should be analyzed. In this experiment, the goal is to analyze the difference between waveguiding, launch, non-gain propagation loss, and soliton carrier loss. In changing the variables of input waveguide length, non-gain spacing, and soliton region spacing each of these effects may be decoupled. It should be stressed that sample to sample deviations force as many variants of the structure to be fabricated onto the same sample to ensure uniformity between devices.

6.3.3 SOLITON INTERACTION

In a more advanced NxN device, multiple solitons may be crossing the gain region, and each other, simultaneously. As the address of the output from the input may be a fixed voltage on an electro-optic prism, it is critical to determine the effects of crossing solitons on the target stability of the output. In this experiment, shown in figure 6.3, two solitons are launched into the same area and set to cross at varying angles. The soliton interaction, angular deviation caused by index profiles, or possibly trapping (although

this seems unlikely for a non-instantaneous nonlinearity), should be analyzed on the output of the device.

6.3.4 CROSS TALK (1XN) DEVICE

Cross talk between crossing solitons and in adjacent outputs will drive the packing density of the device. As such, experiments must be performed to determine the cross talk isolations. This experiment, shown in figure 6.4, uses the same a complete 2x2 device with varied input and output spacing. Two spacings may be sufficient to determine cross talk vs. distance, however, at least three varying spacings will help confirm trends in data.

6.3.5 COMPENSATING RECEPTION ANGLES

In a device with one input and N outputs, each of the outputs can be angled precisely toward the apex of the launching electro-optic prism ensuring the optimum reception efficiency possible. In the case with multiple inputs and outputs, however, the receiving waveguides cannot be angled at all inputs simultaneously. Thus, the placement of reception prisms at the receiving waveguides can help compensate the variance in reception angle deviation from the angle of the reception waveguide. Factors to be determined are whether the angles can be compensated and what efficiency can be

achieved, as well as, what precision of electro-optic control voltage is necessary to achieve a minimum signal to noise ratio.

6.3.6 FULL DEMONSTRATION DEVICE (NXN)

Eventually most of the critical design issues will be answered, and a device complete with multiple inputs and outputs needs to be demonstrated. A mass extension of this device, shown in figure 6.6, incorporates an 8x8 geometry. Each launching waveguide requires a steering electro-optic prism, as does each receiving waveguide. Aside from the ability to be used bidirectionally, the steering electro-optic prisms on each side of the soliton region will compensate for variances in reception angles caused by the differing launch positions.

APPENDIX A: DERIVATION OF THE NON-LINEAR WAVE EQUATION FOR SPATIAL SOLITONS

In developing the non-linear wave equation, we start, of course, with Maxwell's equations for non-magnetic materials, which are

$$\nabla x E = \frac{-\partial B}{\partial t}$$
$$\nabla x H = J + \frac{\partial D}{\partial t}$$
$$\nabla \cdot D = \rho$$
$$\nabla \cdot B = 0$$
$$D = \varepsilon_0 E + P \approx \varepsilon_0 \varepsilon_r E = \varepsilon E$$
$$B = \mu_0 H$$

An optical field is commonly expressed as a function of a traveling envelope (A in this equation) and a traveling phase wave.

$$E(x,y,z,t) = \frac{1}{2} A(x,y,z,t) e^{j(\omega t - kz)} + \frac{1}{2} A(x,y,z,t) * e^{-j(\omega t - kz)}$$
$$E(x,y,z,t) = \frac{1}{2} A(x,y,z,t) e^{j(\omega t - kz)} + c.c.$$

The first step in developing the wave equation is to take the curl of the first Maxwell's equation (and assume a source free medium ($\nabla \cdot D = 0$)).

$$\nabla x \nabla x E = \nabla x(-\partial B/\partial t)$$
$$\nabla(\nabla \cdot E) - \nabla^2 E = -\partial(\nabla x B)/\partial t$$

Although we set $\nabla \cdot D$ to zero for a source free medium, the assumption that the $\nabla \cdot E$ term is also zero, in some cases, is not valid. Assuming that ε contains polarization effects and varies spatially

$$D \approx \varepsilon E$$
$$\nabla \cdot D = \nabla \cdot (\varepsilon E)$$
$$0 = \nabla \varepsilon \cdot E + \varepsilon \nabla \cdot E$$
$$\varepsilon \nabla \cdot E = -\nabla \varepsilon \cdot E$$
$$\nabla \cdot E = -E \cdot \frac{\nabla \varepsilon}{\varepsilon}$$

This tells us that if there is a gradient in the permitivity, or index of refraction, the term $\nabla \cdot E$ is not zero. Many waveguide structures such as graded index waveguides or third order nonlinear materials hosting solitary waves have such a gradient. Fortunately, the change in permittivity is very small, and in most cases can be totally ignored, as we shall do.

$$0 - \nabla^2 E = -\partial(\nabla x \mu_0 H)/\partial t$$

$$\nabla^2 E = \mu_0 \partial(\nabla x H)/\partial t$$

$$\nabla^2 E = \mu_0 \partial(J + \frac{\partial D}{\partial t})/\partial t$$

$$\nabla^2 E = \mu_0 \partial^2(\varepsilon_0 E + P)/\partial t^2$$

$$\nabla^2 E = \frac{1}{c^2}\partial^2 E/\partial t^2 + \mu_0 \partial^2 P/\partial t^2$$

where

c is the speed of light in a vacuum

J is assumed approximately constant with time

If this was free space (P=0), the final equation above would be the Helmholtz wave equation.

$$\nabla^2 E - \frac{1}{c^2}\partial^2 E/\partial t^2 = 0$$

We deal, however, in polarizable material. In the time domain, the polarization is the convolution of the nonlinear response with the input electric field.

$$P^{(1)i}(t) = \varepsilon_0 \int_{-\infty}^{\infty} \chi^{ij}(t-\tau) E_j(\tau) \partial\tau$$

$$P^{(2)i}(t) = \varepsilon_0 \int_{-\infty}^{\infty}\int_{-\infty}^{\infty} \chi^{ijk}(t-\tau_1, t-\tau_2) E_j(\tau_1) E_k(\tau_2) \partial\tau_1 \partial\tau_2$$

$$P^{(3)i}(t) = \varepsilon_0 \int_{-\infty}^{\infty}\int_{-\infty}^{\infty}\int_{-\infty}^{\infty} \chi^{ijkl}(t-\tau_1, t-\tau_2, t-\tau_3) E_j(\tau_1) E_k(\tau_2) E_l(\tau_3) \partial\tau_1 \partial\tau_2 \partial\tau_3$$

where
units are in MKS
χ is the susceptibility of the material and
$P^{(x)}$ is the x^{th} order non-linearity

One way to handle the complexity of these convolutions is to work with the polarization in the frequency plane, where the convolutions of time functions become multiplication of the frequency functions. A second method is to assume that the susceptibility responds much faster than the electric field and can be approximated as an instantaneous function in time. This reduces to polarization to

$$P^{(1)i}(t) = \varepsilon_0 \chi^{ij} E_j(t)$$
$$P^{(2)i}(t) = \varepsilon_0 \chi^{ijk} E_j(t) E_k(t)$$
$$P^{(3)i}(t) = \varepsilon_0 \chi^{ijkl} E_j(t) E_k(t) E_l(t)$$

This equation can again be simplified by assuming a specific set of experimental conditions. If we are interested only in one input field, we set a fixed and specific crystal orientation, and we analyze only the fundamental frequency output (self-action term), we can replace the susceptibility tensors with effective susceptibilities valid only for our given experimental setup. This can be justified in semiconductor waveguide experiments where the waveguide is oriented on a specific crystal direction and only the light that is confined to the waveguide is of interest. Although the total polarization is a complex function, the reduced equation is a power series driven by the applied field.

$$P = \varepsilon_0\left(\chi^{(1)}E + \chi^{(2)}E^2 + \chi^{(3)}E^3 + \chi^{(4)}E^4 + \ldots\right)$$

where $\chi^{(n)}$ is the n^{th} order **effective** susceptibility for our specific setup (MKS units). Inserting this into the Maxwell's equation above

$$\nabla^2 E = \frac{1}{c^2}\left[\partial^2 E/\partial t^2 + \chi^{(1)}\,\partial^2 E/\partial t^2 + \chi^{(2)}\,\partial^2 E^2/\partial t^2 + \chi^{(3)}\,\partial^2 E^3/\partial t^2\right]$$

In the class of materials we are concerned with is called centro-symmetic, third order nonlinear. This means that the material is electronically symmetric about the center of the molecule, thus the even order non-linearities cannot exist. The odd order nonlinearities can exist. Of these nonlinearities, only the third order nonlinearity will be significant, unless the field strength is extremely high. In this case the wave equation reduces to

$$\nabla^2 E = \frac{1}{c^2}\partial^2 E/\partial t^2 + \mu\varepsilon\chi^{(1)}\,\partial^2 E/\partial t^2 + \mu\varepsilon\chi^{(3)}\,\partial^2 E^3/\partial t^2$$

The $\chi^{(3)}$ term contains the cube of the electric field. Cubing the field defined at the beginning of this paper

$$
\begin{aligned}
E(x,y,z,t)^3 &= \left\{\frac{1}{2}A(x,y,z,t)e^{j(\omega t-kz)} + \frac{1}{2}A(x,y,z,t)*e^{-j(\omega t-kz)}\right\}^3 \\
&= \frac{1}{8}\begin{bmatrix} A(x,y,z,t)^3 e^{3j(\omega t-kz)} + 3A(x,y,z,t)^2 e^{2j(\omega t-kz)} A(x,y,z,t)*e^{-j(\omega t-kz)} + \\ 3A(x,y,z,t)e^{j(\omega t-kz)} A(x,y,z,t)^{*2} e^{-2j(\omega t-kz)} + A(x,y,z,t)^{*3} e^{-3j(\omega t-kz)} \end{bmatrix} \\
&= \frac{1}{8}\left[A(x,y,z,t)^3 e^{3j(\omega t-kz)} + c.c.\right] + \frac{3}{8}\left[\left|A(x,y,z,t)\right|^2 A(x,y,z,t)e^{j(\omega t-kz)} + c.c.\right] \\
&= \frac{1}{8}\left[A(x,y,z,t)^3 e^{3j(\omega t-kz)} + c.c.\right] + \frac{3}{4}|E|^2 E
\end{aligned}
$$

In our case, we are interested only in the self-action terms, or the terms that result in the same frequency as the input term. The $|E|^2$ term is estimated to be independent of time and can be removed from the derivative. This term is also directly related to the positional intensity $I = |E|^2/2\eta$ where $\eta = \sqrt{\mu/\varepsilon}$ or $1/(c\varepsilon_0 n_0)$. Regrouping, the equation now becomes

$$
\nabla^2 E = \frac{\left(1+\chi^{(1)}+\frac{3}{2}\chi^{(3)}I\eta\right)}{c^2}\partial^2 E/\partial t^2
$$

Now, the interesting term $1+\chi^{(1)}+3\chi^{(3)}I\eta/2$ is a unitless term that, in effect, ratios the speed of the optical wave in a material to that of the wave traveling in free space. This might be recognized as the square of the optical index of refraction n. It is common to represent the index of refraction as a linear and nonlinear component of the form $n(I) = n_0 + n_2 I$. To find the value of n_2, we square the common form equation $n(I)^2 = n_0^2 + 2n_0 n_2 I +$

$n_2^2 I^2$. Because n_2 is a very small number, we can ignore the final term as insignificant and solve the simple equation

$$n_0^2 + 2n_0 n_2 I = 1 + \chi^{(1)} + 3\chi^{(3)}\eta I / 2$$
$$n_0 = \sqrt{1 + \chi^{(1)}}$$
$$n_2 = {}^{3\chi^{(3)}\eta}\!/_{4n_0} = {}^{3\chi^{(3)}}\!/_{4c\varepsilon_0 n_0^2}$$
$$n(I) \approx n_0 + n_2 I$$

Finally, the wave equation becomes

$$\nabla^2 E - \frac{n(I)^2}{c^2}\,{}^{\partial^2 E}\!/_{\partial t^2} = 0$$

Now let's start executing the derivatives. We assume that the spatial and time variables are separable. Additionally, we choose to analyze the wave in a frame moving with the envelope, the time dependence of the envelope drops off the and second derivative with time produces the original function times $-\omega^2$.

$$\nabla^2 E + \frac{n(I)^2 \omega^2}{c^2} E = 0$$
$$\nabla^2 E + n(I)^2 k_0^2 E = 0$$
$$k_0 = {}^{\omega}\!/_{c}$$

The Laplacian represents the spatial derivatives. The Laplacian in rectangular coordinates is

$$\nabla^2 = \partial^2/\partial x^2 + \partial^2/\partial y^2 + \partial^2/\partial z^2$$

Referring to the form of the field stated at the start of the derivation, the x and y terms are independent and will be referred to as the transverse coordinates. The Laplacian for the transverse coordinates will be the symbol $\nabla^2_{\perp}$. The z term appears both in the amplitude and traveling terms and the Laplacian of the z term is (dropping the non z dependent terms)

$$\begin{aligned}
\partial^2 E(z)/\partial z^2 &= \partial^2/\partial z^2 \left(A(z)e^{-jkz} + c.c.\right) \\
&= \partial/\partial z \left(A(z)(-jk)e^{-jkz} + \partial A(z)/\partial z\, e^{-jkz}\right. \\
&= (-jk)\left\{A(z)(-jk)e^{-jkz} + \partial A(z)/\partial z\, e^{-jkz}\right\} + \partial A(z)/\partial z(-jk)e^{-jkz} + \partial^2 A(z)/\partial z^2\, e^{-jkz} \\
&= -k^2 A(z)e^{-jkz} - 2jk\,\partial A(z)/\partial z\, e^{-jkz} + \partial^2 A(z)/\partial z^2\, e^{-jkz}
\end{aligned}$$

The first and second term of this equation contain the term k which is the wave propagation constant in the z direction ($k = nk_0 = n2\pi/\lambda$). Values for k in the optical range are large. For a near infra-red beam (800 nm) in glass (n=1.5), $k = 1.178 \cdot 10^7\ m^{-1}$. Thus any term without k will be quite insignificant, unless the pulses are short.

Why short? To examine the approximate magnitude for the derivative terms, lets take a snap-shot of the pulse (again, use a moving reference frame) and set the traveling envelope function A(z,t) in terms of z. For a typical short laser pulse, the function is gaussian, or very close to it, which, at any given time, has the form

$$A(z) \propto e^{-\left(\frac{z-z_0}{w}\right)^2}$$

where

z is the dependent variable
z_0 represents the displacement along the z axis, 0 for a moving reference frame
w represent the relative spatial width of the pulse

Laser pulses vary greatly in temporal pulse width, but pulses from active mode locked lasers are typically 1-100 picoseconds. Kerr lens mode locked Titanium Sapphire laser pulse widths can be as short as 6 femptoseconds, but typically range from 100-3000 femptoseconds. The relationship between temporal width and spatial width (w) is given by

$$w \approx {t_0 c}/{n}$$

where

t_0 is the e^{-1} temporal pulse width
c is the speed of light
n is the optical index of refraction

For a 1 picosecond pulse in glass (n=1.5) w=200 microns. Now examine the derivatives of A(z)

$$A(z) = e^{-\left(\frac{z-z_0}{w}\right)^2}$$

$$\partial A(z)/\partial z = -2\frac{z-z_o}{w^2}A(z)$$

$$\partial^2 A(z)/\partial z^2 = \left\{\frac{-2}{w^2} + 4\frac{(z-z_0)^2}{w^4}\right\}A(z)$$

The $(z-z_o)$ term in the above equations is localized about the Gussian function and is of the order of w. Thus the first derivative has a maximum on the order of 1/w, or in the case of a 1-picosecond pulse, 5000 m^{-1}. The second derivative has a maximum on the order of $1/w^2$ or $2.5 \cdot 10^7$ m^{-2}. Now looking at the full equation (i.e. multiplying by k^2 and k), the magnitude the third term is still less than three orders of magnitude less than the second term. Thus, the second derivative can be ignored. This approximation is also called the slowly varying envelope approximation, meaning that the envelope of the function varies much slower than the frequency of the electromagnetic wave. Substituting the terms for A(z) and its first derivative back into the wave equation

$$\nabla^2 E + k_0^2 n(I)^2 E = 0$$

$$\nabla_\perp^2 A - 2jk\,{}^{\partial A}\!/_{\partial z} - k^2 A + k_0^2 n(I)^2 A = 0$$

$$\nabla_\perp^2 A - 2jk\,{}^{\partial A}\!/_{\partial z} - n_0^2 k_0^2 A + k_0^2 n(I)^2 A = 0$$

$$\nabla_\perp^2 A - 2jk\,{}^{\partial A}\!/_{\partial z} + k_0^2 \left(n(I)^2 - n_0^2\right) A = 0$$

We can further simplify this equation by noting that $n_2 I$ is very small in comparison to n_0 so that the index square terms can be approximated by

$$\begin{aligned} n(I)^2 - n_0^2 &= (n(I) + n_0)(n(I) - n_0) \\ &= (n_0 + n_2 I + n_0)(n_0 + n_2 I - n_0) \\ &= (2n_0)(n_2 I) \\ &= (2n_0) n_2 \,{}^{|A|^2}\!/_{2\eta} \\ &= n_0 n_2 |A|^2 / \eta \end{aligned}$$

Substituting this back into the wave equation

$$\nabla_\perp^2 A - 2jk\,{}^{\partial A}\!/_{\partial z} + k_0^2 \left(n(I)^2 - n_0^2\right) A = 0$$

$$\nabla_\perp^2 A - 2jk\,{}^{\partial A}\!/_{\partial z} + k_0^2 \frac{n_0 n_2}{\eta} |A|^2 A = 0$$

$$\nabla_\perp^2 A + k_0^2 \frac{n_0 n_2}{\eta} |A|^2 A = 2jk\,{}^{\partial A}\!/_{\partial z}$$

If taken in a 1-dimensional waveguide, this equation has an exact, steady state, solution, called a spatial soliton, of the form

$$A(x,z) = A_0 \operatorname{sec} h\left(\frac{x}{W_0}\right) e^{-j\frac{z}{4z_0}}$$

$$I(x,z) = \frac{|A(x,z)|^2}{2\eta} = \frac{A_0^2}{2\eta} \operatorname{sec} h^2\left(\frac{x}{W_0}\right)$$

where

$$W_0 = \sqrt{2\eta / n_2 A_0^2 k^2}$$

$$z_0 = \frac{1}{2} k W_0^2 = \pi W_0^2 / \lambda$$

APPENDIX B: KRAMERS-KRONIG RELATIONSHIP

The polarizability of a material is commonly written as a Taylor expansion about the applied electric field

$$P = \epsilon_0 (\chi^{(1)} E + \chi^{(2)} E^2 + \chi^{(3)} E^3 + \ldots)$$

The susceptibility tensors χ are frequency dependent have both real and imaginary parts. In simple situations, such as linear materials with only $\chi^{(1)}$ terms or in Kerr like materials, the real part of the susceptibility relates to the index of refraction, and the imaginary part relates to the absorption or gain. The Kramers-Kronig relationship defines a specific relationship between the real and imaginary parts of this or any real function.

As with any function defined in the frequency domain, the Fourier transform links this function to a corresponding time domain function. It is this function that forms the basis for the Kramers-Kronig Relationship. The causal principle states that the response to a stimulus cannot occur prior to the application of the stimulus. In our case, a polarization response to an electric field cannot occur prior to the application of the field. Assume that the stimulus is applied at time zero and the response to the stimulus is an arbitrary function

f(t). By the causal principle, *f(t)* must be zero for times less than zero. As such, *f(t)* multiplied by a step function at zero is still *f*(t) or $f(t) = f(t) * step(0)$.

The frequency domain response is found be executing the Fourier transform.

$$F(\omega) = \Im\{f(t)\} \otimes \Im\{step(0)\}$$

$$F(\omega) = i \int_{-\infty}^{\infty} \frac{F(\omega`)}{\omega - \omega`} \partial\omega`$$

where the integral is the execution of the convolution function. Now, allowing *F(ω)* to have both real and imaginary parts, $F(\omega) = F`(\omega) + iF``(\omega)$, equation 3 becomes

$$F`(\omega) + F``(\omega) = i \int_{-\infty}^{\infty} \frac{F`(\omega`) + iF``(\omega)}{\omega - \omega`} \partial\omega`$$

Real and imaginary parts of an equality must be independently equal, thus

$$F`(\omega) = -\int_{-\infty}^{\infty} \frac{F``(\omega)}{\omega - \omega`} \partial\omega`$$

$$F``(\omega) = \int_{-\infty}^{\infty} \frac{F`(\omega`)}{\omega - \omega`} \partial\omega`$$

Thus, the real and imaginary parts of the frequency response are related through the Kramers-Kronig integral. In practice, this integral is relatively easy to graph by noting that the integral is the convolution of the real or imaginary part of the response with the function within the integral.

As an example, apply the Kramers-Kronig relationship to a Gaussian response function, shown in figure 2. As the integral function approaches from the low frequency side, the convolution will follow the same sign as the function. As the convolution nears the center of the Gaussian, the convolution turns towards the axis, and hits the axis when the two functions have the same center point. As the integral function proceeds further, the result is negative, then turns towards the axis as the two functions separate.

An important corollary to this equation is that changes in the absorption or gain can be directly related to changes in the refractive index directly without measuring the entire absorption spectra.

$$\Delta n(\omega) = -\int_{-\infty}^{\infty} \frac{\Delta\alpha(\omega)}{\omega - \omega'} \partial\omega'$$

If the change in the absorption, or gain, is caused by an incident optical intensity, then this equation calculates the change in optical refractive index, $n_2 I$.

Although powerful in its simplicity, the greatest drawback to this equation is that to produce an exact form of the change in the index, the change in the absorption must be known throughout the entire spectrum. Often this is either impossible or impractical. Fortunately, the change to the index at a given frequency drops dramatically as the absorption measurement range further from the wavelength of interest. Therefore, this method can be used to determine a qualitative measure of the change in the index of refraction given a limited spectrum measurement of the change in the absorption.

APPENDIX C: WAVEGUIDE MODE CALCULATIONS

Electric fields traveling through a waveguide must conform to continuous boundary conditions. The first condition mandates that the fields decay to zero at large distances away from the core of the waveguide. Secondly, the field in the core may have oscillatory behavior. Finally, that the normal components of the electric flux density must be equal ($D_{n1} = D_{n2}$), and that the tangential electric field and its derivative must be equal ($E_{t1} = E_{t2}$ and $\frac{dE_{t1}}{dx} = \frac{dE_{t2}}{dx}$). These assume zero charge at the boundaries. With the coordinate system set at $x=0$ for one boundary, and $x=h$ at the other, the solution of this system is

$$f(x) = e^{sx}\, e^{i(\omega t - \beta z)} \qquad \text{lower cladding region}$$

$$f(x) = \left(cos(\kappa x) + \frac{s}{\kappa} sin(\kappa x) \right) e^{i(\omega t - \beta z)} \qquad \text{guiding region}$$

$$f(x) = \left[cos(\kappa h) + \frac{s}{\kappa} sin(\kappa h) \right] e^{-p(x-h)} e^{i(\omega t - \beta z)} \qquad \text{upper cladding region}$$

The relationship between the decay and oscillation constants and the propagation constant, β, is found by substitution of these equations into the SWE discussed in

appendix A. Application of the boundary conditions to these equations yields the dispersion relationship

$$tan(\kappa h + m\frac{\pi}{2}) = \frac{\kappa(p+s)}{\kappa^2 - ps}$$

m in this equation is the order of the waveguide mode.

This solution applies only to configurations where the cladding layers are infinite. If the cladding is not infinite, such as in the case of the weighted waveguide, an additional set of boundary conditions must be applied. The math quickly become tedious and computerized solution methods exist to determine the propagation mode constants.

A lateral transmission method can be used to calculate propagation constants for a structure of any number of layers. The method uses the multiple beam interference method to calculate resonances in a multiple layer stack. Light at an interface of high index to low index will be total internally reflected for all angles greater than the total internal reflection angle. Certain angles, however, will cause the multiply reflected continuous waves within the waveguide to overlap constructively. These are the modes of the waveguide. At these specific angles, there exists a singularity in the angular transmission spectrum. Locating the angle of these singularities yields the propagation constant through the expression $\beta = k_n \, sin(\theta)$, where k_n is the propagation constant in the bulk material. The angles are found by dividing the structure into a series of regions and applying a matrix method to determine the series solutions for the structure. The matrix consists of an interface step defined by the matrix H_{12} (interface between layers 1

and 2) and a propagation matrix step defined by the matrix L_2 (propagation across layer 2).

$$H_{ij} = \frac{1}{\tau_{ij}} \begin{bmatrix} 1 & \rho_{ij} \\ \rho_{ij} & 1 \end{bmatrix}$$

$$L_j = \begin{bmatrix} e^{-ik_j} & 0 \\ 0 & e^{ik_j} \end{bmatrix}$$

where ρ_{ij} and τ_{ij} are the reflection and transmission coefficients; k_j is the material propagation constant.

The total transfer matrix is then

$$H_{12}L_2H_{23}L_3 \ldots L_{n-1}H_{n-1,n} = \begin{bmatrix} S_{11} & S_{12} \\ S_{21} & S_{22} \end{bmatrix}$$

where the angular dependence of the equation is found using Snell's Law. The final transmission and reflection of this stack is then

$$\rho = \frac{S_{12}}{S_{22}}$$

$$\tau = \frac{1}{S_{22}}$$

To implement this method, an angular ray at the first level of the waveguiding region is used to find the series of angles throughout the rest of the system. These angles are used to calculation the transmission and reflection coefficients for the H and L matrix elements, and the S matrix is calculated. The initial launch angle is varied to approach the singularities of the waveguide modes.

A Matlab code implementing this method appears at the conclusion of this appendix.

```
function dumb=main;
%
%  index = index of refraction of each layer
%  thick = thickness of each layer in meters
%  guide = the layer the angles will be set in.  All
%          other layer angles depend on the guide angle
%  lambda0 = wavelengh in free space
%  counts = number of wavelengths that will be analyzed
%           Note: the angle range is set by the pTh
%           statement inside the counts loop.
%
%  Program calls
%  Angles -> calculate all angles (complex) within the
%  stack
%  Stack  -> calculate transmission and reflection of the
%   stack

um=1e-6;
nm=1e-9;
ang=1e-10;
deg=2*pi/360;

%lambda_start=500*nm;
%lambda_end=1200*nm;
%lambda_inc=1*nm;
%lambda0=1000*nm;

%for mn=1:30,
%layers=mn*2;
%layers=4;
%n_top=1;
%n_low=1.5;
%n_high=2.0;
%n_sub=3.5;

%index(1)=n_top;
%for l=2:2:layers+1
%   index(l)=n_high;
%   index(l+1)=n_low;
%end;
%index(layers+2)=n_sub;

%k=round((lambda_end-lambda_start)/lambda_inc)
```

```
   %index=[3.59 3.08024 3.45164 3.590 3.45164 3.590 3.45164
3.590 3.45164 3.08024 3.590 1];
   %thick=[1 1.39*um 0.075*um 80*ang 80*ang 80*ang 80*ang
80*ang 0.075*um 0.93*um 1000*ang 1];

   %index=[3.59 3.08024 3.453164 3.590 3.453164 3.08024];
   %thick=[1 1.39*um 0.7385*um 0.008*um 0.7385*um 1];

   index=[3.1 3.58 3.1];
   thick=[1 0.2*um 1];

   lambda0=900*nm;

   %index=[1.40 1.50 1.45];
   %thick=[1 5*um 1];
   %lambda0=1000*nm;

   guide=2;
   counts=2000;
   j=sqrt(-1);
   %theta=0;

   for i=1:counts,
      pTh(i)=(90-(30*i/counts))*deg;
      [rho,tau,R,T]=stack(lambda0,index,thick,pTh(i),guide);
      pR(i)=abs(R);
      pT(i)=abs(T);
   end;

   subplot(1,2,1), plot(pTh/deg,pR,'r');
   %axis([60 90 -0.1 2000]);

   subplot(1,2,2), plot(pTh/deg,pT,'g');
   %axis([60 90 -0.1 2000]);

   modeangles=[];

   i=1;
   while i<counts,
   if pR(i)>5000,
      low=pTh(i-1)/deg;
      while pR(i)>5000,
         i=i+1;
         end;
      high=pTh(i)/deg;
      modeangles=[modeangles,(low+high)/2];
      end;
   i=i+1;
```

```
end;

kf=2*1.5*pi/lambda0;
kx=cos(modeangles*deg).*kf;
eff_index=index(guide)*sin(modeangles(1)*deg);
kx
modeangles
eff_index
end;
```

```
   function
[Srho,Stau,R,T]=stack(lambda,index,thick,theta,seed);

thetas=angles(index,theta,seed);

betas=cos(thetas).*index.*thick*(2*pi/lambda);

   i=sqrt(-1);
   k=length(index)-1;

   a=tan(thetas(k))/tan(thetas(k+1));
   tau=2/(1+a);
   rho=(1-a)/(1+a);
   S=[1 rho ; rho 1]./tau;

   for j=k:-1:2,
      a=tan(thetas(j-1))/tan(thetas(j));
      tau=2/(1+a);
      rho=(1-a)/(1+a);
      H=[1 rho ; rho 1]./tau;
      L=[exp(-i*betas(j)) 0 ; 0 exp(i*betas(j))];
      S=H*L*S;
   end;

   Srho=S(1,2)/S(2,2);
   Stau=1/S(2,2);

   R=abs(Srho)^2;
   T=(abs(Stau)^2)*(index(k+1)*cos(thetas(k+1)))/(index(1)*c
os(thetas(1)));
```

```
   function angs=angles(index,theta,seed);

%seed is the layer number that is calling all other angles

   l=length(index);
   angs(seed)=theta;
   i=sqrt(-1);

   for j=seed+1:1, %layers after seed
      aratio=index(j-1)*sin(angs(j-1))/index(j);
      iangs=imag(asin(aratio));
      rangs=real(asin(aratio));

      if abs(aratio)>1
     angs(j)=rangs-iangs*i;
      else
     angs(j)=rangs+iangs*i;
     end;

   end;

   for j=seed-1:-1:1, %layers before seed
      aratio=index(j+1)*sin(angs(j+1))/index(j);
      iangs=imag(asin(aratio));
      rangs=real(asin(aratio));

      if abs(aratio)>1
     angs(j)=rangs-iangs*i;
      else
     angs(j)=rangs+iangs*i;
     end;

   end;
```

```
   function n=kzeros(kappa);
   global nf ns nc h lambda k deg;

      t=tan(kappa*h);
      betas=(((k^2)*(nf^2))-(kappa^2));
      GS=sqrt(betas-((k^2)*(ns^2)));
```

```
   GC=sqrt(betas-((k^2)*(nc^2)));
   tr=(GS+GC)/(kappa*(1-(GS*GC/(kappa^2))));

   n=t-tr;

end;
```

APPENDIX D: DERIVATION OF THE BEAM PROPAGATION METHOD

A very powerful method of analyzing a beam propagating through a complicated material is the beam propagation method (BPM). The method is particularly powerful in circumstances where a closed form solution is not available. Additionally, the method provides insight into the evolution of steady state functions if those functions are not input directly to the structure. To show the power the beam propagation method, we start with the wave equation and expand the polarization about the fundamental frequency, using effective susceptibilities, for centro-symmetric (no even order nonlinearities), third and fifth order nonlinear, non-magnetic materials.

$$\nabla^2 E = \frac{1}{c^2}\partial^2 E/\partial t^2 + \mu_0 \partial^2 P/\partial t^2$$
$$P = \varepsilon_0\left(\chi^{(1)}E + \chi^{(3)}|E|^2 E + \chi^{(5)}|E|^4 E\right)$$

Combining these equations, yields

$$\nabla^2 E = \frac{1}{c^2}\partial^2 E/\partial t^2 + \mu_0\varepsilon_0 \partial^2\left(\chi^{(1)}E + \chi^{(3)}|E|^2 E + \chi^{(5)}|E|^4 E\right)/\partial t^2$$

$$\nabla^2 E = \frac{\left(1+\chi^{(1)} + \chi^{(3)}|E|^2 + \chi^{(5)}|E|^4\right)}{c^2}\partial^2 E/\partial t^2$$

$$\nabla^2 E - \frac{n^2}{c^2}\partial^2 E/\partial t^2 = 0$$

where we substituted n^2 for the susceptibility term. The term n, which is a function of the electric field intensity, should not be confused with the linear index of refraction, n_0, which is not a function of the field intensity. We assume a trial solution to this equation as a standard propagating harmonic wave in the z direction with a spatial envelope function.

$$E(x,y,z,t) = \frac{1}{2}\left(A(x,y,z)e^{j(\omega t - kz)} + A(x,y,z)^* e^{-j(\omega t - kz)}\right)$$

where

A is the spatial envelope of the wave
ω is the frequency
k is the spatial wave vector

Inserting this into the wave equation and assuming the z dependency of the envelope function is separable from the x and y dependencies yields

$$\nabla_{\perp}^{2} A - k^2 A - 2jk\,\partial A/\partial z + \frac{n^2\omega^2}{c^2} A = 0$$

$$\nabla_{\perp}^{2} A - 2jk\,\partial A/\partial z + \left(n^2 k_0^{\,2} - k^2\right) A = 0$$

$$\nabla_{\perp}^{2} A - 2jk\,\partial A/\partial z + \left(n^2 k_0^{\,2} - n_0^2 k_0^{\,2}\right) A = 0$$

$$\nabla_{\perp}^{2} A - 2jk\,\partial A/\partial z + \left(n^2 - n_0^2\right) k_0^{\,2} A = 0$$

We have dropped the second derivative of A with respect to z because this term is insignificant. The term $\nabla_{\perp}^{2}$ is the transverse Laplacian, or the Laplacian in the x and y coordinates only. As this equation is written there is no closed form solution for A. Additionally, the problem of solving for A becomes even more complicated if there is a variation in the index of refraction of the material across the wave, as in a waveguide structures. Using the beam propagation method, however, we can approximate the form of A at a small increment in the z direction beyond a known A. To see this, rewrite the equation using functional notation, isolate the envelope function and solve the derivative at a small distance Δz beyond a known envelope assuming the index terms are constant across the Δz interval.

$$2jk\,\partial A/\partial z = \nabla_\perp{}^2 A + \left(n^2 - n_0^2\right)k_0{}^2 A$$

$$\partial A/\partial z = \frac{1}{2jk}\left(\nabla_\perp{}^2 + \left(n^2 - n_0^2\right)k_0{}^2\right)A$$

$$\partial A/A = \frac{1}{2jk}\left(\nabla_\perp{}^2 + \left(n^2 - n_0^2\right)k_0{}^2\right)\partial z$$

$$\int_{A(z)}^{A(z+\Delta z)} \partial A/A = \int_z^{z+\Delta z} \frac{1}{2jk}\left(\nabla_\perp{}^2 + \left(n^2 - n_0^2\right)k_0{}^2\right)\partial z$$

$$\ln(A(z+\Delta z)) - \ln(A(z)) = \frac{1}{2jk}\left(\nabla_\perp{}^2 + \left(n^2 - n_0^2\right)k_0{}^2\right)(z+\Delta z - z)$$

$$\ln\left(A(z+\Delta z)/A(z)\right) = \frac{1}{2jk}\left(\nabla_\perp{}^2 + \left(n^2 - n_0^2\right)k_0{}^2\right)\Delta z$$

$$A(z+\Delta z) = e^{\frac{1}{2jk}\left(\nabla_\perp{}^2 + \left(n^2 - n_0^2\right)k_0{}^2\right)\Delta z} A(z)$$

$$A(z+\Delta z) = e^{\frac{1}{2jk}\left(\nabla_\perp{}^2 A(z) + \left(n^2 - n_0^2\right)k_0{}^2 A(z)\right)\Delta z} A(z)$$

This result shows that the known field and the material parameters can approximate the field envelope at a small incremental distance from a known point. Thus the envelope function can be determined by repeated application of the formula. The only remaining obstacle is the evaluation of the exponential term, particularly the transverse Laplacian. Although we might have a shot of evaluating the Laplacian for a real starting field, after a few increments, the complexity of the envelope function would overwhelm. An alternative is to specify the envelope at a known point along the axis of transmission with a sampling matrix giving the known field's amplitude and phase in the transverse plane. This also allows us to specify the index of refraction as a sampling matrix. Using this method, the complex envelope function is easily tracked through the real and imaginary amplitudes in each propagated sampling matrix. An additional benefit to using a sampling matrix is the

evaluation of the transverse Laplacian, which is the second partial derivative in rectangular coordinates. Using Fourier theory in one dimension

$$\nabla_{\perp}^{2} f(x) = {}^{\partial^2 f(x)}\!/_{\partial x^2} = \Im^{-1}\left\{k_x{}^2 \Im\{f(x)\}\right\}$$

where

$\Im$ is the Fourier transform operator
$\Im^{-1}$ is the inverse Fourier transform operator
k_x is the spatial frequency along the x direction

The Fourier transform can be evaluated using the discrete Fourier transform (DFT), usually implemented in most codes as the fast Fourier transform (FFT). The DFT is a summation approximation of the integral form of the transform

$$F(k_x) = \Im\{f(x)\} = \int_{-\infty}^{+\infty} f(x) e^{jk_x x} dx$$

$$F_s \approx \frac{1}{\sqrt{N}} \sum_{r=1}^{N} f_r e^{j2\pi(s-1)(r-1)/N}$$

$$k_{x_s} = \frac{2\pi(s-1)}{H}$$

where

$f(x)$ is a spatial function
$F(k_x)$ is the spatial frequency function of f(x)
k_x is the spatial frequency

f_r is the sampled spatial function of f(x)
F_s is the DFT spatial frequency function of f_r
N is the total number of points in the sample
H is the spatial extent of the sample
s is the sample point index in the Fourier plane
r is the sample point index in the real plane

An assumption in the discrete Fourier transform is that the input waveform repeats itself in space, with a period of the spatial extent of the sampling. Figure D.1 demonstrates this problem. Each line in the figure represents a BPM propagation step. Note that each step requires the execution of a DFT and an inverse DFT, both assuming that the function is periodic beyond the sampling extent. As portions of the wave approach the edge of the sampling space, through repeated application of the DFT, a matching wave approaches the opposite side of the sampling extent. Waveform components that travel across the boundary of the spatial extent of the sampling will reappear on the other side of the spatial sampling, which does not happen in the actual device, so we need to make sure it doesn't happen in the model.

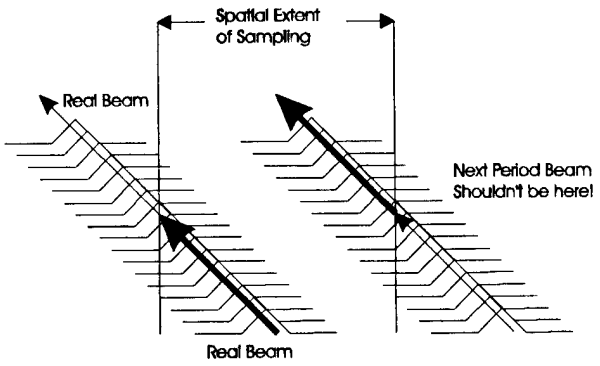

Figure D.1 Periodic Waveform Assumption of the Discrete Fourier Transform

To eliminate this, a windowing filter is used to attenuate signals approaching the sampling edges (note: there is no hard edge here, just the limits of the selected sampling region). This, however, must be done with care because the waveform must remain as accurate as possible in both spatial and frequency planes. An abrupt, severe, rectangular attenuation preserves the spatial characteristics across the wave, but acts like a mirror at the edges, reflecting the wave back into the sample space. Additionally, choosing an attenuator that is too sharp and narrow will cause a Gibbs Phenomenon, or ripples in the frequency domain, Figure D.2 (b). Choosing a smooth slowly varying window, such as a Hamming function, is desirable in the frequency plane, but will significantly distort the wave in the spatial domain, Figure D.2 (a).

Taken mathematically, the spatial filter is a multiplication of two functions in the spatial plane, filter t(x) and function f(x). Transforming to the spatial frequency plane, this becomes the convolution of the two separate transforms.

$$g(x) = t(x)f(x)$$
$$G(k_x) = T(k_x) * F(k_x)$$

Ideally, in the space domain, we would like a rectangle function, however, this results in a sinc function (which has ripples) in the frequency domain, giving rise to the Gibbs Phenomena. In the frequency domain, we would ideally like the filter transform, $T(k_x)$, to be a delta function, however, this would represent no filtering at all. One approximation for the delta function is a narrow Gaussian. This has been shown by Harvey (Am. Journal of Physics, Aug 1981) be the best at reduction of ripples, at the expense of smoothing any sharp profiles in the frequency domain. Unfortunately, a Gaussian function approximating a delta function in the frequency plane may not provide enough attenuation at the edges of the spatial sampling region. Combining these to functions results in a "best fit" solution. In the frequency domain, multiply these two functions together. If the widths are properly selected, most of the ripples in the frequency domain will be substantially reduced. The results in the spatial domain is the convolution of the two functions, or softening the edges of the rectangle function without creating any ripple in the spatial domain, Figure D.2 (c).

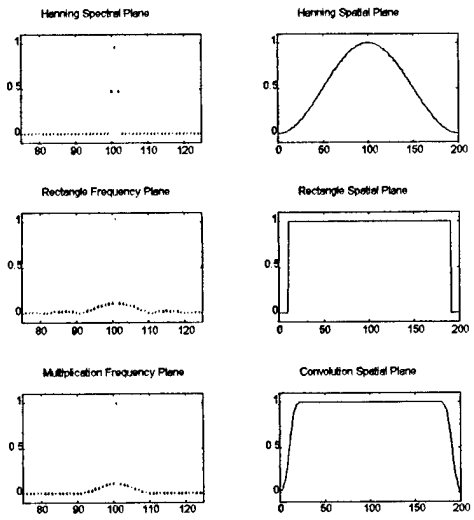

Figure D.2 Windowing Functions, Spatial and Frequency Plane Spectrums. (a) Hanning Filter, (b) Rectangle Filter, (c) Convolution Filter.

The distance between sampled points and the total size of the sampling space directly effects the accuracy of the BPM not only through the accuracy of the waveform itself, but also in the sampling of index waveguides. The Nyquist sampling theorem states that the largest frequency that can be sampled is ½ of the sampling rate. Spatial frequencies exceeding this will alias onto the existing frequency space causing distortion. Additionally, the resolution of the frequency space or the distance between discrete frequency points will be determined by the inverse of the size of the sampling space. Using these two criteria, we would like to sample as many points as possible! Opposing the desire to sample 1e6 points across a huge sample space, however, is the time a computer takes to calculate the DFT for the sample space multiplied by the number of steps taken for the propagating beam. Experience has shown that even 1000 point

samplings on a Pentium 90 processor using MATLAB, propagated over 1000 steps will take about 10 minutes to complete the calculation.

The size of Δz in the calculations also effects the accuracy and speed of the calculation because the method assumes that the index profile is constant over the distance Δz. VanRoey, ("Beam-propagation method: analysis and assessment," J. Opt. Soc. Am., July 1981), derives the following restrictions for the use of the BPM.

$$|\Delta n|_{\max} \sin^2(\alpha) << 1$$

$$p >> \frac{\lambda}{n_0}\sqrt{2}$$

$$p >> \frac{1}{n_0}\sqrt{2\pi\lambda|\Delta n|_{\max}\Delta z}$$

$$\Delta z\sqrt{\frac{2\pi}{p\lambda}\tan(\alpha)|\Delta n|_{\max}} << 1$$

$$\pi\frac{\tan(\alpha)}{p}\Delta z << 1$$

where

λ is the free space wavelength
α is the maximum angle corresponding to a significant part of the angular spectrum, usually the Numeric Aperture angle of the waveguide (N.A.=sin(α))
p is the highest spatial-frequency component of the refractive-index profile $\Delta n^2(x)$

VanRoey illustrated the effects of varying step size by propagating a 2.5 μm wide (1/e width) Gaussian beam (λ=1 μm) through 10 μm wide parabolic-index profile waveguide with a peak refractive-index variation of 1%. He then plotted the quadratic error of the

BPM propagated field compared to the closed form solution. The results are shown in Figure D.3.

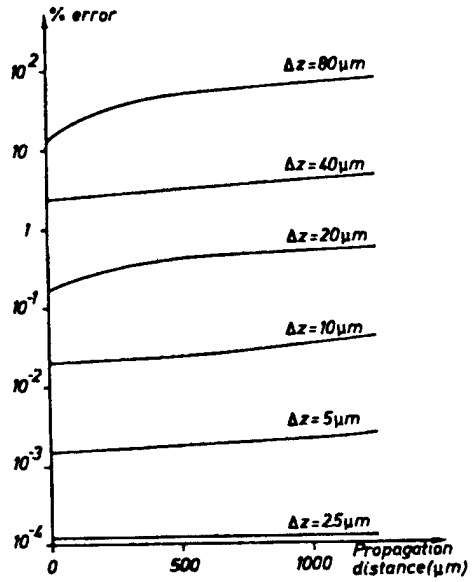

Figure D.3 Percent Error versus Propagation Distance for Varying Step Sizes (J. Opt Soc. Am./Vol. 71, No. 7/July 1981 pg. 806)

APPENDIX E: PROCESS FOLLOWER - SOLITON DEVICE

In this process, the thinning of the sample to 200 microns was done first. This allowed the high temperature Ni/Ge/Au ohmic contact to be applied and annealed without damaging the lower temperature Au/Zu/Au topside ohmic contact. Additionally, the SiN used to insulate the topside remains intact in tests up to 350°C, however it occasionally delaminates at 450°C, the processing temperature of Ni/Ge/Au contacts. Thus, the SiN is not exposed to the 420°C Ni/Ge/Au anneal temperature. The major disadvantage of this method is that the 200-micron sample is VERY fragile and must be handled with extreme care.

Thinning after the topside processing can be done, however, the silicon nitride should be checked carefully after the 420°C, 120 sec rapid thermal anneal.

Initial Cleave

1. Prior to cleaving, use a scribe to lightly mark the backside of the wafer where the sample will be cut from. After the cleave, the top and bottom of the sample will be indistinguishable without this mark.
2. Cleave a section of the wafer by making a 1-mm scribe mark at the edge of the wafer, turning the wafer over, and applying pressure to the backside of the wafer immediately above the scribe mark with a pointed object. The edge of the subsequent cleaved sample must be smooth along most of one side. This will be used to align the mask. The sample should be no smaller than 3/8" square - remember that the edges will not be used.

Thinning

3. Measure the starting thickness of your sample using a micrometer caliper ruler. G2-2329 is 625 microns thick. This indicates how much material needs to be removed.
4. Mount the sample onto a thin glass coverlet using low temperature, acetone soluble wax such as crystal bond.
5. Mount the sample/coverlet combination onto the top surface of a lapping chuck using crystal bond
6. Measure the chuck/sample/coverlet combination. Zero out a micrometer at this thickness. Use this zeroed micrometer as a guide to measure material removed.
7. Mount the lapping chuck into a lapping jig. If the jig has a thickness setting available, set this to remove the desired amount of material.
8. Mix a slurry of 2 tablespoons of 10 micron alumna lapping grit and water on the surface of a lapping plate. The slurry should be the consistency of mud. Spread the slurry into a 2" circle on the plate.
9. Place the lapping jig into the slurry. If using the lapping machine, set or a slow table and chuck rotation. About 1.5 on both dials.
10. If lapping by hand, use figure 8 motions, rotating the chuck by 120° every 100 strokes, to remove the desired amount of material.
11. Once the sample is thinned, clean with a toothbrush to remove any 10 micron grit.
12. Using a polishing pad, mix a slurry of 1 or 3 micron polishing grit with a mixture of 1 part Clorox bleach to 3 parts water. This is an aggressive chemical polish that will stain the back of the sample if not removed quickly after polishing.
13. Using the figure 8 motion, polish the sample until all scratches are removed from the surface. To clean the slurry, have the water running, and quickly move the sample from a polishing motion on the pad to the water. If the slurry does not come off immediately, a stain will result. If this happens, add a small amount of water (few drops) to the slurry, and polish again for 100 strokes. Move from a polishing motion to the water and quickly remove the slurry. A completed sample will not have any visible scratches and be mirror shinny. A mottled orange peal effect may be visible. This is not detrimental to the device and may be ignored.
14. Remove the lapping chuck from the lapping jig and place in a beaker of acetone. After several hours, the coverlet and sample will separate from the lapping chuck.
15. MOVE TO THE CLEANROOM FOR FURTHER PROCESSING. Set hot plates for 119°C and 200°C.
16. In the clean room, remove the sample from the acetone bath, and spray with a stream of acetone to remove any residual wax from the solution. Do not let the sample dry.
17. Place the sample into a clean beaker of acetone, and ultrasound the beaker for 5 minutes using the Cole-Parmer ultrasound in the class 10,000 area. DO NOT use the small Fisher ultrasound in the class 100 area. This ultrasound will break up thinned wafers; it'll break up un-thinned wafers too!
18. Spray with acetone for several seconds as you remove the sample from the acetone bath, then place the sample into another clean beaker filled with acetone. DO NOT allow sample to dry during the solvent cleaning process.
19. Boil this beaker of acetone at 119°C for 5 minutes.
20. Remove from acetone bath and spray with acetone for several seconds. Spray with methanol to remove the acetone for several seconds.

21. Place in a clean beaker fill with methanol. Boil sample in methanol at 119°C for 5 minutes.
22. Remove from methanol; do not allow sample to dry. Spray with methanol for several seconds as you remove the sample from the methanol bath, then spray with isopropyl alcohol (IPA) for several seconds to remove the methanol.
23. Boil sample in IPA at 200°C for 5 minutes.
24. Remove from IPA, do not allow sample to dry. Spray with IPA for several seconds as you remove the sample from the bath.
25. While still covered with IPA, place on a lint free rag and blow the IPA from the sample with nitrogen gun. Do not let the IPA evaporate without the nitrogen blow.

N-type Metallization

This step employs a pre-metal dip to remove any surface oxides built up upon the wafer during the thinning process. The sample should be loaded into the metallizer as soon as possible after the pre-metal dip.

Prep

Mix a pre-metal dip solution of 1 part buffered oxide etch to 50 parts 18 megohm deionized water from the class 10,000 area.

26. Use a drop of photoresist to attach the sample, backside up, to a glass slide.
27. Hot plate bake the sample at 119°C for 5 minutes to cure the resist.
28. Dip the sample into the pre-metal dip solution for 30 seconds.
29. DIW rinse for 2 minutes.
30. Blow dry thoroughly.
31. Blow dry some more.
32. Load into the metallizer and press 'cycle'.
33. Pump the metallizer to $1x10^{-6}$ torr and use standard posted techniques to deposit 50Å Ni/ 200Å Ge/ 2000Å Au.
34. Cool the metallizer 30 minutes prior to removing the sample.
35. Remove the sample, and soak in a beaker of acetone until the sample separates from the glass slide.
36. While spraying the sample with acetone, remove the sample from the soaking acetone, and place in a clean beaker of acetone. Boil sample in acetone at 119°C for 5 minutes.
37. Remove from acetone, do not allow sample to dry. Spray with acetone for several seconds as you remove the sample from the acetone bath, then spray with methanol to remove the acetone for several seconds. DO NOT allow sample to become dry during the solvent cleaning process.
38. Boil sample in methanol at 150°C for 5 minutes.
39. Remove from methanol, do not allow sample to dry. Spray with methanol for several seconds as you remove the sample from the methanol bath, then spray with isopropyl alcohol (IPA) for several seconds to remove the methanol.

40. Boil sample in IPA at 200°C for 5 minutes.
41. Remove from IPA, do not allow sample to dry. Spray with IPA for several seconds as you remove the sample from the bath.
42. While still covered with IPA, place on a lint free rag and blow the IPA from the sample with nitrogen gun. Do not let the IPA evaporate without the nitrogen blow.

N-contact Rapid Thermal Anneal

43. Place a clean GaAs mechanical wafer onto the silicon substrate of the Rapid Thermal Annealer (RTA). Place the sample, topside down, onto this mechanical substrate.
44. Close the RTA chamber and flow nitrogen gas at the maximum rate for 5 minutes.
45. Reduce gas flow to 3 sccm wait 1 minute for the chamber to stabilize.
46. RTA the sample at 420°C for 120 seconds.
47. Allow the RTA to cool to below 200°C before opening.

This completes backside processing

If you wish to process the front side first, start here.

Clean and Photoresist

Cleaning must immediately proceed photoresist, exposures, and develops. If you cannot do all three in a single day, consider waiting until you can.

Prep

Ensure exposure tool nitrogen tank in chase contains at least 750 lbs. of pressure and is on.

Ensure house nitrogen tank in chase is on.

Ensure house vacuum in chase is on.

Start with one hot plate at 119°C and the second at 200°C.

Turn on exposure tool gas, and start exposure tool lamps.

Set the exposure time of aligner to 1.6 seconds.

48. Boil sample in acetone at 119°C for 5 minutes.
49. Remove from acetone, do not allow sample to dry. Spray with acetone for several seconds as you remove the sample from the acetone bath, then spray with methanol to remove the acetone for several seconds. DO NOT allow sample to become dry during the solvent cleaning process.
50. Boil sample in methanol at 150°C for 5 minutes.
51. Remove from methanol, do not allow sample to dry. Spray with methanol for several seconds as you remove the sample from the methanol bath, then spray with isopropyl alcohol (IPA) for several seconds to remove the methanol.

52. Boil sample in IPA at 200°C for 5 minutes.
53. Remove from IPA, do not allow sample to dry. Spray with IPA for several seconds as you remove the sample from the bath.
54. While still covered with IPA, place on a lint free rag and blow the IPA from the sample with nitrogen gun. Do not let the IPA evaporate without the nitrogen blow.
55. Place on a clean glass microscope slide, and hot plate bake at 200°C for 5 minutes.
56. Remove from hot plate and allow sample to cool for 1 minute.
57. Center sample on spinner chuck, engage vacuum. Check vacuum hold.
58. Test spin sample to ensure acceleration, spin speed, and spin time. Sample should spin up to speed in 1 second, spin at 3000 rpm, and spin for 30 seconds.
59. With sample stopped, dispense enough 1400-17 photoresist to cover sample, typically 1 to 3 drops, but not bleed over edges. Immediately upon completing the dispense, start spinner.
60. Remove from spinner without disturbing top of resist. This can be tricky so be careful. If the resist is not completely covered and free from dust eddies and holes, briefly rinse sample with acetone and go to step 2.
61. Place sample face up on a clean microscope slide and hot plate bake for 5 minutes at 119°C.
62. Remove from hot plate and cool for 5 minutes.

Exposure

Prep

Ensure lamp control power supply has a number close to 274 watts on the display.

If the display says cold, wait until a number is display.

Turn the MJB-3 exposure tool on by pressing the power button

Set the MJB-3 to HP (High Precision) mode by pressing the HP/ST button until the HP side lights

Ensure the vacuum mask light is off

Clean the sample holder chuck with small amount of acetone on a wipe if necessary.

Mix a solution of 1 part 351 developer to 6 parts water. Typically 25ml / 150 ml.

Find the mask you will use and visually inspect to ensure mask is clean. If not, clean it.

63. With nitrogen gun, blow surface of exposure tool to remove dust. Do not attach mask yet.
64. If small amounts of photoresist are on the back of the sample, place sample upside down on the sample chuck of the exposure tool, and expose for 99 seconds. If large amounts of resist are on sample, remove with acetone being careful not to get acetone on the front of the sample. If this happens, however, rinse briefly with acetone and go to step 2.
65. This step is used to remove edge beading. Turn sample over and place a clean mechanical sample over the sample such that 1 mm of two edges are exposed. Expose for 60 seconds. Repeat procedure to exposure the two remaining edges.

66. Develop sample in developer for 60 seconds or until all back and edge photoresist is removed. Use caution not to disturb photoresist on the front of the sample.

67. Rinse in Deionized Tap Water (DIW) for 2 minutes. Thoroughly blow dry with nitrogen gun. A hot plate bake is not necessary at this point.

68. Attach mask to the mask chuck and press vacuum mask. This first exposure requires the bright field WAVEGUIDE quadrant of the mask. The dull chromium side of the mask must be facing away from the holder. Insert holder into the aligner and tighten thumbscrews.

69. Place sample face up on MJB-3 sample chuck. Sample must cover the flush open holes on the chuck. If not, place small squares of tape over open holes. Note that the large depressed hole on the left of the chuck must not be covered or blocked. This is the nitrogen hole for separation mode.

70. While watching sample from the side, or through the microscope, raise the sample to the mask. The sample should touch the mask when the substrate raiser lever is at the 90% position. If the sample doesn't contact at the 90% position, raise or lower the substrate chuck with the chuck dial gauge. Be careful; you can destroy samples and damage your mask if the chuck is set too high; start low to be safe.

    If the sample jumps to the mask, and cannot be put into separation, one or more of the holes in the substrate chuck are not covered properly. Lower chuck and check for good coverage.

    If the sample rotates in separation mode, the chuck is set just a bit too high and one corner is catching. Lower chuck.

    If in contact mode, Fresnel contact rings to not form, the chuck is too low. Raise chuck holder until rings form at the corners, but go away in separation mode.

71. Align sample cleaved edge to a straight edge on the mask.

72. Press the vacuum chamber button and ensure vacuum pressure drops to -0. 8 bar on the gauge. If not, ensure vacuum line to the UV exposure tower is off. Next check to ensure vacuum holes on the sample chuck are covered, and finally, check to ensure vacuum ring on the sample chuck is good and touches the mask around its entire circumference to the mask during contact.

73. If pressure drops to a good level, visually check the alignment once again. Note that vacuum chamber presses the sample closer to the mask, and sometimes moves the sample.

74. If alignment is ok, ensure exposure time is set for 1.6 seconds, and press the expose button.

75. Remove sample from exposure tool, and place in developer for 30 to 45 seconds. You can see the resist develop away. If watching the sample in the developer, hold sample in developer 10 seconds past the point where exposed photoresist appears to be removed.

76. Rinse in DIW for 2 minutes, then blow dry.

77. Examine with optical microscope with the green filter in place. If resist is not completely developed, develop again for 15-second increments followed by a 2 minutes DIW rinse and blow dry. Sometimes this can compensate for a bad exposure, however, be picky. If the exposure isn't perfect, rinse briefly with acetone and go back to step 2.

78. Place sample on a clean microscope slide and hot plate bake for 5 minutes at 119°C. This is critical to ensure the resist does not delaminate during subsequent processing.

Etch Waveguides

Note: The Silicon Nitride process immediately following the etch process requires a non-oxidized surface for good adhesion. As exposed GaAs and AlGaAs will oxide slowly at room temperature, you should be prepared to load the sample into the deposition chamber and pump the chamber to vacuum immediately following the etch process.

Prep

Mix a solution of 1:2:50 of H_3PO_4: H2O2: DIW, typically 5ml, 10ml, 250ml. For this, use the 18 Meg water from the Millipore system in the main cleanroom. Clean glassware thoroughly using 18 Meg DIW prior to mixing. Stir solution until viscosity turbulence is no longer visible. Solution must sit for at least 5 minutes prior to use.

The etch rate of this solution is approximately 1850Å/min at 23°C. Check temperature of solution. If not 23°C, adjust times accordingly. You can repeat etches to etch deeper, the reverse is not true. Err to the short side!

Ensure SiN Deposition chamber on the PlasmaTherm 790 at or below 50°C.

Set the PlasmaTherm controller to the right side deposition chamber.

Load the SIN100 process and prepare to run this process.

Set hotplates at 119°C and 200°C

79. Remove residual organic surface contamination by placing the sample into the left chamber of the PlasmaTherm 790 and executing the descum procedure. Run the procedure for 1 minute.
80. Remove sample from PlasmaTherm 790. Measure the resist thickness at several positions on the alpha step profilometer. Select positions that you can return to in subsequent measurements. Record resist thickness for later measurements. Center thickness for 1400-17 resist at 3000rpm spin speed should be 5000Å ± 500Å. Thickness will vary towards edges.
81. Prior to etch, stir etch solution to ensure viscosity turbulence is not visible. Immerse sample face up or sideways into acid etch solution for appropriate time. Never allow the face of the sample to reset against the walls or bottom of etch beaker. Assume 1850Å/min. Agitate gently each minute during etch.
82. Remove sample from etch solution and plunge into beaker of clean DIW. Rinse for 2 minutes in DIW, then blow dry.
83. Measure etch depth + resist thickness at the same positions you measured the initial resist thickness and subtract resist thickness to determine actual etch depth. Assume that the resist will swell slightly 200-500Å from pre-etch measurement. Calculate your etch rate. Use this rate for subsequent etches.
84. If the depth is short, go to step 35 using your calculated rate from step 37 to set the next time. If the depth is correct, remove resist with a short acetone, methanol, IPA rinse, and then blow dry. Measure and record final thickness.
85. Examine under a microscope. It is common for the etched area to look rough and nonuniform especially when viewed with a Newmarski-Differential Interference Contrast (DIC) system. The areas not etched should have sharp and straight edges and be smooth. Check the sharpness and continuity of the etch on the waveguides. Ensure separation between waveguide breaks. Rejection criteria at this point is up to the fabricator, however, this is still early enough in the process to restart without significant loss of time or resources.

Silicon Nitride Deposition

86. Boil sample in acetone at 119°C for 5 minutes.
87. Remove from acetone, do not allow sample to dry. Spray with acetone for several seconds as you remove the sample from the acetone bath, then spray with methanol to remove the acetone for several seconds. DO NOT allow sample to become dry during the solvent cleaning process.
88. Boil sample in methanol at 150°C for 5 minutes.
89. Remove from methanol, do not allow sample to dry. Spray with methanol for several seconds as you remove the sample from the methanol bath, then spray with isopropyl alcohol (IPA) to remove the methanol for several seconds.
90. Boil sample in IPA at 200°C for 5 minutes.
91. Remove from IPA, do not allow sample to dry. Spray with IPA for several seconds as you remove the sample from the bath.
92. While still covered with IPA, place on a lint free rag and blow the IPA from the sample with nitrogen gun. Do not let the IPA evaporate without the nitrogen blow.
93. Do not hot plate bake. This will cause oxides to form on the surface of the sample.
94. Immediately load into the right chamber of the PlasmaTherm 790. Close chamber and manually pump with turbopump.
95. When the chamber reaches $5x10^{-5}$ torr, manually flow 50sccm N_2 and 50 sccm He at a chamber pressure of 100 millitorr for 2 minutes. This is a flush step to help remove oxygen.
96. Stop manual mode and pump with the turbo pump until the chamber pressure reduces to $1x10^{-5}$ torr.
97. Set the standby temperature of the system to 250°C and wait until the platen temperature is within 5°C of 250°C.
98. Start the SIN100 process. Run this process to 6 minutes. This will deposit approximate 1000Å of silicon nitride.
99. When the process completes, set the system standby temperature to 50°C and allow the sample to cool under vacuum until the platen temperature is below 100°C. Note that the system temperature may be below 50° at the end of the SIN100 process.
100. Remove sample from PlasmaTherm 790 and reseal and turbopump system.
101. Examine sample under optical microscope. The SiN film should follow the contour of the substrate and should be smooth without any major holes or cracks. Small-discolored areas are typical and have not proven to be detrimental to the processing. If any delaminating occurs, the film is defective.
102. If the film needs to be removed, place the sample into the deposition chamber and run the etch program for 8 minutes. Note, this process will be updated with a new process to be used in the left etch chamber during the month of June. Removing the film will not damage the sample. Once the film is removed, go to step 40.

P type Metallization - Photoresist

Note: Following SiN deposition, sample should be very clean and does not require additional cleaning at this time. If just removed from the PlasmaTherm 790, photoresist can be immediately applied. If the sample is left out overnight, hot plate bake at 119°C for 5 minutes to drive out any water collected.

The photoresist used in this step acts as a photomask for both the opening of the silicon nitride and the deposition of the p-type contact. This type of dual use is termed a self-aligned process. Remember not to remove the photoresist after the silicon nitride is removed.

Prep

Hot plate at 119°C

Check availability of 1813 photoresist. If out, mix using 28 ml of 1827 resist with 10 ml type P thinner. Mix by rolling the bottle on the table and gently rotating end to end for 5 minutes. DO NOT SHAKE or ultrasound. Shaking will get bubbles into the resist; ultrasound will break up the long chain photoresist polymers.

Ensure spinner rotates at 4000 rpm.

103. Center sample on spinner chuck, engage vacuum. Check vacuum hold.

104. Test spin sample to ensure acceleration, spin speed, and spin time. Sample should spin up to speed in 1 second, spin at 4000 rpm, and spin for 30 seconds.

105. With sample stopped, dispense enough 1813 photoresist to cover sample, typically 1 to 3 drops, but not bleed over edges. Immediately upon completing the dispense, start spinner.

106. Remove from spinner without disturbing top of resist. This can be tricky so be careful. If the resist is not completely covered and free from dust eddies and holes, briefly rinse sample with acetone, and clean using the boiling solvent technique. Hot plate bake for 5 minutes at 119°C, allow to cool for 1 minute and go to step 57.

107. Place sample face up on a clean microscope slide and hot plate bake for 5 minutes at 119°C.

108. Remove from hot plate and cool for 5 minutes.

P-Type Metallization - Exposure

Prep

Ensure lamp control power supply has a number close to 274 watts on the display.

If the display says cold, wait until a number is display.

Turn the MJB-3 exposure tool on by pressing the power button

Set the MJB-3 to HP (High Precision) mode by pressing the HP/ST button until the HP side lights

Ensure the vacuum mask light is off

Clean the sample holder chuck with small amount of acetone on a wipe if necessary.

Mix a solution of 1 part 351 developer to 6 parts water. Typically 25ml / 150 ml.

Find the mask you will use and visually inspect to ensure mask is clean. If not, clean it.

109. With nitrogen gun, blow surface of exposure tool to remove dust. Do not attach mask yet.

110. If small amounts of photoresist are on the back of the sample, place sample upside down on the sample chuck of the exposure tool, and expose for 99 seconds. If large amounts of resist are on

sample, remove with acetone being careful not to get acetone on the front of the sample. If this happens, however, rinse briefly with acetone and go to step 2.

111. This step is used to remove edge beading. Turn sample over and place a clean mechanical sample over the sample such that 1 mm of two edges is exposed. Expose for 60 seconds. Repeat procedure to exposure the two remaining edges.

112. Develop sample in developer for 60 seconds or until all back and edge photoresist is removed. Use caution not to disturb photoresist on the front of the sample.

113. Rinse in Deionized Tap Water (DIW) for 2 minutes. Thoroughly blow-dry with nitrogen gun. A hot plate bake is not necessary at this point.

114. Attach mask to the mask chuck and press vacuum mask. This first exposure requires the dark field WAVEGUIDE quadrant of the mask. The dull chromium side of the mask must be facing away from the holder. Insert holder into the aligner and tighten thumbscrews.

115. Place sample face up on MJB-3 sample chuck. Sample must cover the flush open holes on the chuck. If not, place small squares of tape over open holes. Note that the large depressed hole on the left of the chuck must not be covered or blocked. This is the nitrogen hole for separation mode.

116. While watching sample from the side, or through the microscope, raise the sample to the mask. The sample should touch the mask when the substrate raiser lever is at the 90% position. If the sample doesn't contact at the 90% position, raise or lower the substrate chuck with the chuck dial gauge. Be careful; you can destroy samples and damage your mask if the chuck is set too high; start low to be safe.

If the sample jumps to the mask, and cannot be put into separation, one or more of the holes in the substrate chuck are not covered properly. Lower chuck and check for good coverage.

If the sample rotates in separation mode, the chuck is set just a bit too high and one corner is catching. Lower chuck.

If in contact mode, Fresnel contact rings to not form, the chuck is too low. Raise chuck holder until rings form at the corners, but go away in separation mode.

117. Align sample cleaved edge to a straight edge on the mask.

118. Press the vacuum chamber button and ensure vacuum pressure drops to -0. 8 bar on the gauge. If not, ensure vacuum line to the UV exposure tower is off. Next check to ensure vacuum holes on the sample chuck are covered, and finally, check to ensure vacuum ring on the sample chuck is good and touches the mask around its entire circumference to the mask during contact.

119. If pressure drops to a good level, visually check the alignment once again. Note that vacuum chamber presses the sample closer to the mask, and sometimes moves the sample.

120. If alignment is ok, ensure exposure time is set for 5.0 seconds, and press the expose button.

121. Remove sample from exposure tool, and place in developer for 30 to 45 seconds. You can see the resist develop away. If watching the sample in the developer, hold sample in developer 10 seconds past the point where exposed photoresist appears to be removed.

122. Rinse in DIW for 2 minutes, then blow dry.

123. Examine with optical microscope with the green filter in place. If resist is not completely developed, develop again for 15-second increments followed by a 2 minutes DIW rinse and blow dry. Sometimes this can compensate for a bad exposure, however, be picky. If the exposure isn't perfect, briefly rinse

sample with acetone, and clean using the boiling solvent technique. Hot plate bake for 5 minutes at 119°C, allow to cool for 1 minute and go to step 57.

124. Place sample on a clean microscope slide and hot plate bake for 5 minutes at 119°C. This is critical to ensure the resist does not delaminate during subsequent processing.

P-Type Metallization – Nitride Etch

Prep

Ensure the temperature of the PlasmaTherm 790 is 50°C or lower

Load process etch and prepare to run the process

125. Place sample into the right chamber of the PlasmaTherm 790. The temperature of the platen must be lower than 100°C. Calibration runs of this process were done at 50°C.

126. Run the process etch for 3 minutes to etch through and slightly undercut 2000Å of SiN.

127. Do not remove the photoresist for the subsequent metallization.

128. Examine the sample using an optical microscope following this step. The tops of the waveguides must be free from nitride. Remaining nitride looks like a smudge the follows the edges of the openings. If required, set the sample for a 1 minutes nitride etch using the etch process.

P-Type Metallization – Metallization

The pre-metal dip is used to remove any oxides formed on the substrate surface formed during the nitride etch or by general oxidation over time. The dip will slowly etch the SiN, thus a thorough DIW rinse is critical to ensure the SiN remains intact.

Samples should be loaded into the metallizer as soon as possible following the pre-metal dip.

Prep

Mix a pre-metal dip solution consisting of 1 part buffered oxide etch and 50 parts 18 Meg DIW

Load Au and Zn into the boat roundtable at the base of the metallizer enclosure.

Mark where the metals are on the rotation wheel outside the enclosure.

129. Dip the sample into the pre-metal dip for 15 seconds.

130. Flush with tap DIW for 2 minutes.

131. Thoroughly blow dry with nitrogen

132. Blow dry with nitrogen some more. Do not hot plate bake.

133. Immediately load the sample into the metallizer and press "Cycle" on the control console.

134. Pump system to $1x10^{-6}$ torr and use standard posted procedures to deposit 50Å of Au, 200Å of Zn, and 2000Å of Au.

135. Cool the chamber for 30 minutes after metallization, then remove sample.

136. Place sample into beaker of acetone for 10 minutes. Agitate with a stream of acetone to remove metal from substrate. Do not let acetone dry on substrate, this is DESTROY you sample, guaranteed.

137. Remove sample from acetone while spraying the sample with acetone. Place into a clean beaker of acetone and boil for 5 minutes at 119°C.

138. Remove from acetone, do not allow sample to dry. Spray with acetone for several seconds as you remove the sample from the acetone bath, then spray with methanol to remove the acetone for several seconds. DO NOT allow sample to become dry during the solvent cleaning process.

139. Boil sample in methanol at 119°C for 5 minutes.

140. Remove from methanol, do not allow sample to dry. Spray with methanol for several seconds as you remove the sample from the methanol bath, then spray with isopropyl alcohol (IPA) to remove the methanol for several seconds.

141. Boil sample in IPA at 119°C for 5 minutes.

142. Remove from IPA, do not allow sample to dry. Spray with IPA for several seconds as you remove the sample from the bath.

143. While still covered with IPA, place on a lint free rag and blow the IPA from the sample with nitrogen gun. Do not let the IPA evaporate without the nitrogen blow.

144. Examine sample using an optical microscope. Ensure metal is removed from unwanted areas. If unwanted metal remains, place the sample into acetone ultrasound for 5 minutes in the Cole-Parmer ultrasound in the class 10,000 hood. DO NOT USE the small Fisher ultrasound. These will breakup your sample, and delaminate the metal. Go to step 91 following the ultrasound.

P-type Contact – Anneal

Note: If you elect to process the top side first, omit this step.

Prep

Hot plates at 119°C and 200°C

145. Place the sample on a clean glass microscope slide hot plate bake to 119°C for at least 1 minute.

146. Move the slide and sample to a 200°C hot plate and set the hot plate for 350°C. The plate will ramp to 350°C within 20 minutes. Hold at this temperature for 20 minutes, and set the hot plate for 100°C. The plate will cool to 100°C within 20 minutes.

147. Remove the sample and cool for 1 minute.

Pad Metal – Photoresist

Prep

Hot plate at 119°C

Check availability of 1813 photoresist. If out, mix using 28 ml of 1827 resist with 10 ml type P thinner. Mix by rolling the bottle on the table and gently rotating end to end for 5 minutes. DO NOT

SHAKE or ultrasound. Shaking will get bubbles into the resist; ultrasound will break up the long chain photoresist polymers.

Ensure spinner rotates at 4000 rpm.

148. Place sample on a clean glass microscope slide, and hot plate bake at 119°C for 5 minutes.

149. Remove from hot plate and allow sample to cool for 1 minute.

150. Center sample on spinner chuck, engage vacuum. Check vacuum hold.

151. Test spin sample to ensure acceleration, spin speed, and spin time. Sample should spin up to speed in 1 second, spin at 4000 rpm, and spin for 30 seconds.

152. With sample stopped, dispense enough 1813 photoresist to cover sample, typically 1 to 3 drops, but not bleed over edges. Immediately upon completing the dispense, start spinner.

153. Remove from spinner without disturbing top of resist. This can be tricky so be careful. If the resist is not completely covered and free from dust eddies and holes, briefly rinse sample with acetone and go to step 2.

154. Place sample face up on a clean microscope slide and hot plate bake for 5 minutes at 119°C.

155. Remove from hot plate and cool for 5 minutes.

Pad Metal - Exposure

Prep

Ensure lamp control power supply has a number close to 274 watts on the display.

If the display says cold, wait until a number is display.

Turn the MJB-3 exposure tool on by pressing the power button

Set the MJB-3 to HP (High Precision) mode by pressing the HP/ST button until the HP side lights

Ensure the vacuum mask light is off

Clean the sample holder chuck with small amount of acetone on a wipe if necessary.

Mix a solution of 1 part 351 developer to 6 parts water. Typically 25ml / 150 ml.

Find the mask you will use and visually inspect to ensure mask is clean. If not, clean it.

156. With nitrogen gun, blow surface of exposure tool to remove dust. Do not attach mask yet.

157. If small amounts of photoresist are on the back of the sample, place sample upside down on the sample chuck of the exposure tool, and expose for 99 seconds. If large amounts of resist are on sample, remove with acetone being careful not to get acetone on the front of the sample. If this happens, however, rinse briefly with acetone and go to step 2.

158. This step is used to remove edge beading. Turn sample over and place a clean mechanical sample over the sample such that 1 mm of two edges are exposed. Expose for 60 seconds. Repeat procedure to exposure the two remaining edges.

159. Develop sample in developer for 60 seconds or until all back and edge photoresist is removed. Use caution not to disturb photoresist on the front of the sample.

160. Rinse in Deionized Tap Water (DIW) for 2 minutes. Thoroughly blow dry with nitrogen gun. A hot plate bake is not necessary at this point.

161. Attach mask to the mask chuck and press vacuum mask. This first exposure requires the dark field PAD quadrant of the mask. The dull chromium side of the mask must be facing away from the holder. Insert holder into the aligner and tighten thumbscrews.

162. Place sample face up on MJB-3 sample chuck. Sample must cover the flush open holes on the chuck. If not, place small squares of tape over open holes. Note that the large depressed hole on the left of the chuck must not be covered or blocked. This is the nitrogen hole for separation mode.

163. While watching sample from the side, or through the microscope, raise the sample to the mask. The sample should touch the mask when the substrate raiser lever is at the 90% position. If the sample doesn't contact at the 90% position, raise or lower the substrate chuck with the chuck dial gauge. Be careful; you can destroy samples and damage your mask if the chuck is set too high; start low to be safe.

    If the sample jumps to the mask, and cannot be put into separation, one or more of the holes in the substrate chuck are not covered properly. Lower chuck and check for good coverage.

    If the sample rotates in separation mode, the chuck is set just a bit too high and one corner is catching. Lower chuck.

    If in contact mode, Fresnel contact rings to not form, the chuck is too low. Raise chuck holder until rings form at the corners, but go away in separation mode.

164. Align sample cleaved edge to a straight edge on the mask.

165. Press the vacuum chamber button and ensure vacuum pressure drops to -0. 8 bar on the gauge. If not, ensure vacuum line to the UV exposure tower is off. Next check to ensure vacuum holes on the sample chuck are covered, and finally, check to ensure vacuum ring on the sample chuck is good and touches the mask around its entire circumference to the mask during contact.

166. If pressure drops to a good level, visually check the alignment once again. Note that vacuum chamber presses the sample closer to the mask, and sometimes moves the sample.

167. If alignment is ok, ensure exposure time is set for 5.0 seconds, and press the expose button.

168. Remove sample from exposure tool, and place in developer for 30 to 45 seconds. You can see the resist develop away. If watching the sample in the developer, hold sample in developer 10 seconds past the point where exposed photoresist appears to be removed.

169. Rinse in DIW for 2 minutes, then blow dry.

170. Examine with optical microscope with the green filter in place. If resist is not completely developed, develop again for 15-second increments followed by a 2 minutes DIW rinse and blow dry. Sometimes this can compensate for a bad exposure, however, be picky. If the exposure isn't perfect, rinse briefly with acetone and go back to step 2.

171. Place sample on a clean microscope slide and hot plate bake for 5 minutes at 119°C. This is critical to ensure the resist does not delaminate during subsequent processing.

Pad Metal – Metallization

The pre-metal dip is not used in this step. All sections of the semiconductor should be covered with either nitride or metal at this point.

Prep

Load Ti and Au into the boat roundtable at the base of the metallizer enclosure.

Mark where the metals are on the rotation wheel outside the enclosure.

172. Place the sample into the left chamber of the PlasmaTherm 790 and run process DESCUM for 1 minute.

173. Remove the sample from the PlasmaTherm, load the sample into the metallizer, and press "Cycle" on the control console.

174. Pump system to $1x10^{-6}$ torr and use standard posted procedures to deposit 100Å of Ti, and 3000Å of Au. This metal combination adheres well to almost any material. Note that Ti reacts with the tungsten boats, thus only 3 to 4 Ti runs can be made with a single boat.

175. Cool the chamber for 30 minutes after metallization, then remove sample.

176. Place sample into beaker of acetone for 10 minutes. Agitate with a stream of acetone to remove metal from substrate. Do not let acetone dry on substrate, this is DESTROY you sample, guaranteed.

177. Remove sample from acetone bath while spraying the sample with acetone. Place into a clean beaker of acetone and boil for 5 minutes at 119°C.

178. Remove from acetone, do not allow sample to dry. Spray with acetone for several seconds as you remove the sample from the acetone bath, then spray with methanol to remove the acetone for several seconds. DO NOT allow sample to become dry during the solvent cleaning process.

179. Boil sample in methanol at 119°C for 5 minutes.

180. Remove from methanol, do not allow sample to dry. Spray with methanol for several seconds as you remove the sample from the methanol bath, then spray with isopropyl alcohol (IPA) to remove the methanol for several seconds.

181. Boil sample in IPA at 119°C for 5 minutes.

182. Remove from IPA, do not allow sample to dry. Spray with IPA for several seconds as you remove the sample from the bath.

183. While still covered with IPA, place on a lint free rag and blow the IPA from the sample with nitrogen gun. Do not let the IPA evaporate without the nitrogen blow.

184. Examine sample using an optical microscope. Ensure metal is removed from unwanted areas. If unwanted metal remains, place the sample into acetone ultrasound for 5 minutes in the Cole-Parmer ultrasound in the class 10,000 hood. DO NOT USE the small Fisher ultrasound. These will breakup your sample, and delaminate the metal. Go to step 127 following the ultrasound.

This completes topside processing. The sample is ready for cleaving and mounting.

Bibliography

[1] T. Maimann, "Stimulated Optical Radiation in Ruby," Nature 187 p 493, 1960.

[2] A.C.S. van Heel, Nature 173, 39 (1954)

[3] N.S. Kapany, J. Opt Soc. Am. 49, 779 (1959).

[4] P.A. Franken, A.E. Hill, C.W. Peters, W. Weinreich, "Generation of Optical Harmonics," Phys Rev. Lett. Vol. 7(4) page 118 , 15 Aug 1961.

[5] M. Bass, P. Franken, J. Ward, G. Weinreich, "Optical Rectification," Phys. Rev. Lett., 9 (11), page 446, 1 Dec 1962.

[6] M. Bass, P. Franken, A. Hill, C. Peters, G. Weinreich, "Optical Mixing," Phys. Rev. Lett., 8 (1), page 18, 1 Jan 1962.

[7] R. Kingston, "Parametric Amplification and Oscillation at Optical Frequencies," Proceedings of the IRE Vol 50(4), page 472, April 1962.

[8] G. Eckhardt, R. Hellwarth, F. McClung, S. Schwarz, D. Weiner, "Stimulated Raman Scattering from Organic Liquids," Phys Rev. Lett., Vol 9(11), page 455, 1 Dec 1962.

[9] P. Maker, R. Terhune, C. Savage, "Intensity-Dependent Changes in the Refractive Index of Liquids," Phys. Rev. Lett., Vol 12(18) page 507, 4 May 1964.

[10] R.G. Hunsperger, *Integrated Optics: Theory and Technology*, Springer-Verlag, Berlin, GE,1985.

[11] P.T. Ho, L. Glasser, E.P. Ippen, H.A. Haus, "Pciosecond Pulse Generation with a cw GaAlAs Laser Diode," Appl. Phys. Lett., vol 33, page 241, 1978

[12] H. Ito, H. Yokoyama, S. Murata, H. Inaba, "Picosecond Optical Pulse Generation for an R.F. Modulation AlGaAs Double Heterostructure Diode Laser," Electron. Lett. ,Vol. 15, page 738, 1979.

[13] Y. Silberberg, P. Smith D. Eilenberger, D. Miller, A. Gossard, W. Wiegmann, "Passive Modelocking of a Semiconductor Diode Laser," Opt. Lett., Vol. 9, page 507, 1984.

[14] P.-T. Ho, "Coherent pulse generation with a GaAlAs laser by Active Modelocking," Electron. Lett., Vol 15, page 526, 1979.

[15] P. Morton, J. Bowers, L. Koszi, M. Soler, J. Lopata, and D. Wilt, "Monolithic Hybrid Modelocked 1.3 μm Semiconductor Lasers," Appl. Phys. Lett., Vol. 56, page 111 1990.

[16] P. Delfyett, L. Florez, N. Stoffel, T. Gmitter, N. Andreadakis, Y. Silberberg, J. Heritage, G. Alphonse, "High-Power Ultrafast Laser Diodes," IEEE J. Quant. Electron., Vol 28 (10), page 2203, Oct 1992.

[17] F.P. Kapron, D.B. Keck, R.D. Maurer, Appl Phys. Lett., 17 page 423, (1970).

[18] T. Miya, Y. Terunuma, T. Hosaka, T. Miyashita, Electron. Lett.. 15, page 106 (1979).

[19] R Stolen, E. Ippen, "Stimulated Brillouin Scattering in Optical Fibers," Appl. Phys. Lett., Vol 21(11), page 539 1 Dec 1972.

[20] R. Stolen, A. Ashkin, Appl. Phys. Lett. Vol 2, page 294 (1973).

[21] R. Stolen, "Phase-Matched-Stimulated Four-Photon Mixing in Silica-Fiber Waveguides," IEEE J. Quant Elec., Vol. QE-11(3), page 100, March 1975.

[22] L. Mollenauer, R. Stolen, "Experimental Observation of Picosecond Pulse Narrowing and Solitons in Optical Fibers," Phys. Rev. Lett., Vol 45(13), page 1095, 29 Sep 1980.

[23] G. Agrawal, *Nonlinear Fiber Optics*, Academic Press, New York, New York, (1995).

[24] R. Fork, C. Brito Cruz, P. Becker, C. Shank, Opt. Lett. Vol 12, page 483 (1987).

[25] S. Yamazaki, M. Shikada, "POF for High-Speed PC and Home Networks," OSA Annual Meeting ILS-XIII, ThM2, Long Beach, CA, 12 Oct 1997.

[26] C. Pollock, *Fundamentals of Optoelectronics*, Irwin, Chicago, IL, page 6, 1995.

[27] T. Ono, "Characteristics of Optical Duobinary Signals in Terabit/s Optical Transmission Systems," OSA Annual Meeting ILS-XIII, ThT3, Long Beach, CA, 12 Oct 1997.

[28] B. Mathason, P. Delfyett, "All-optical Clock Recovery Using Injection Mode-Locked Laser Diodes," Proc. SPIE v 3075, page 52 1997.

[29] H. Shi, P. Delfyett, "20 x 5Gbit/s Optical WDM Transmitter Using a Single-Stripe Multi-Wavelength Modelocked Semiconductor Laser," Electron. Lett., tbd 1998.

[30] J. Sokoloff, P. Prucnal, I. Glesk, M. Kane, "A Terahertz Optical Asymmetric Demultiplexer (TOAD)," IEEE Photonics Tech. Lett., Vol 5(7), July 1993.

[31] M. Eiselt, "Optical Loop Mirror with Semiconductor Laser Amplifier," Electron. Lett., Vol. 28, page 1505, 1992.

[32] M. Islam, E. Sunderman, R. Stolen, W. Pleibel, J. Simpson, "Soliton Switching a Fiber Nonlinear Mirror," Opt. Lett., Vol. 15, page 811, 1989.

[33] P LiKamWa, A. Kan'an, "Ultrafast All-Optical Switching in Multiple-Quantum-Well Y-Junction Waveguides at the Band Gap Resonance," IEEE J. Quant. Elect., Vol 2(3), Sept 1996.

[34] G. I. Stegeman, E. Wright, "All-Optical Waveguide Switching," Optical and Quant. Electronics, Vol 22 page 95, 1990.

[35] G. I. Stegeman, "Material Requirements for Nonlinear Third Order Phenomena in Waveguides," *Nonlinear Optics: Fundamentals, Materials and Devices,* S. Miyata, Ed, Elsevier Science Publishers, B.V., page 337, 1992.

[36] S. Singh, *Handbook of Lasers*, Chemical Rubber Company, Cleveland, OH, 1971.

[37] B. Lawrence, W. Torruellas, G. I. Stegeman, "Stable Self-Trapping and Ring Formation in Polydiacetylene Para-Toluene Sulfonate," Optics Lett., Vol 20 (24) page 2481, 15 Dec 1997.

[38] M. Jager, G.I. Stegeman, "Comparison of Quasi-Phase-Matching Geometries for Second-harmonic Generation in Poled Polymer Channel Waveguides at 1.5 μm," Appl. Phys. Lett., Vol 68(9), page 1183, 26 Feb 1996.

[39] M. Sundheimer, Ch. Bosshard, E. VanStryland, G.I. Stegeman, "Large nonlinear Phase Modulation in Quasi-Phase Matched KTP Waveguides as a Result of Cascaded Second-Order Processes," Optics Lett., Vol 18 (17), page 1397, 1 Sep 1993.

[40] R Schiek, Y. Baek, G.I. Stegeman, "One-dimensional Spatial Solitary Waves Due to Cascaded Second-Order Nonlinearities in Planar Waveguides," Phys. Rev E, Vol 53(1), page 1138, Jan 1996.

[41] R. Fuerst, B. Lawrence, W. Torreullas, G.I. Stegeman, "Beam reshaping by use of Spatial Solitons in the Quadratic Nonlinear Medium KTP," Optics Lett., Vol 22 (1), 1 Jan 1997.

[42] M. Ohkawa, R. Fuerst, G.I. Stegeman, "Characteristics of Second Harmonic Generation with Quadratic Soliton Generation Versus Conventional Methods," J. Opt. Society B, tbd.

[43] B.S. Wherrett and H.A. Higgins, "Theory of Nonlinear Refraction Near the Band Edge of a Semiconductor," Proc. R. Soc. Lond. A, Vol 379, page 67, 1982.

[44] M.J. Adams, D.A.O. Davies, M.C. Tatham, M.A. Fisher, "Nonlinearities in Semiconductor Laser Amplifiers," Optical and Quantum Electronics, Vol. 27, pg. 9, 1995.

[45] D. Miller, D. Chemla, D Eilenberger, P Smith, "Degenerate Four-Wave Mixing in Room-Temperature GaAs/GaAlAs Multiple Quantum Well Structures," Appl. Phys. Lett., Vol 42(11), page 925, 1 June 1983.

[46] J. Aitchison, D. Hutchings, J. Kang, G.I. Stegeman, A. Villeneuve, "The Nonlinear Optical Properties of AlGaAs at the Half Band Gap," IEEE J. Quantum Electronics, Vol 33(3), March 1997.

[47] J. Kang, *Spatial Solitons in AlGaAs Waveguides*, University of Central Florida, Orlando FL, 1996.

[48] C.T. Hultgren, D.J. Dougherty, E.P. Ippen, "Above- and Below-Band Femtosecond Nonlinearities in Active AlGaAs Waveguides," Applied Physics Letters, vol. 61, no. 23, 7 Dec 1992, pg. 2767.

[49] M.H. LaGasse, K.K. Anderson, C.A. Wang, H.A. Haus, and J.G. Fujimoto, Appl. Phys. Lett. 56, page 1834, 1990.

[50] Hultgren, C.T., Ippen, E.P., "Ultrafast Refractive Index Dynamics in AlGaAs Diode Laser Amplifiers," Appl. Phys. Lett. 59 (6), pg. 635, 5 Aug 1991.

[51] J. Zhou, N. Park, J. Dawson, K. Vahala, "Highly nondegenerate four-wave mixing and gain nonlinearity in a strained multiple-quantum-well optical amplifier," Appl. Phys. Lett. 62 (19), 10 May 1993.

[52] K. Kikuchi, M. Kakui, C.E. Zah, T.P. Lee, IEEE J. Quantum Electron. QE-28, 151 (1992).

[53] K Hall, G. Lenz, E. Ippen, U. Koren, G. Raybon, "Carrier Heating and Spectral Hole Burning in Strained-Layer Quantum-Well Laser Amplifiers at 1.5 μm," Appl. Phys. Lett. Vol 61 (21) page 2512, 23 Nov 1992.

[54] T.S. Moss, "Theory of Intensity Dependence of Refractive Index," Phys. Status Solidi B, vol. 101, page 555, 1980.

[55] D. Miller, C. Seaton, M Prise, S. Smith, Phys. Rev. Lett., Vol 47, page 197, 1981.

[56] P. Bhattacharya, *Semiconductor Optoelectronic Devices*, Prentice Hall, Englewood Cliffs, New Jersey, 1994.

[57] W. Spitzer and H. Fan, Phys Rev. Vol 106, page 883 (1957).

[58] J. Pankove, "Properties of Heavily Doped Germanium," Progress in Semiconducotrs, ed. A.F. Gibson, Heywood Press, Vol 9 page 67, 1965.

[59] J. Verdeyen, *Laser Electronics*, Prentice-Hall, Englewood Cliffs, New Jersey, 1989.

[60] J. Kang, *Spatial Solitons in AlGaAs Waveguides*, University of Central Florida, Orlando FL, 1996.

[61] M. Canva, R. Ruerst, S. Baboiu, G.I.Stegeman, "Quadratic Spatial Soliton Generation by Seeded Downconversion of a Strong Harmonic Pump Beam," Optics Lett., Vol 22(22) 15 Nov 1997.

[62] G. Khitrova, H. Gibbs, Y. Kawamura, H. Iwamura, and T. Ikegami, "Spatial Solitons in a Self-Focusing Semiconductor Gain Medium," Phys. Rev. Lett., Vol 70(7), page 920, 15 Feb 1993.

[63] B. Lawrence, Third Order Optical Nonlinearities and Spatial Solitary Waves in Polydiacetylene Toluene Sulfonate, University of Central Florida, Orlando, FL, 1997.

[64] J. Kang, C.H. Hamilton, J.S. Aitchison, G.I. Stegeman, "Spatial Soliton Robustness Against Spatially Anisotropic Phase Perturbations," Appl. Phys. Lett. Vol 70(11), page 1363, 17 March 1997.

[65] Pliska, Thomas, Etch Rate Data – PlasmaTherm 790 Anisotropic Etch of PMMA, 1 May 1998

[66] PlasmaTherm Corporation, "Plasma Enhanced Silicon Nitride Deposition," Technical Application Notes, 24 Sep 1992.

[67] C. Kutsche, *Photo of cleaved GaAs laser waveguide ridge*, Electronic Devices Directorate, Wright Laboratories, WPAFB, OH 45433. May 1994.

[68] PlasmaTherm Corporation, "Silicon Nitride Film Stress Control via Carrier Gas Composition," Technical Application Notes, 24 Sep 1992.

[69] T.S. Moss, "Absorption edge of GaAs at Room Temperature," J. Appl. Phys. 32, 2136, 1961

[70] H.H. Berger, "Models for contacts to planar devices," Solid State Electron. 15:145-158 (1972)

[71] H. Murrmann, D. Widmann, "Current crowding on metal contacts to planar devices," IEEE Trans. Electron Dev., ED-16(12): 1022-1024 (1969).

[72] G.K. Reeves, H.B. Harrison, "Obtaining the specific contact resistance from transmission line model measurements," IEEE Electron Dev. Lett., EDL-3(5), p 111-113 (1982)

[73] D.K. Ferry, *Gallium Arsenide Technology (II)*, Howard W. Sams & Company, Carmel, IN., p 393-399, (1990)

[74] G. Khitrova, H.M. Gibbs, Y. Kawamura, H. Iwamura, T. Ikegami, "Spatial Solitons in a Self-Focusing Semiconductor Gain Medium," Phys. Rev Lett. Vol (70) No 7, pg 920, 15 Feb 1993.

[75] A. Yariv and P. Yeh, *Optical Waves in Crystals*, New York: New York: John Wiley & Sons, 230 (1984).

[76] E. Hecht, *Optics*, Reading, MA, Addison-Wesley Publishing Co, 164 (1987)